# Assessment of nasal airflow simulations

On the accuracy and usage of CFD simulations for healthy and NAO patients

Fulin Yang

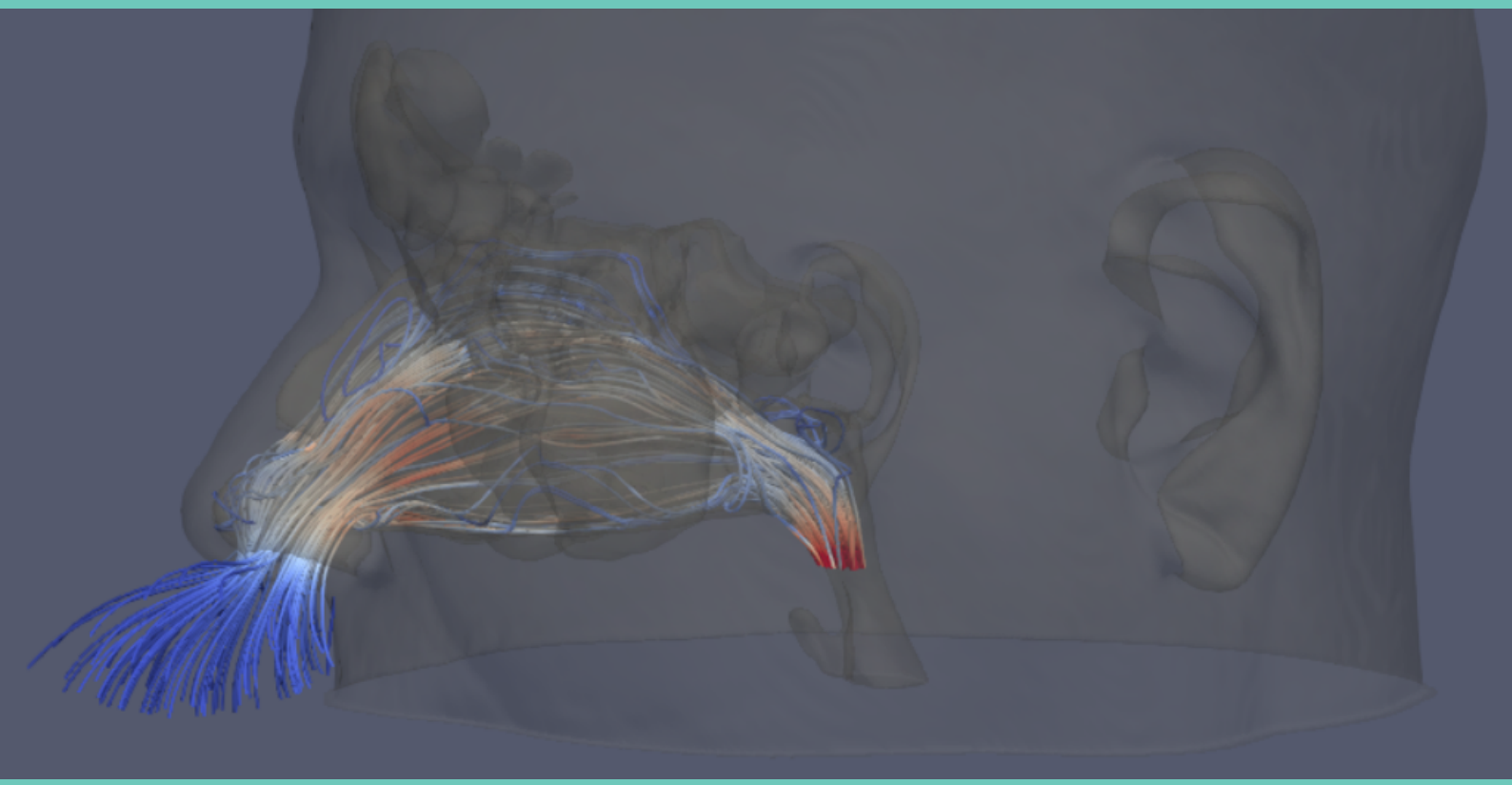

TU Delft

# Assessment of nasal airflow simulations

## On the accuracy and usage of CFD simulations for healthy and NAO patients

by

Fulin Yang

to obtain the degree of Master of Science
at the Delft University of Technology,
to be defended publicly on Wednesday October 19, 2022 at 2:00 PM.

Student number: 5062047

Thesis committee:

| | |
|---|---|
| Prof. dr. ir. C. Poelma, | TU Delft, supervisor and chair |
| Dr. ir. M. J. B. M. Pourquie, | TU Delft, daily supervisor |
| Dr. S. Pirola, | TU Delft |
| Dr. ir. J. W. R. Peeters, | TU Delft |

*This thesis is confidential and cannot be made public until October 19, 2022.*



TU Delft

# Abstract

Nasal airway obstruction (NAO) is one of the most common symptoms in the human respiratory system and causes a considerable financial burden to both individuals and society. Currently, NAO detection is troublesome to achieve, which can influence the accuracy and effectiveness of clinical surgery. Although several objective measurement techniques are currently available, none of them are proven to be consistent with patients' sensations. In recent years, computational fluid dynamics (CFD) has become a novel technique to objectively assess nasal airflow by simulating the nasal airflow of NAO patients. Existing literature has also shown the potential to correlate relevant CFD parameters with patients' sensations. Nevertheless, there is still debate on the numerical setup for an accurate solution and the CFD parameter to correlate with the subjective measurement.

Based on these existing issues, we mainly investigated the boundary configuration (with and without the external nose), the usage of turbulence/laminar models, the usage of steady-state/transient solvers, and briefly discussed the potential of using unilateral pressure drop ratio as a parameter for NAO detection.

To begin with, including the external nose in the nasal airflow simulation is recommended in the nasal airflow simulations. The external nose configuration can affect the flow direction through the nostrils and downstream flow distributions. However, the static (and total) pressure drop only shows a 4% difference compared to the commonly-used plane-truncated boundary configuration. Furthermore, using the laminar model is sufficient for the nasal airflow simulations concerning the static pressure drop prediction. The laminar model shows a difference lower than 15% in static pressure drop compared to the experimental values on 3D-printed nasal airway models. We stress the caution of using the $k-\omega$ model in the nasal airflow simulations because it tends to overpredict the turbulent viscosity ratio near the inlet unphysically. Moreover, steady-state simulations can also reasonably predict nasal airflow. We observed unsteady effects when comparing the steady-state simulation with the transient simulation with a constant flow rate and the transient simulation with a sinusoidal flow-rate-versus-time profile representing the real-life breathing cycle. Nevertheless, the steady-state simulation achieves an accurate prediction in static pressure drop, with a difference lower than 6% compared to the tested transient simulations. The steady-state simulation can also perfectly match transient simulations in the velocity profile of the recirculation zones and require a much lower computational cost. Last but not least, we also tested the possibility of using the unilateral static pressure drop ratio for NAO detection using CFD. However, we note that future studies should make corrections to account for the nasal cycle effect for NAO detection.

Overall, we conclude that including the external nose and using the laminar simulations with the steady-state solver can give an acceptable prediction for the nasal airflow, especially concerning the static pressure drop prediction. We also state that applying CFD in the nasal airflow shows the potential for NAO detection, although future studies may consider making some corrections to include the nasal cycle effect.

**Keywords:** Nasal Airway Obstruction; Physiological flows; CFD; 3D printing.

# Acknowledgement

Every time when I walk through the TU campus, I start to recall those memories I had on every corner here.

My journey began in our department, where the inspiring knowledge has nourished me for the past 3 years. I would like to wholeheartedly thank Dr. ir. Mathieu Pourquie for his guidance throughout my internship project and my M.Sc. thesis. This thesis would not have been possible without his suggestions in both numerical and theoretical analysis. By then I was not experienced in presenting my work, both in speech and written form. His advice made me realize the necessity of presenting. I would also like to truly thank Prof. dr. ir. Christian Poelma for his important advice in the formation of this thesis. His intuition about how to approach the research topic, as well as his intuition about fluid dynamics, really shaped my understanding of scientific research. Furthermore, I would like to express my sincere gratitude to Dr. Frank Datema. As a medical doctor, his passion for fluid mechanics inspired me to apply my knowledge in clinical research. His instructions in anatomy are also extremely helpful for this thesis. Last but not least, I am thankful to the thesis committee. Thank you, Dr. Selene Pirola, for reading and evaluating my thesis report and insights on computational biomechanics. Thank you, Dr. ir. Jurriaan Peeters, for reading and evaluating my thesis report and for the lecture series in Advanced Heat Transfer, one of my first courses in TU Delft.

Entering the laboratory, I started to remember the winter days when I lost myself in the experiments for this thesis. There are so many people that directly and indirectly contributed to this thesis. I would like to thank Dr. ir. Willian Hogendoorn, Dr. Rene Delfos, Ing. Bart Hoek, and Gertjan Mulder for helping with the experimental setup, and to thank dr. Ronald Booij for helping with validating the 3D-printed model.

Walking toward the library where I spent most of my time learning, my mind wandered from 2022 to 2019. I would like to thank all my friends in TU Delft, back home, and across the Atlantic. I would like to express special appreciation to Cristopher, Neel, Ivan, Asif, Abhirath, Teja, Kavya, Sowmya, Ilam, Rafael, and Simin. I will never forget the old days when we worked hard in the library and when we shared laughter near the coffee machine. My days were not bright despite the sunshine in 2022, but you guys were always there to get me through rainfall. Thank you all for always cheering me up and motivating me through the ups and downs. I always hold my love and gratitude to you guys. Most importantly, this journey would not have begun without the unconditionally emotional and financial support from my parents. I am very grateful for everything.

I looked back and saw myself three years back in my head. He was sitting there, making plans for his master's study. I would like to thank him for staying curious and motivated since he arrived here, even after witnessing tree leaves on the campus turn red the third time.

Now my backpack is full, and I know it is time to move forward. Hope I will continue stepping out of my comfort zone forever.

Fulin Yang
September 2022, In Delft

**Easy to do, hard to know.** -*Yuan-Cheng Fung*

# Contents

# 1

# General introduction to the human nasal airway and its obstruction

Since this study hinges on both the medical anatomy of the nasal airway and fluid dynamics of nasal airflow, we will discuss the anatomical structure of the nasal airway involved in the simulations in this chapter, as a supplement to medical knowledge. We advise the readers without a medical background to revisit the content of chapter 1 while reading the following chapters.

## 1.1. Anatomical directions

Before we introduce the anatomical structures of the nasal airway, we will address the anatomical directions frequently mentioned in this study, as supplementary material for readers without a medical background. We recommend Wong et al. (2021) for further details. The terms are explained in the caption of figure 1.1.

## 1.2. Anatomy of the healthy nasal airway

In this section, we will take one of the studied subjects (a healthy subject, FD2) as an example and briefly introduce the anatomy of the healthy nasal airway.

### 1.2.1. Paranasal sinuses and the nasal airway

The entire nasal air passage is defined as the flow field bounded by solid structures of the nasal cavity and the nasopharynx region, which in principle should include the nasal airway and paranasal sinuses. A side view of the entire air passage is introduced in figure 1.2. In the entire nasal air passage, the nasal airway is the main topic of our study, and paranasal sinuses are air cells surrounding the nasal airway, with small openings connected to the nasal airway. We need to clarify that the paranasal sinuses are not included in this study. The reason is that, for people without sinus disease, paranasal sinuses are filled with air and are not directly exposed to airflow from the environment, as described by Jones (2001). It was demonstrated by Xiong et al. (2008) and Kumar et al. (2016) that air change between paranasal sinuses and nasal cavity is not significant. Therefore, in this research, paranasal sinuses are assumed to have no influence on the nasal airflow and thus will be removed as in section 3.1.2.

After excluding the paranasal sinuses, the shape and the location of the nasal airway in the head of a person are shown in figure 1.3. From an engineering perspec-

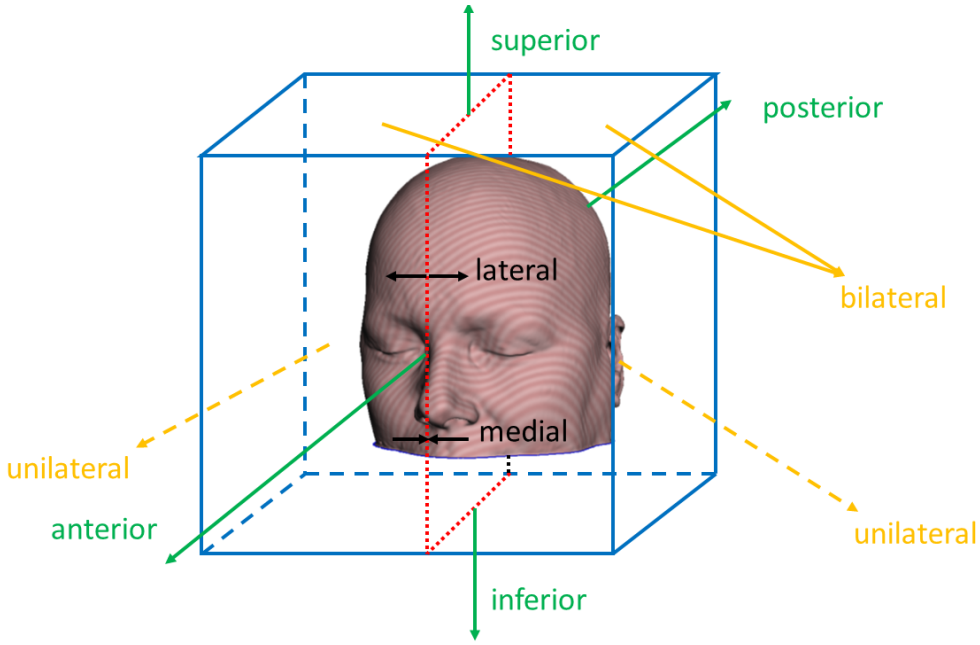


Figure 1.1: Anatomical direction terms are explained with a model of a patient's head. Arrows in the figure represent the direction of the anatomy, and the red plane with dash lines is the "sagittal plane" (meaning the middle plane). Terms of anatomical directions involved in this study are anterior (front)/posterior (back), superior (top)/inferior (bottom), lateral (away from the center)/medial (towards the center). The sagittal plane divides the whole domain into two halves. The airflow on both sides is referred to as bilateral airflow, and the airflow on one side is unilateral airflow.

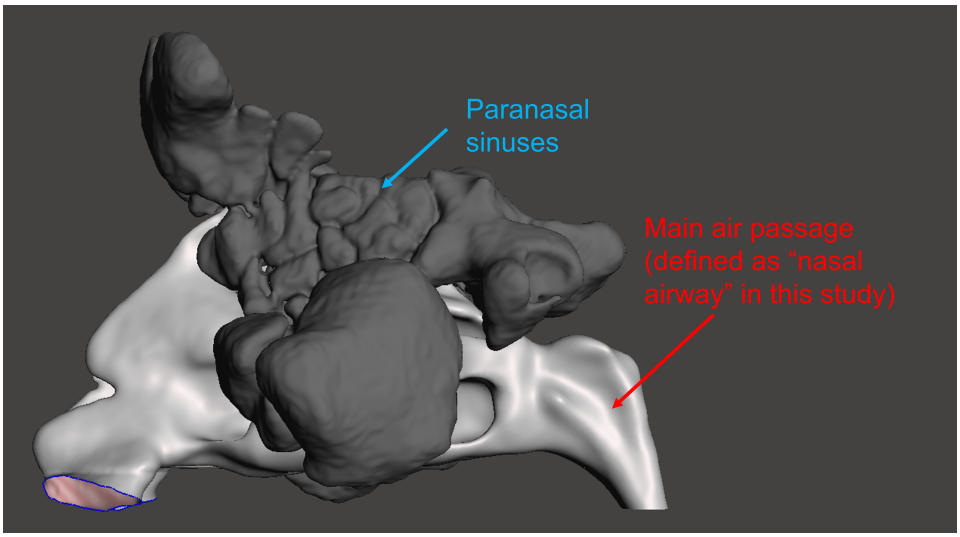


Figure 1.2: The entire nasal air passage in principle contains paranasal sinuses (darker structure in the figure) and the main air passage (also nasal airway, brighter structure in the figure). Paranasal sinuses are cell structures surrounding the nasal airway. Because there is little gas exchange between paranasal sinuses and the main air passage in reality, our discussion on the nasal airway will not consider paranasal sinuses.

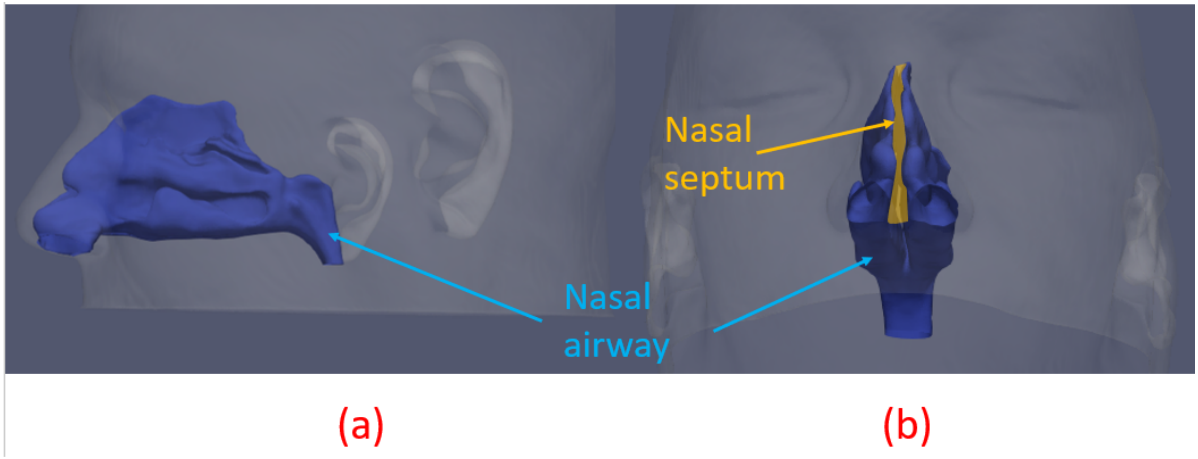


Figure 1.3: The shape and the location of a healthy nasal airway (blue structures) in the head of a person (transparent structures) are shown in (a) side view (from left) and (b) front view. The anatomy of the nasal airway will be further discussed in figure 1.4 using the same viewpoint as in figure 1.3 (a). From figure 1.3 (b), we can see that the nasal cavity shows symmetry in nasal structures between the left and the right side. The nasal airway is separated by the nasal septum at the beginning (see the yellow masked region) and converges after some distance in the posterior direction. For this reason, we will only pick one side (left side) of the nasal airway to introduce its anatomy in figure 1.4.

tive, Mlynski (2013) decomposed the nasal airway generally into three sections by their aerodynamic functions within the inhaling process, namely the inflow area, the functional area, and the outflow area. The position of these three sections, as well as the major nasal airway structures, are shown in figure 1.4. We will also follow this classification and introduce the detailed structures in each area in the following sections.

Again, we should mention that we will only discuss the medical structures relevant to the study in this chapter. We recommend consulting Wong et al. (2021) for further details on the anatomy of the upper respiratory tract.

### 1.2.2. Inflow area

The anterior section of the nasal cavity is the inflow area. The anatomical structures in the inflow area are further visualized by viewing through the nostril, as shown in figure 1.5. The airflow within the inflow area begins at the nostril, which connects the nasal airway with the external environment. The nostril can be seen externally. The nasal vestibule locates internally in the nostril. From a medical point of view, the surface of the nasal vestibule is anteriorly covered by skin structure and posteriorly mantled by a layer of viscous fluid called the mucosa layer. Aerodynamically speaking, the nasal vestibule can redirect the airflow from the environment.

After the vestibule, airflow streams through a narrow section called an internal nasal valve. The shape of the nasal valve can be seen in figure1.5. In principle, the internal nasal valve has the smallest cross-sectional area of the inflow area (see figure 1.4), and in most cases the smallest cross-sectional area of the entire nasal airway. For this reason, the internal nasal valve is a critical structure for nasal airflow. It functions as the throat of a nozzle, located between the converging region of the nasal vestibule and diverging region of the anterior cavum. Because of this particular configuration, airflow accelerates while passing through the internal nasal valve before spreading to the functional area posteriorly (see figure 1.6). This acceleration-spreading effect

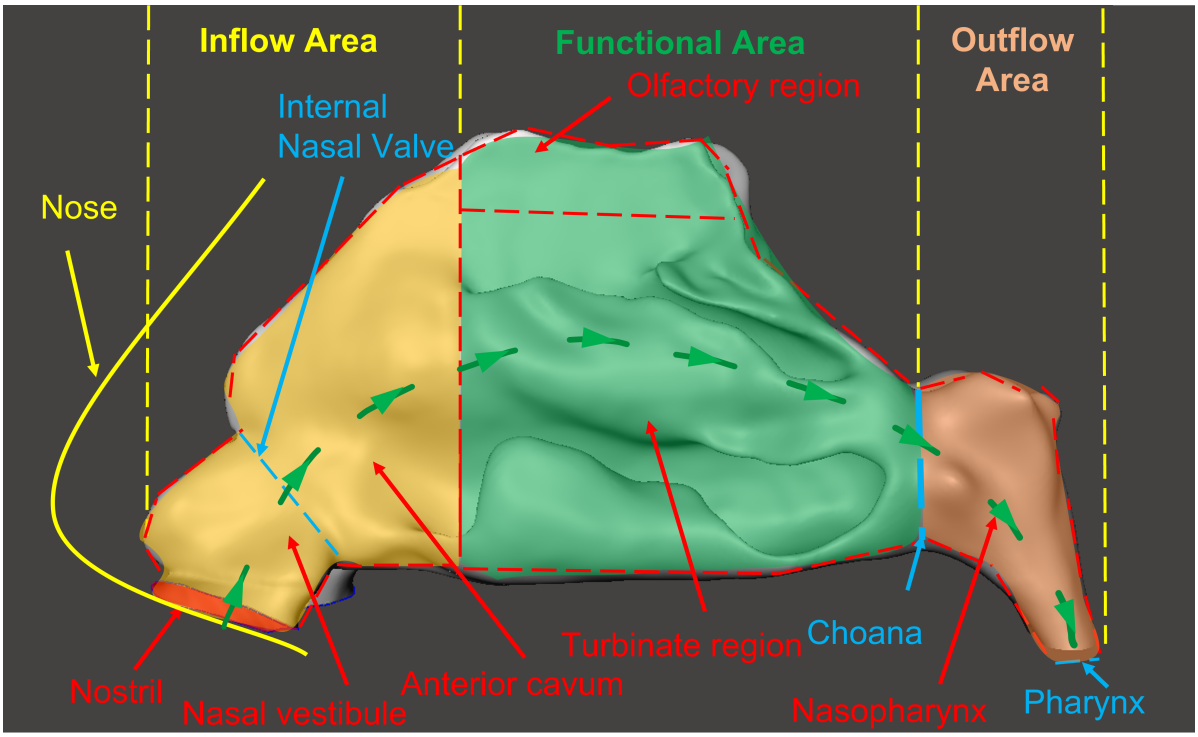


Figure 1.4: To introduce the anatomy of the nasal airway in detail, we borrow the categorization of the nasal airway described by Mlynski (2013) and apply the categorization to one subject in this study. The viewpoint is from the left side, same as figure 1.3 (a). In this figure, the structure in red-color text and arrow indicates that the structure is visible from the side view, and the structure in blue-color text and arrow indicates that it is invisible from the side view. The green arrows represent the mean flow direction during the inhaling process. Mlynski (2013) divided the entire nasal airway into three areas: inflow area (masked in yellow), function area (masked in green), and outflow area (masked in orange). Each person has one inflow area and one functional area on each side of the nasal airway. The inflow area (introduced in section 1.2.2) is a converging-diverging configuration containing the nostril, the nasal vestibule (converging part), the internal nasal valve (minimal cross-section), and the anterior cavum (diverging part). The functional area (introduced in section 1.2.3) is mainly the turbinate region and the olfactory region. The choana, which works as a transition for both sides of the nasal airway to converge, is located between the functional area and the outflow area. The converged flow from upstream then enters the nasopharynx region in the outflow area (introduced in 1.2.4), and then leaves the human upper airway through the pharynx.

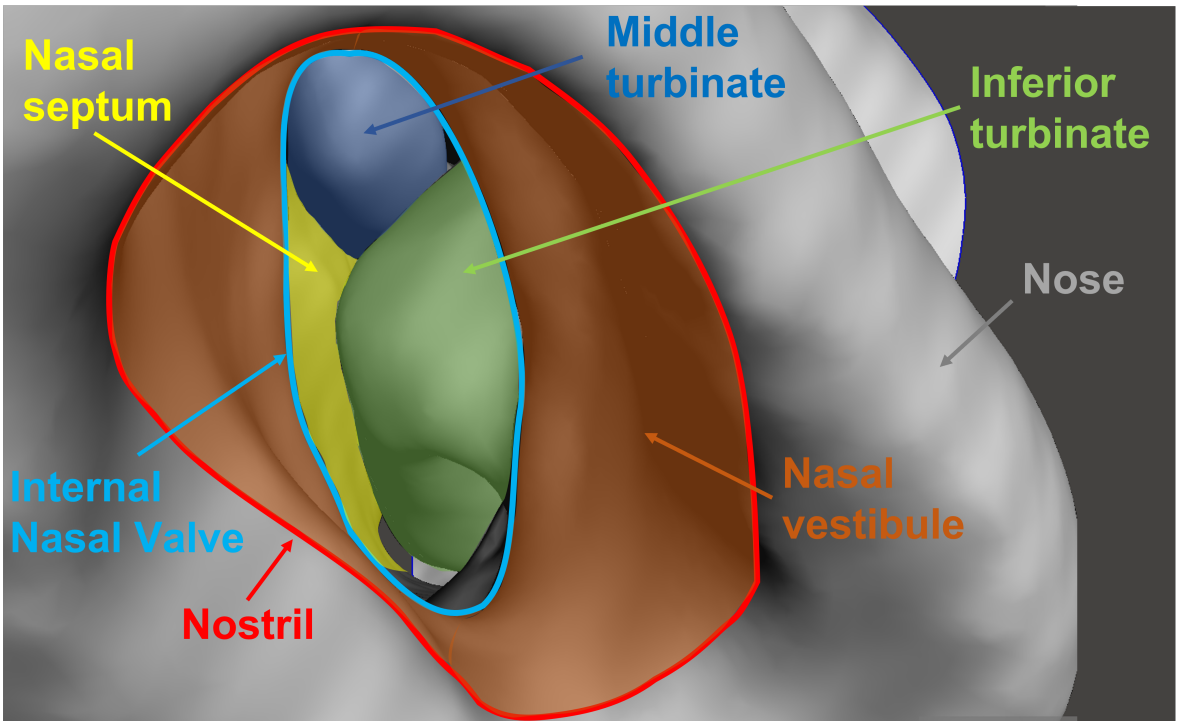


Figure 1.5: Since the internal nasal valve is not visible in the side view of figure 1.4, we select our viewpoint through the nostril to visualize the shape of the internal nasal valve. In this figure, the masked region is the solid structure, and the circled region is the airway. As seen in the figure, the nostril is located externally, connecting the nasal airway with the environment. The nasal vestibule is a converging geometry, located between the nostril and the internal nasal valve. The internal nasal valve has a minimal cross-section area in the inflow area, which is also visible in figure 1.4. The structures behind the internal nasal valve will be introduced in section 1.2.3, where we can see the head of the inferior turbinate and the tip of the middle turbinate. Towards the medial direction, we can see the nasal septum which separations both sides of the nasal airway.

is also referred to as “inspiratory jet” effect, as described by Taylor et al. (2010) and Doorly et al. (2008b).

The anterior cavum functions as a diffuser, spreading the airflow over the entire functional area posteriorly. As one may know, above a certain cone angle ($15^\circ$ as described by White (2011)) for a diffuser, flow separation happens. A similar effect can also be noticed inside the anterior cavum region. Especially within the superior part of the anterior cavum, existing literature visualized a recirculation zone downstream of the internal nasal valve, because of the converging-diverging configuration in the inflow area, such as the experimental work using dye visualization and PIV by Doorly et al. (2008b) (see figure 1.6). In addition, Doorly et al. (2008b) discussed the flow irregularities from the interaction between the main flow and the recirculation zone, which is the source of unsteadiness even under the laminar flow condition. The airflow then enters the second aerodynamic area: the functional area.

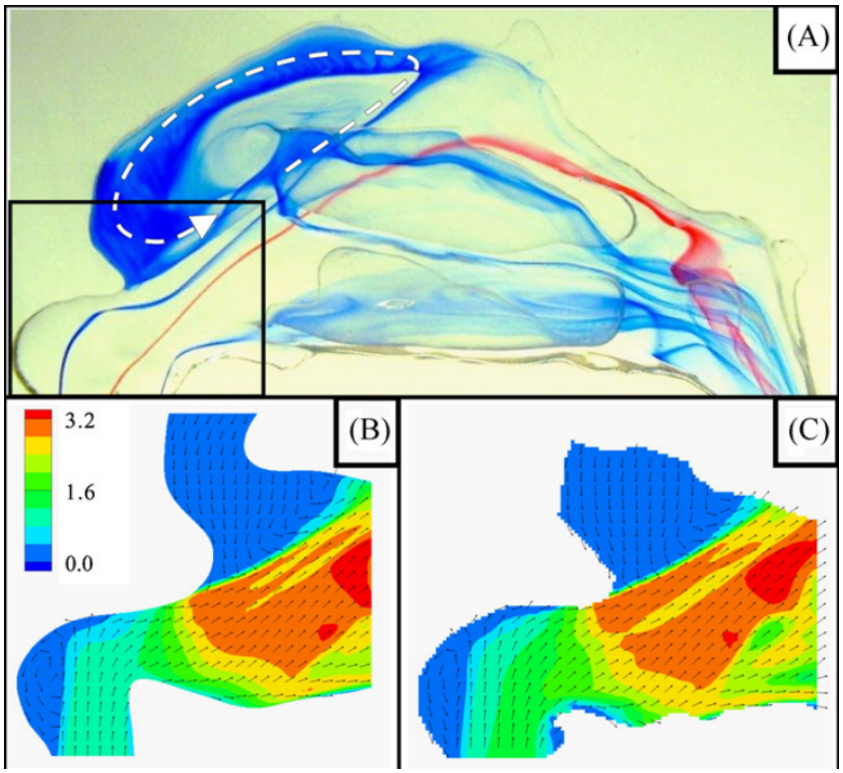


Figure 1.6: The visualization of the flow field within the anterior cavum. The figure is reproduced from Doorly et al. (2008b). Figure (A) is the dye visualization of the flow field during the inspiratory process. A recirculation zone originating from the internal nasal valve up to the olfactory region is noticed in the flow field, represented by a white arrow. The internal nasal valve region is zoomed in and particle image velocimetry (PIV) measurement of this region is shown in (C). In comparison, (B) is the numerical simulation of the velocity field under the same flow conditions. In both figures (B) and (C), the color of the contour represents the velocity magnitude. Because of the minimal cross-section area of the internal nasal valve, both PIV and numerical simulation show that the flow accelerates when passing through the internal nasal valve and spreads downstream, as seen in the velocity contour. This indicates that the airflow passing through the internal nasal valve forms a jet flow pattern (thus the so-called “inspiratory jet”) and drives the recirculation zone.

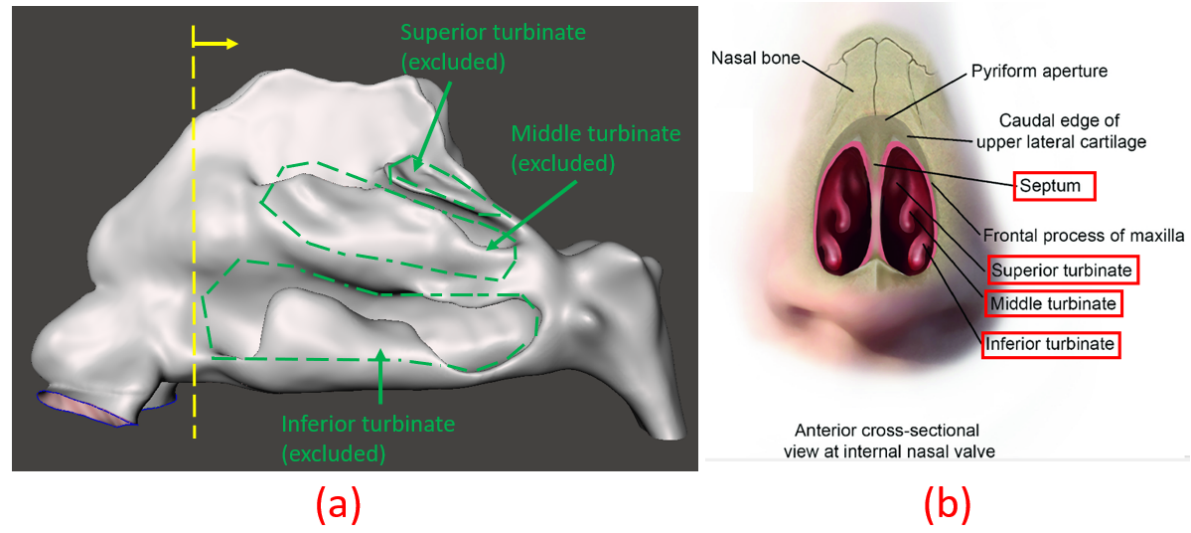


Figure 1.7: The side view of the nasal airway (figure 1.7 (a)) and the front view of its surrounding solid structures (figure 1.7 (b)) in the turbinate region are visualized. In figure 1.7 (a), the circled-out region in green represents the hollow structure in the nasal airway because of the presence of turbinates in the nasal cavity. If we take the cross-sectional view from the yellow dash line in figure 1.7 (a), three types of nasal turbinates can be seen in figure 1.7 (b). Figure 1.7 (b) represents the solid structures in the nasal cavity adapted from Wong et al. (2021), and we marked the relevant structures in red squares. In figure 1.7 (b) we learn that there are two pairs of droplet-shaped superior, middle, and inferior turbinates on both sides of the human nasal cavity away from the nasal septum.

### 1.2.3. Functional area

As seen in figure 1.4, the functional area contains the turbinate region and the olfactory region. It undertakes the functions of olfactory, warming, and humidifying the inhaling airflow. Also, in figure 1.4, the olfactory region is located above the turbinate region. Essentially, the olfactory region contains odor sensors connecting to the human brain, making people sense smell from environmental air. Previous work and research articles such as Doorly et al. (2008b) and Casey et al. (2017) have shown that the airflow rate passing through the olfactory region is around 11% of the total airflow rate, much smaller than the flow rate through the turbinate region (89% of the total airflow rate).

Compared with a lower flow rate in the olfactory region, a large proportion of airflow passes by the turbinate region, allowing the nose to rapidly humidify, clean, and heat external air. A feature of the turbinate region, as seen in figure 1.7 (a), is its complicated shape caused by the existence of three solid structures: superior, middle, and inferior turbinate. The anatomical structure of nasal turbinates is shown in figure 1.7 (b). The airway adjacent to those three turbinate structures is often referred to respectively as superior meatus, middle meatus, and inferior meatus (meatus means passage), which are shown in figure 1.8 (b). The middle turbinates and superior turbinates are connected to paranasal sinuses, which were removed and therefore not visible in these figures.

### 1.2.4. Outflow area

After the unilateral airflow passes through the turbinate region, each side of the nasal airflow enters the outflow area through the choana. The airflow on both sides gathers again when reaching the nasopharynx, and finally, leaves the nasal airway from the pharynx. The configuration of the nasopharynx is revisited in figure 1.9 (a) and (c),

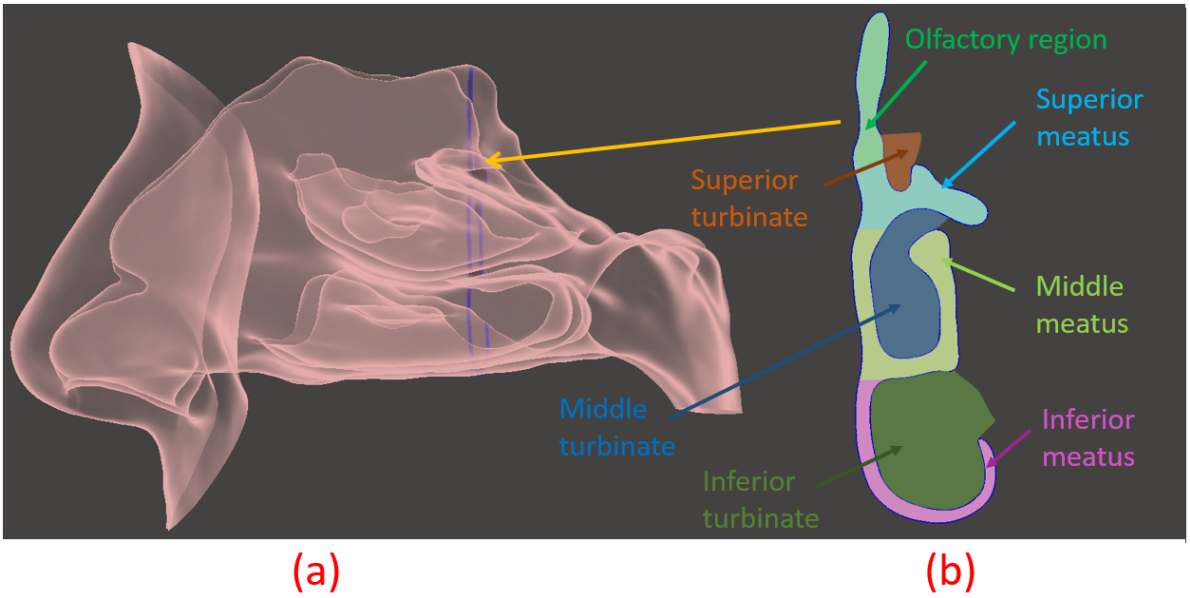


Figure 1.8: For one axial slice (along anterior-posterior direction) in figure 1.8 (a), the nasal meatus (airway adjacent to the turbinate region) is shown. Superior, middle, and inferior meatus are respectively the airway adjacent to the superior, middle, and inferior turbinate. The location of the three nasal meatus regions can be seen in figure 1.8 (b).

and the shape of the choana and pharynx are shown in figure 1.9 (b).

Similar to the internal nasal valve, the choana region is another site with minimal cross-section area, connecting the converging geometry of the functional area and the slightly-diverging geometry of the nasopharynx. This can be seen in figure 1.9 (b). The airflow is redirected by the bend and then reaches the trachea, the beginning of the human lower respiratory airway. Since in this research, we are only interested in the inspiratory process within the upper airway, the pharynx plane is the ending boundary of our study.

### 1.2.5. Nasal cycle

Up to now, we have introduced all the anatomic structures of the human nose. However, normally the geometry of the nasal cavity is not stationary. For $70-90\%$ of the population, there exists a dynamic phenomenon inside the human nose, meaning that the geometry of the unilateral nasal airway will shrink or expand with time, corresponding to alternating physiological congestion or decongestion state unilaterally. This was reported by Pendolino et al. (2019) and Kahana-Zweig et al. (2016). The duration of each nasal cycle varies among people, ranging from 1.5 to 4h. This means that, for a person at one moment, it is possible that one side of the nose is in a decongestion state while the other is in a congestion state. After a certain time, the congested side will be decongested and vice versa.

In this study, we will not make any corrections to the nasal cycle effect for two reasons. The first reason is that the requirement on the CT scans is demanding to study the nasal cycle. To the best of our knowledge, the existing research for nasal cycle simulations requires the CT scan (or MRI) of the same patient under different states of the nasal cycle, such as in Patel et al. (2015) and Jo et al. (2015). Taking multiple CT scans on one patient without medical indications is difficult because of

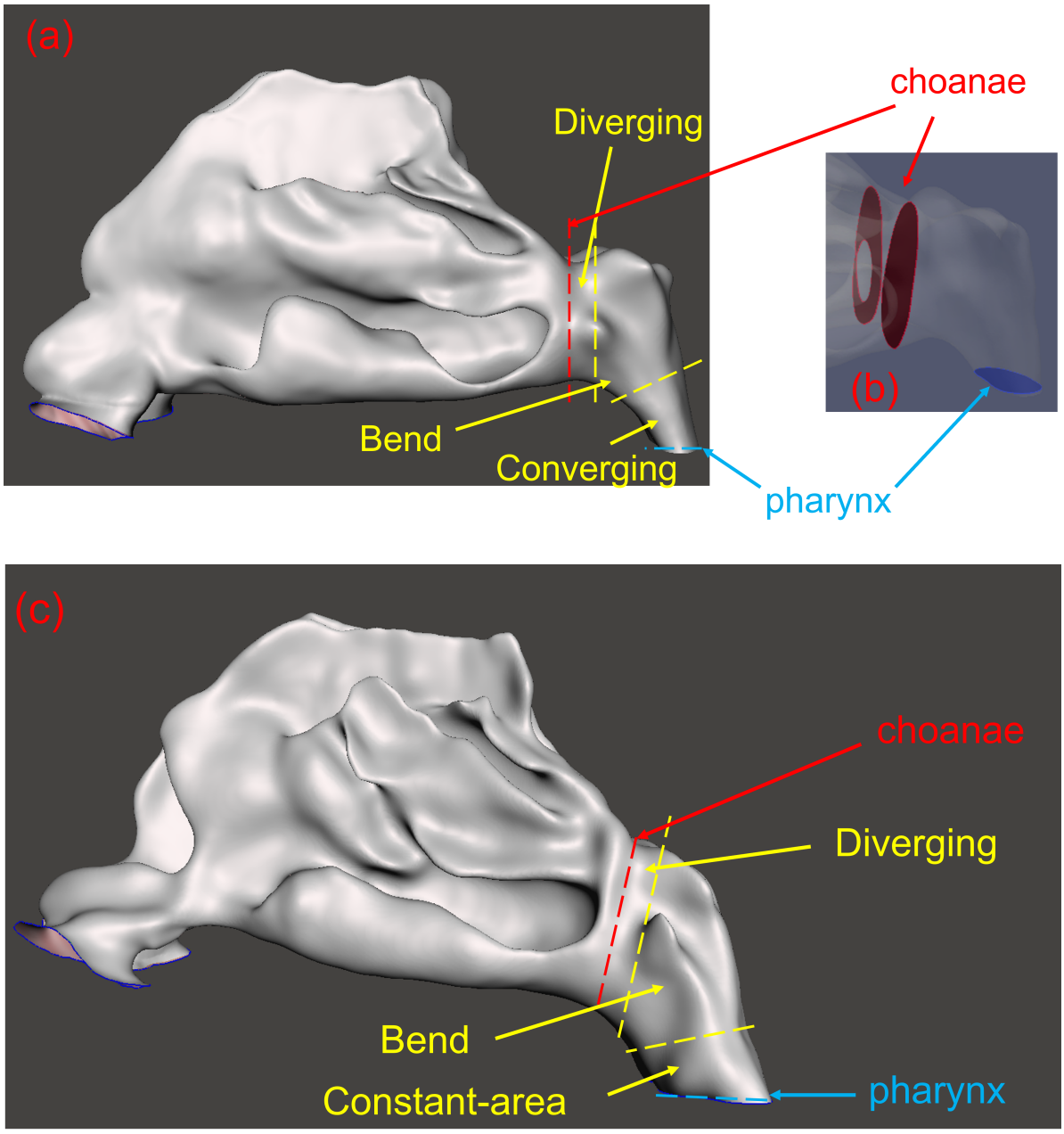


Figure 1.9: Three types of geometrical configuration are identified in the nasopharynx area. As seen in figure 1.9 (a), the first section is the slightly-diverging section, starting from the choanae, then the geometry has a bend to direct the flow downwards. Near the pharynx, the geometry can vary from a converging to an almost constant-area configuration, depending on the subject. For the example subject (FD2) in this section, the geometry near the pharynx is converging, as seen in figure 1.9 (a). However, for another subject (scan2, NAO subject) discussed in later sections, the geometry has an almost constant cross-section area, as seen in figure 1.9 (c). For the healthy (FD2) subject, the shape of the airway for choanae (both sides of the choana plane) and the pharynx is visualized in figure 1.9 (b).

the concern of radiation dose. For this reason, CT scans of the same patient were unavailable during the course of the study. The second reason is that the subjective sensation of congestion usually is not correlated with the area variation from the nasal cycle effect, as stated by Wong et al. (2021). This can be explained by the fact that the “ensemble average” (time-average and bilaterally average) of the cross-section area usually remains constant. Therefore, people are less likely to complain about the congestion caused by the nasal cycle.

## 1.3. Background of nasal airway obstruction

### 1.3.1. Impact of nasal airway obstruction on individuals and society

The nasal tract is a vital part of the human respiratory system. It acts mainly as an air conditioner so that the lungs receive humidified, heated, and cleaned air. However, the human nose is not always well-functioning. A certain number of people are suffering from impaired nasal function by many types of causes, such as nasal obstruction, sinus pain, and an absent sense of smell. In the United States alone, nasal sinus disease resulted in an expense of approximately 6 billion dollars in 2009, as reported by Zhao et al. (2014). Of all major symptoms, nasal airway obstruction (NAO) was estimated by Stewart et al. (2010) and Rhee et al. (2005) to impact more than 20 million Americans and to account for 5 billion dollars annually on medication for helping to relieve an obstruction sense, with an additional financial burden on surgery. From the patient’s point of view, the feeling of congestion during each breathing cycle could have a huge influence on the quality of life, as reported by Rhee et al. (2003). In summary, nasal airway obstruction has caused financial and life-quality difficulties for both individuals and human society.

### 1.3.2. Anatomical cause of nasal airway obstruction

Existing research, such as Ricci et al. (2001), has shown several common anatomical reasons for NAO, including septal deviation, nasal valve collapse, and nasal turbinate hypertrophy. Among those, because the studied CT scans (will be introduced in section 3) are both caused by septal deviations, we will only introduce the anatomical cause of the septal deviation. We refer the reader to consult Siu et al. (2021) for general NAO causes, Schatz et al. (2014) for NAO subjects caused by nasal valve collapse, and Whyte et al. (2020) for NAO subjects caused by nasal turbinate hypertrophy.

Septal deviation literally means a deviated nasal septum. It can be caused by external forces or genetic factors. Anatomically speaking, septal deviation happens in the inflow and (or) the functional areas, leading to abnormal airflow in these regions. As an example, a healthy subject and a subject suffering from septal deviation are discussed in Mohapatra et al. (2017). CT scans of both subjects are given in the figure 1.10. Figure 1.10 (A) is a coronal CT-scan slice (the left side of the picture is the right nasal cavity for the patient, and vice versa), there is a moderate septal deviation to the left. Compared to the symptomatic side, Figure 1.10 (B) is the anatomy of the healthy nasal septum. It is obvious that the nasal airway in Figure 1.10 (A) is distorted, and the patient will experience obstruction because of the deviation.

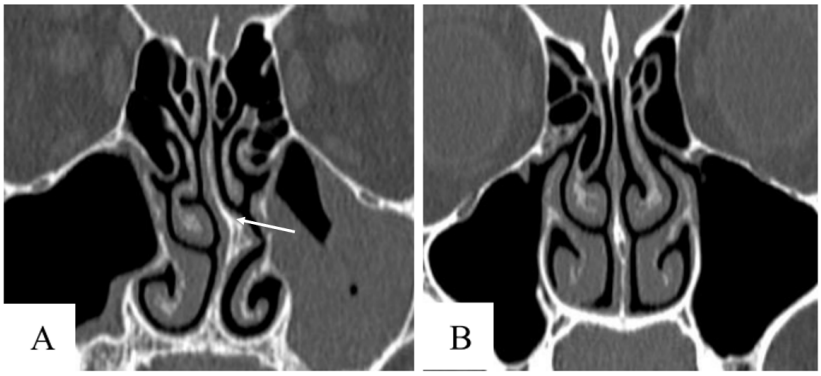


Figure 1.10: CT-scan of a septal deviation patient (A) and a healthy person (B), adapted from Mohapatra et al. (2017). In a CT scan, the black region is the airway, the gray region is the soft structures, and the white area is the bone structures. A brief introduction regarding CT scans can be found in section 3.1.2. In figure (A), the nasal septum (labeled with a white arrow) deviates to the left, causing the airway in the middle-inferior meatus to change. In comparison with the pathological case, the healthy nasal septum in figure (B) is almost straight.

Furthermore, studies such as Clark et al. (2018) show that it is highly possible for one patient to have multiple anatomical causes, such as having both nasal valve collapse and septal deviation. Such confounding causes indeed increase the difficulty to diagnose and furthermore to develop a treatment plan.

### 1.3.3. Existing techniques for diagnosis and limitations

Since there are many possible reasons for NAO to happen, in order to perform an appropriate operation for each individual, the primal task is to find out the specific reason for the NAO symptoms. To this end, the clinical surgeon will first arrange a series of pre-operative nasal function assessments. After viewing the patient's medical record, the initial techniques for clinicians to utilize to evaluate a patient's nasal anatomy are usually endoscopy. These enable doctors to visualize the situation of the anterior nose (nasal valve) and posterior nose. Medical imaging is also applied frequently, especially with computed tomography scans (CT scans) and rarely with magnetic resonance imaging (MRI).

To evaluate the severity of the obstruction, there are contributions from the patient's side as well. Subjective and objective measurements of patients are often requested by clinicians to assess the severity of nasal obstruction.

1. **Subjective measurement tools**:
   Subjective measurement tools, also called Patient-Reported Outcome Measures (PROMs), are usually present in the form of questionnaires. Prevailing subjective measurement tools include the Nasal Obstruction Symptom Evaluation (NOSE) scale and the visual analog scale (VAS). Both subjective measurement tools assess NAO by asking patients to rate their own NAO severity with scores. From the clinical effectiveness point of view, Rhee et al. (2014) concludes that both score systems are clinically effective. A subjective measurement tool can represent the true sensation of the patient and therefore is a valid tool for clinicians to evaluate the severeness of NAO subjectively. However, no further objective information can be deduced from subjective measurements, such as the location of obstruc-

tion or the resistance during breathing. Therefore, objective measurement tools are often utilized by clinics.

2. **Objective measurement tools**:
   Objective measurement tools are devices for measuring physical parameters during the inhaling process, such as nasal resistance or flow rate. Nowadays, there are many existing techniques to objectively detect a nasal obstruction, including peak nasal inspiratory flow (PNIF) to measure flow rate, acoustic rhinometry to measure cross-section area over depth, and rhinomanometry to measure nasal resistance. Nasal resistance will also be mentioned in section 2.3, which can be calculated from

$$R = \frac{\Delta p}{Q}, \tag{1.1}$$

   where $\Delta p$ is the unilateral static pressure drop, calculated by the difference between the static pressure of the nostril and the static pressure of the pharynx, and $Q$ is the flow rate.

   After unilateral nasal resistance ($R_L$ for the left side and $R_R$ for the right side) measured by rhinomanometry is obtained, bilateral nasal resistance ($R_{bi}$) is calculated from an Ohm's law analogy:

$$R_{bi} = \frac{R_L R_R}{R_L + R_R}. \tag{1.2}$$

   The bilateral static pressure drop is calculated using a similar principle to calculate the electrical resistance of a circuit in parallel, where airflow on both sides of the nose is analogous to the electric current in a parallel configuration. The post-processed bilateral nasal resistance will be compared with the established healthy range, from which the clinician will identify if the patient has NAO. For the detailed comparison procedure, it is advisable to refer to the Ph.D. thesis by Thulesius (2012).

3. **Correlation between objective tools with subjective measurement**:
   One question still remains unanswered: since there are two categories of measurement tools, how far can we use an objective tool to predict NAO? Since subjective measurement tools such as NOSE or VAS scores are often considered a direct interpretation of a patient's sensation, the above question can be partly answered by the correlation between subjective and objective measurement. To obtain the statistically important correlation, existing literature regularly involves many candidates to create large data samples. The correlation is obtained using objective tools, subjective measurement scores, and statistical analysis (for example, the Pearson correlation coefficient and linear regression). Andre et al. (2009) reviewed 16 studies published from 1989 to 2006, investigating the correlation between subjective scores and parameters from objective tools, including rhinomanometry and acoustic rhinometry. Especially for rhinomanometry, they concluded that the correlation between the pressure-flow relation and subjective scores still remains uncertain. Out of 8 studies involving the relationship between subjective scores and bilateral nasal airway resistance, no correlation is reported in four studies. They concluded that there is no consensus about the correlation

between objective measurement and subjective scores. Furthermore, Yepes-Nunez et al. (2013) conducted a study involving 184 candidates to establish the correlation between different subjective techniques (symptom score and VAS), and different objective tools (rhinomanometry, acoustic rhinometry, and PNIF). They found a moderate correlation between the selected two subjective tools, moderate to strong correlation among the tools from the objective category, and a weak correlation between subjective tools and all the objective tools in this study.

From the above studies, we notice that there is no strong correlation between subjective and objective measurement tools. Considering that different objective measurement tools would correspond to different output parameters, it is important to develop a more comprehensive objective measurement tool, through which a better correlation with the patient's sensation could be achieved.

### 1.3.4. Limitations of existing techniques

Through the assessment mentioned above, clinicians will try to identify the possible location for obstruction, guided by which they will conduct surgeries. However, as reported by Zhao et al. (2014), because of the uncertainty of objective measurement tools, NAO surgeries often rely on the clinicians' personal experience and intuition. As a result, although NAO surgery has been applied in millions of cases, its successful rate still has huge space for improvement. A short-term study by Samad et al. (1992) reported that NAO surgery only has approximately 70% chances to succeed. A long-term study by Sundh et al. (2015) reported even higher chances to fail, with 53% of the cases claiming nasal obstruction right after receiving the nasal surgery and 83% recurs nasal obstruction symptoms 3 to 5 years after the surgery. Up to now, clinicians have been expecting an objective measurement tool with more reliability to increase the success rate of NAO surgery greatly.

Understanding the patient-specific nasal airflow might physically explain why patients feel the obstruction. To this end, both experimental work and numerical simulation of the nasal airflow are carried out. Especially with the development of medical imaging and computational fluid dynamics (CFD), from the beginning of the 1990s up till now, applying CFD techniques to nasal airflow has become a key research topic. The real-life nasal airflow can be simulated and visualized using CFD by reconstructing the patient-specific nasal airway from medical imaging. Therefore, by physically understanding the nasal airflow of NAO patients, CFD is expected to become the next objective tool for nasal obstruction measurement in clinical use.

# 2

# CFD to simulate nasal airflow: An overview

## 2.1. Introduction

The shortcomings of the current NAO detection tools motivate us to develop a CFD workflow as an alternative objective measurement tool for NAO detection. This chapter will review the general methodology from existing literature and its limitations. We should first learn how the nasal airflow is simulated and its limits to detect NAO using CFD. This motivates us to assess the appropriate numerical setup for CFD to be applied in the nasal airflow. Next, we will address the current issue of applying CFD for NAO detection, which clarifies this study's focus and potential outcome.

## 2.2. General procedure for modeling

Of all the earlier attempts to utilize CFD techniques on nasal airflow, Elad et al. (1993) and Keyhani et al. (1995) obtained instructive results and inspired many researchers on nasal airflow simulation. Elad et al. (1993) developed a nose-like model with unilateral trapezoidal cross-section and rectangular-shaped nasal turbinates. Because the geometry is extremely simplified and shape details of the nasal cavity are not preserved, their computational mesh is a structural mesh with a few thousand cells. In comparison, Keyhani et al. (1995) was the first to use a reconstructed 3D airway model from a CT scan in a CFD simulation. They also experimented with using a scaled physical model for validation. Under the same flow condition assumption as Elad et al. (1993), computational results achieved by Keyhani et al. (1995) show acceptable agreement with experimental results, considering flow pattern and percentage of flow passing through the different structures.

Although the results of both articles above can be improved after decades of rapid development in computational techniques, later research adopted their general procedures of modeling nasal airflow with CFD: 1. to reconstruct a 3D model from a CT scan; 2. to generate a computational mesh from the 3D model geometry and 3. to model and solve the flow field with CFD.

Following these three steps allows reconstructing nasal airflow with a CFD simulation. However, some parameters and necessary assumptions in modeling the nasal airway could cause the simulation result to deviate from reality. In the next section, we will discuss previous work aiming at studying such settings in general procedures.

### 2.2.1. Reconstructing 3D model from CT-scan

In the reconstruction procedure, the following two assumptions are commonly made.

The first assumption is that the reconstruction procedure does not consider any dynamical deformation of the nasal structure because CT scans are taken instantaneously. As a result, two physical processes are excluded if a CT scan is used: nasal cycle and fluid-structure interaction (FSI) during the respiratory process. The reasoning for ruling out the nasal cycle effect has been discussed in section 1.2.5, and now we focus on validating the FSI process during inhaling and exhaling. O'Neill et al. (2019) developed a mathematical model to describe the deformation of the nasal cavity caused by the inhaling airflow and a rigid-wall model for comparison. Their model was validated using experimental data. The result shows that a minor pressure drop corresponds to a lower flow rate difference between a rigid and compliant wall model. The deformation effect on the nasal airflow gives only 5% of the flow rate difference compared to rigid-wall approximation for a driving pressure drop of 150 Pa. A 150 Pa pressure drop corresponds to around 18 L/min unilateral flow rate, which is larger than the maximum unilateral flow rate in our study (12 L/min). Therefore, we would expect a smaller pressure drop difference between the compliant wall model and the rigid wall model under the flow rate range of this study. We will introduce our studied range of the flow rates in section 2.2.3. Here it is important to note that, for the current study, because the deformation of the nasal airway is not strong in the flow rate range of this study, we will not consider fluid-structure interaction.

The second assumption is that the removed structures during the reconstruction procedure cause minor effect on the flow field. If we trace back the reconstruction procedure, one primary structures is constantly neglected: the external nose structure at the inlet.

The influence of including the external nose in the configuration of the inflow boundary might be considerable. Existing research models the nasal airflow with various choices of the inflow boundary profile configurations. The most common approach is defining a flat plane within the nasal airway as the inlet, leaving out the external nose and part of the nasal vestibule, as seen in the figure 2.1. Such setup can be seen in earlier literature such as Wen et al. (2008), Wang et al. (2014), and also literature nowadays such as Tretiakow et al. (2020), Bruning et al. (2017), and Hildebrandt et al. (2019). To the best of our knowledge, one benefit of such a configuration is that the plane inlet is easier to obtain. Nostrils and external air are geometrically connected in a CT-scan and are difficult to distinguish from each other. In this case, the most direct approach would be to truncate the connection between the nostril and the external air using a specific slice, which forms a plane inlet profile. Compared to the plane inlet configuration, adding the external nose (in figure2.1) into the simulation will require more technical effort, such as defining the inlet boundary of the flow field. However, such configuration is considered the most comprehensive approach, including all necessary features of nasal airflow. The application of the external nose into nasal airflow simulation can be seen in Van Strien et al. (2021) and Xiao et al. (2021).

However, none of the above articles justified the usage of such inflow boundary profile configurations. One article that systematically compared the influence of inflow boundary configuration is Taylor et al. (2010). They demonstrated the effect of the external nose by numerically simulating different models with a plane-truncated inlet profile, a pipe-extended inlet profile, and an inlet profile, including the external nose. The first two profiles ignore the effect of the external nose, thus reducing the

effort spent on reconstructing it from a CT scan. Under restful inflow conditions, they recorded a minor pressure drop difference with an order of 10% between the plane-truncated and the external nose profile. However, considering wall shear stress or intranasal flow distribution, the selection of inlet boundary profiles greatly impacted simulated nasal airflow. Although they selected a plane inlet and inlet with an external nose and compared the effect of inflow configuration on wall shear stress and pressure drop, the boundary condition they prescribed is a constant velocity profile at the inlet. This setup implies that the flow goes into the nasal airway uniformly throughout the nostril, which would be a strong assumption. This motivates us to compare the effect of inflow boundary configurations in this study.

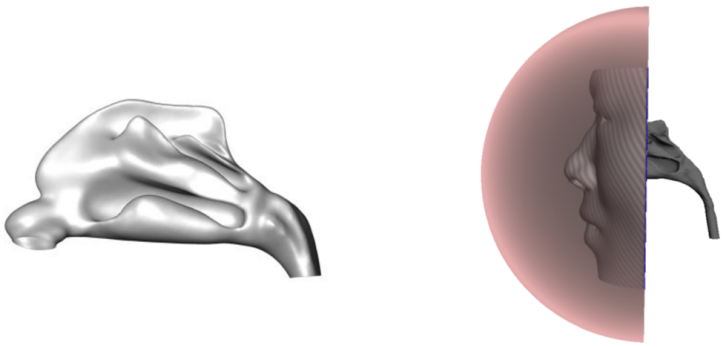

(a) (b)

Figure 2.1: Common inflow boundary profile, as selected in the existing literature. Figure (a) shows an example of a plane inlet boundary configuration from Hildebrandt et al. (2019). In figure (b), the inflow profile of the nasal airway is different from the inflow profile in the plane inlet case, caused by the existence of the external nose. Figure (b) is adapted from the supplement material of Van Strien et al. (2021). In their configuration, the whole face is modeled. However, other parts of the face, excluding the nose region, are far away from the region of interest and could be considered unimportant.

### 2.2.2. Mesh generation

Because of the complex shape of the nasal cavity with sharp edges and multiple bends, mesh generation could be difficult and time-consuming. Although a structured grid with the same connectivity for each cell, to some extent, reduces computational error, the unstructured grid is frequently applied in the nasal cavity simulation, reported by Lintermann (2020). This is because the generation of an unstructured grid can capture the complicated geometrical details in the case of the human nasal airway. Several tools are available in common CFD packages for automatic unstructured mesh generation, such as CFMESH (to generate hexahedral-based internal cells and prism layers) and snappyHexMesh (to generate multiple types of cells with hexahedral background mesh) packages in OpenFOAM software, or TGrid package in ANSYS software.

One of the critical parameters in the mesh generation process is the grid size. Frank-Ito et al. (2016) systematically investigated the grid independence in the nasal airflow for tetrahedral-only meshes, as well as the effect of adding different numbers of prism layers to a tetrahedral mesh on the resolution of the particle deposition. They recorded a minor difference in flow variables (flow rate under fixed inlet-outlet pressure

drop and the pressure drop within the inflow and functional area) for 4 million and larger grid sizes. At the same time, the velocity profile at a certain location still has a visible difference, even with a grid size larger than 4 million. Nevertheless, they suggested that a grid dependency study should be performed for any purpose of the nasal airflow simulation. To examine the resolution of the mesh, we will also test the grid independence in our study.

### 2.2.3. Setting up the physical model

In reality, the breathing process is random. In addition, it is very difficult to categorize the regime of the nasal airflow. To model the nasal airflow, some approximations are constantly introduced in existing literatures. In this section, we will justify the usage of these approximations.

- **Unsteadiness:** During the inhaling process, the human has a non-constant inhaling flow rate with respect to time, and it would be laborious to record the flow rate profile of each patient individually. The time-varying flow rate inherently causes the flow field of the nasal airway to be unsteady in nature. However, for calculation simplicity, current research tends to conduct steady simulations directly, which needs some justification. For this reason, we will discuss the time-variability of the breathing process.

  We breathe with a different flow rate profile in time for every breathing cycle. Early medical research by Lafortuna et al. (1984) obtained a statistically averaged function of more than 2000 breathing cycles. They have shown that flow rate during both rest and exercise shows a periodic variation with time in the inhaling and exhaling process, which can be approximated by a sinusoidal wave function. Especially for the inhaling process, the real flow rate versus time function and the approximating sinusoidal function can be seen in figure 2.2. Two branches can be distinguished. The increasing branch with time (at 0 to 50 on X-axis) is called the inclining phase, and the decreasing part (at 50 to 100 on the X-axis) is called the declining phase. In this figure, points with error bars are measured flow rate data. From this data, an equivalent sinusoidal function is calculated in the form of the following equation,

$$\dot{V}_{sin}(t) = V_{max} sin(\frac{\pi}{T_0} t), \tag{2.1}$$

  where $V_{max} = \frac{\pi}{2T_0} \int_0^{T_0} \dot{V}(t)\, dt$ is the peak flow rate, and $T_0$ is time in each inhaling cycle. This equation assumes that the total air volume within one inspiration period is the same for a real-life flow rate profile and a sinusoidal profile approximation.

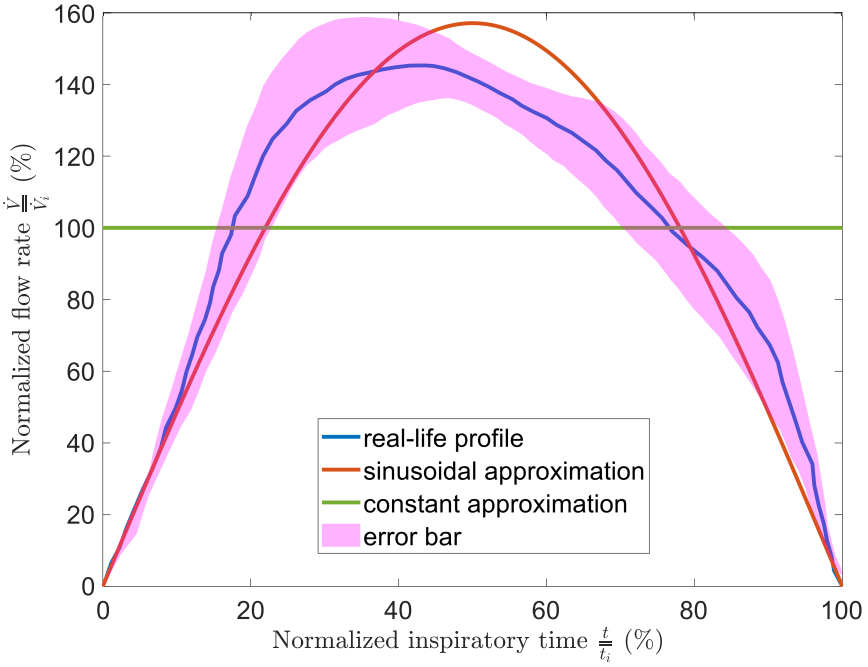


Figure 2.2: Comparison of measured inhaling flow rate (points with error bars), equivalent sinusoidal function (solid line), and mean flow rate (dash line) varying with time. The figure is adapted from Lafortuna et al. (1984). Two variables of this figure, namely flow rate and inspiratory time, are normalized. On the y-axis, $\dot{V}$ is the time-varying flow rate, and $\overline{\dot{V}_i}$ is the mean flow rate. On the x-axis, $t$ is time, and $\overline{t_i}$ is the inspiratory time for each breathing cycle.

In addition, another common approach to further simplify the inflow profile is to directly assume a constant inhaling flow rate with time, using constant mean flow instead (see dash line in figure 2.2). Mean flow rate $\overline{\dot{V}_i}$ is calculated by

$$\overline{\dot{V}_i} = \frac{2}{\pi} V_{max}. \tag{2.2}$$

Equation 2.2 is derived from the premise that the total air volume is the same for different inhaling profiles. A well-accepted range of mean flow rate $\overline{\dot{V}_i}$ , introduced by Anderson et al. (2006) and Rennie et al. (2011), is: from 9.6 L/min to 24 L/min under restful conditions, and from 24 L/min to 120 L/min under sniffing and exercising conditions.

A transient simulation with a steady respiratory flow rate is also referred to as quasi-steady simulation by Doorly et al. (2008b) and Xiao et al. (2021). In addition, since the flow rate is now constant in time, most of the existing research takes a further step to simulate the inhaling process in a steady state completely. The motivation is that transient simulations for nasal airflow are very time-consuming. Because the nasal airway has a complex geometry, it requires more mesh to preserve its surface. In addition, because the length scale of the nasal airway is very small (the order of magnitude for volume is $10^{-5}\ m^3$), large cell numbers are usually required to generate a proper mesh for nasal cavity simulation. The time step should be very small to satisfy the stability criterion

for transient simulations (Courant number smaller than 1). This will increase the computational time and make the transient simulation for nasal airflow very computationally expensive.

From the above discussion, we could divide the nasal airflow simulation into three types regarding the inhaling flow rate profile versus time:

(a) a sinusoidal profile

(b) a constant profile with transient simulation

(c) a constant profile with steady-state simulation

The first type is more accurate, while the second and the third types involve more approximations for unsteadiness but are easier to approach.

To justify the usage of the approximations, we return to the main issue of this paragraph: how unsteady is the nasal airflow? To justify the selection of quasi-steady approximation from a sinusoidal profile, Doorly et al. (2008b) estimated Strouhal number $St$ and Womersley number $Wo$ under the restful breathing condition. We will discuss the physical meaning of these two non-dimensional numbers in section 3.2.2. Doorly et al. (2008b) recorded that $St$ and $Wo$ are respectively less than 0.25 and 3. Especially, the lower $St$ means that the inspiratory time is an order of magnitude higher than the duration for the airflow to pass through the nasal cavity. Therefore, Doorly et al. (2008b) stated that the quasi-steady assumption is valid for the restful inspiratory rate. However, there is still debate on the usage of steady-state assumptions. The prevalent idea is to apply a constant flow rate with the steady-state simulation for the entire inspiratory process (see the setup for Wen et al. (2008), Casey et al. (2017) and Taylor et al. (2010)) to reduce the computational time. In contrast, Doorly et al. (2008) experimentally demonstrated that, while the majority of the nasal airflow is quite steady, the fluctuating flow pattern is visible at the location when the flow interacts with the middle turbinate, even within the restful breathing range of flow rates. Their separate review paper (see Doorly et al. (2008b)) suggested that using unsteady simulation is recommended in the case of accumulative parameters such as coupled heat transfer, particle deposition, or odor transfer.

- **Flow Paradigm (Laminar or Turbulent):** Besides the unsteadiness, the flow paradigm is another critical issue in determining the solution method. The reason for discussing the flow paradigm is to choose the proper turbulent model. If the flow stays in the laminar regime, the flow field can be solved without turbulence modeling, which will be accurate and fast for calculation. The nasal airflow regime is strongly related to the Reynolds number, hence is associated with the flow rate and the geometry of the nasal airway. There is no strict criterion for a flow rate range within which the nasal airflow can be considered laminar because even in lower flow rates, the nasal airflow can be vortical, chaotic, and three-dimensional. Hahn et al. (1993) measured the velocity profile of the healthy unilateral nasal airflow at different locations using a hot-film anemometer. Under the unilateral flow rate of 10.8 L/min (almost the upper limit of the restful breathing condition), they recorded a predominantly laminar flow across the nasal cavity. The same conclusion was reached by Doorly et al. (2008a), using high-speed dye visualization, however, at a slightly lower unilateral flow rate of 10.2 L/min. These findings were well accepted as the justification for using the laminar model

under the restful breathing condition (see Wen et al. (2008) and Van Strien et al. (2021)). However, hardly any work mentions whether a laminar model is still valid for nasal airflow with nasal obstruction.

In the other situation where turbulence modeling is necessary, there are three approaches: Direct Numerical Simulation (DNS), Large Eddy Simulation (LES), and Reynolds-Averaged Navier-Stokes (RANS). DNS requires fine space and time resolution down to the Kolmogorov scale. Thus, it would be rather time-consuming to complete each simulation. For this reason, limited research simulates nasal airflow with DNS. One existing study is Li et al. (2017), which investigated the nasal airflow under various breathing conditions for a constant unilateral flow rate from 180 mL/s to 1100 mL/s using DNS. To sufficiently resolve the Kolmogorov scale, their mesh size for DNS simulation varies from 11.5 million at the lowest flow rate to 36.7 million at the highest flow rate. To simulate one second of breathing time, they reported that the required computational time varies from 1100 to 2100 hours using DNS on a workstation with 6 cores. Compared to DNS, LES could decrease the required computational time while still providing well-resolved but less accurate results, principally by solving eddies larger than the mesh size and modeling eddies smaller than the mesh size. However, LES could also require considerable computational resources in our nasal airway simulation. For example, to study water droplet deposition, Covello et al. (2018) reconstructed a patient-specific 3D model and set up an LES simulation with up to 25 million cells of the grid, tracking different sizes of water droplets with the Lagrangian approach. With the help of 32 to 96 processors in a supercomputer center, they recorded approximately 40000 CPU hours for 14 case studies, demonstrating the cost of LES simulation with a fine mesh.

The expensive time cost for DNS and LES makes the RANS method rather popular in simulating turbulence effects in nasal airflow. Compared to DNS or LES, a RANS simulation for nasal airflow research requires the calculation time of hours using a workstation with 8 cores. Under the RANS category, there are still many specific approaches to approximate the Reynolds stress. Notable research trying to find a suitable candidate for nasal airflow simulation is Li et al. (2017). They compared the results simulated by the “laminar” method (without any turbulence modeling), $k-\epsilon$ method, $k-\omega$ method, $k-\omega-SST$ method, Reynolds stress model (RSM) method, LES, and DNS with experimental data of the exact model. Three different flow rates are involved in their simulation, corresponding to restful breathing, medium sniffing, and strong sniffing conditions. The velocity profile and the turbulent intensity at specific locations obtained from different turbulence modeling methods are compared with the experiments. Although no turbulence model perfectly predicts the experimental data for all comparisons, DNS gives the most accurate result of all the selected methods compared with the experimental result, followed by LES. They suggested using the laminar model is considered sufficient for every selected output parameter under the restful inspiratory condition instead of using RANS models. Under sniffing conditions, the $k-\omega$ model of all the RANS models gives the best comparison with experimental data regarding the velocity profile. In contrast, the result with the $k-\epsilon$ model deviates from the experimental results the most. Regarding the turbulent intensity, their study shows that all the selected RANS models failed to predict turbulence intensity correctly. Although Li et al. (2017) did not explain that the $k-\omega$ model predicts

better than other RANS models, one could argue that the $k-\omega$ model behaves well in predicting adverse pressure gradient and the separating flow, which usually happens in the nasal airflow. In contrast, the $k-\epsilon$ model performs poorly under these circumstances. Finally, they stated that the $k-\omega$ model gives the best overall performance among the four RANS models in terms of accuracy and computational cost.

As one could already see from the analysis by Li et al. (2017), a question mark should be added regarding the accuracy of the RANS simulation. A golden criterion to check the accuracy of numerical simulation is always comparing numerical results and experiments. To this end, the most straightforward approach will be to compare the CFD simulation result with PIV in the flow field or dye visualization in the streamline pattern. Such comparison can be found in Doorly et al. (2008a) and Doorly et al. (2008). Although we also strongly recommend comparing PIV and CFD, a PIV setup could take months, which is not within the scope of this work. Apart from PIV, another possible approach is to compare the velocity profile at a specific cross-section using a hot-film anemometer or Pitot tube. However, these methods are invasive measurement techniques, which we reckon will also alter the nature of nasal airflow. Also, Li et al. (2017) mentioned that using the hot-film anemometer might not be able to resolve the sharp velocity gradient accurately near the wall.

One suitable experimental technique for this study is to measure the pressure drop of the nasal airway to validate the selection of the RANS model. A similar approach can be seen in Weinhold et al. (2004) and Wen et al. (2008). There are two reasons behind the overall pressure drop measurement.

The first reason is that the predicted pressure drop with the laminar model is smaller than with the turbulence model under the same flow rate caused by the additional viscous stress at the boundary in a turbulent flow.

The second reason is that the growth rate of pressure drop versus flow rates (the pressure-flow relationship) can also provide insights into the flow paradigm. In principle, when the viscous effect dominates the flow field under lower flow rates, pressure drop behaves linearly with flow velocity ($\Delta P \sim U$). In addition, when the inertia effect dominates the flow field under sufficiently high flow rates (higher than the restful breathing flow rate range), the pressure drop shows approximately quadratic behavior ($\Delta P \sim U^{1+x}$, $x \approx 1$). A similar pressure-flow relation in the nasal airflow was also recorded by literature. Zamankhan et al. (2006) stated that a linear pressure-flow relationship can be found at a flow rate smaller than 0.8 L/min, and Schreck et al. (1993) recorded that a quadratic pressure-flow relationship is expected for a flow rate larger than 30 L/min. However, no research has yet established a universal critical flow rate for nasal airflow in the viscous and inertial regime. The pressure-flow relation can be reflected in the turbulence model selection, as the laminar model can describe the viscous regime's flow field well. In contrast, modeling inertial behaviors under high flow rates, such as turbulent flow and separation, would be more difficult. Therefore, we believe that in addition to the pressure drop value, a good prediction in pressure-flow relation can also be used as a guide to reflect the flow paradigm.

One representative approach to measuring the pressure drop along the nasal airway is given by Van Strien et al. (2021). They designed many ports along

the nasal airway for pressure drop measurement (see figure 2.3). We still hold concerns about the influence on the flow field by the measurement port in this configuration. This is because The diameter of the pressure sensor port is similar to the width of the meatus in the turbinate region is within a length scale of millimeters. In contrast to the pressure measurement along the nasal airway, we can measure the pressure drop around the pharynx region. The diameter of the cross-section in the pharynx region is around ten times larger than the diameter of the nasal turbinate meatus. Therefore, the measurement of the overall pressure drop will barely cause any disturbance of the original nasal airflow.

Although the pressure drop measurement for healthy nasal airflow has been studied, we note that there is little literature recording the pressure drop for NAO patients.

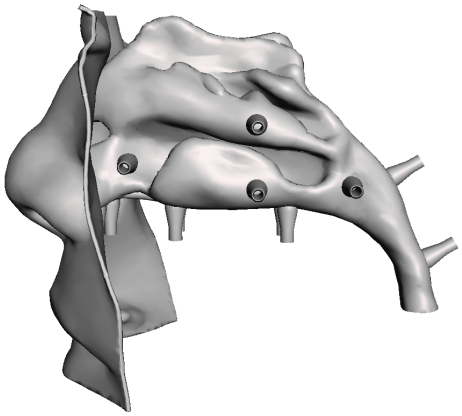

Figure 2.3: The experimental setup of Van Strien et al. (2021) is adapted in this figure. The small cylindrical extrusion represents the port for pressure drop measurement, which connects the pressure sensor with the nasal airway model. The pressure sensor port has a similar size compared to the meatus inside the model.

From the study, we might notice that although nasal airway simulation would be highly expensive in computational resources with an accurate DNS or LES study for multiple case studies with various flow rates, it is still within engineering approximation to resolve nasal airflow through RANS simulation under a higher respiratory flow rate. The experimental study to validate RANS simulations can also be done with a more straightforward and reasonable setup. This enables us to investigate nasal airflow in various flow rates for both healthy and NAO patients.

## 2.3. Correlating CFD variables with the sensation of patients

The expected scenario of the current research is to utilize a sound and robust CFD workflow as an alternative objective measurement tool for NAO detection. However, the question arises, which parameter should be compared from all the potential outcomes of each CFD simulation? To quantitatively answer this question, the primary methodology of existing research is to correlate each CFD variable with the subjective measurement score, which is the subject of this section. We will first review the current attempts for this correlation.

Currently, three types of CFD variables are often mentioned when correlating with

subjective scores: heat transfer variables (which were suggested to be correlated with the effect of thermo-receptor (TRPM8) by Zhao et al. (2011)), nasal resistance, and wall shear stress.

Kimbell et al. (2013) selected 10 patients undertaken nasal obstruction surgery and correlated various CFD parameters with the NOSE and VAS scores from both pre-surgery and post-surgery states. A summary of their finding can be seen in the first row of the table 2.1. Furthermore, Sullivan et al. (2014) found out the surface area where heat flux is larger than 50 $W/m^2$ is strongly correlated with the subjective scores and proposed this new criterion. Findings by both Kimbell et al. (2013) and Sullivan et al. (2014) suggested that the nasal obstruction might be a multifactor effect, combining the thermal and mechanical contributions.

| | Material | Variables with significant correlation | Variables with weak or no correlation |
|---|---|---|---|
| Kimbell et al. (2013) | 10 Subjects with Pre-surgery & Post-surgery<br>NOSE<br>VAS | **NOSE:**<br>Airflow-OS<br>Heat Flux-OS<br>Airflow Partition-OS<br>CFDNR Ratio-OS<br>**VAS:**<br>CFDNR Ratio-OS | Airflow-Bilateral<br>CFDNR-Bilateral<br>Heat Flux-Bilateral<br>Wall Shear-Bilateral<br>Airflow-US<br>CFDNR-US<br>Wall Shear-US<br>Heat Flux-US<br>CFDNR-OS<br>Wall Shear-OS |
| Sullivan et al. (2014) | 10 Subjects with Pre-surgery & Post-surgery<br>NOSE<br>VAS | **NOSE & VAS:**<br>Area where heat flux is larger than 50 $W/m^2$ | Peak Heat Flux ($W/m^2$) |
| Casey et al. (2017) | 15 healthy subjects & 15 NAO subjects<br>NOSE<br>VAS | **NOSE & VAS:**<br>Flow rate in middle meatus | Flow rate in inferior meatus<br>Flow rate in superior meatus |

Table 2.1: An overview of the findings by Kimbell et al. (2013), Sullivan et al. (2014) and Casey et al. (2017), in terms of the correlation between CFD variables and the subjective scores. In this table, the airflow rate under fixed pressure drop (Bilateral: Airflow-bilateral; Unilateral: Airflow-OS for Obstructive Side and Airflow-US for Unobstructive side), nasal resistance (Bilateral: CFDNR-bilateral; Unilateral: CFDNR-OS for obstructive side and CFDNR-US for non-obstructive side), and heat flux (Bilateral: Heat Flux-bilateral; Unilateral: Heat Flux-OS for obstructive side and Heat Flux-US for non-obstructive side) both unilateral and bilateral, as well as ratio of unilateral nasal resistance on the obstructive side to bilateral nasal resistance (CFDNR Ratio-OS) and the flow rate on the obstructive side to bilateral flow rate (Airflow Partition-OS). Kimbell et al. (2013) found that almost all the bilateral variables have weak or no correlation with subjective scores. In addition, the unilateral variables on the obstructive side, as well as the nasal resistance ratio correlate well with the subjective scores, which may indicate that these variables are suitable for NAO detection. Sullivan et al. (2014) and Casey et al. (2017) respectively proposed that the surface area where heat flux is larger than 50 $W/m^2$ and the flow rate in the middle meatus are correlated with the subjective scores.

In addition, Casey et al. (2017) correlated intranasal airflow distribution, meaning the proportion of airflow passing through the inferior meatus, middle meatus, and superior meatus, respectively, with both the VAS score and NOSE score. Their statistical analysis of 15 NAO patients and 15 healthy cases showed that subjective scores correlated better with middle airflow than another regional nasal airflow, and

concluded that reduction within middle meatus airflow correlates with obstruction sensation. From the distribution of heat flux, they also deduced that less mucosal cooling might correspond with complaints of nasal obstruction.

The selection of the CFD variables to correlate with subjective sensations is based on case studies of nasal obstruction subjects that report a significant change in certain variables. For example, the motivation for Kimbell et al. (2013) to select the nasal resistance is from Garcia et al. (2010), where they discussed the effect of anterior septal deviation causing the nasal resistance to increase. The motivation for selecting heat-transfer-related variables is from the medical study of Zhao et al. (2011), where they tested the subjective sensation of 44 healthy volunteers by measuring the VAS scale under different inhaling conditions (room air, dry air, and cool air), and found that air humidity and heat loss during inhaling is an important factor for correlation. Therefore, to find a potential criterion for CFD analysis to correlate with subjective measurement scores, we should first conduct a case study indicating the potential parameter, using the comparison between the healthy and the NAO patient.

As we have discussed, one potential type of CFD variable for correlation could be the thermal effect, which was mentioned by most of the relevant research. However, in view of the consistency with our experimental measurement of the pressure drop, we restrict our discussion to pressure-drop-related CFD variables for the NAO detection criterion.

## 2.4. Motivation and scope

From the above literature research, we can make the following observations.

On the one hand, the general procedure for using CFD to investigate nasal airflow has been clarified by previous research. However, justifications for several CFD settings are not yet clear, such as the inflow boundary configuration, the steady-state nasal airflow approximation, and the flow regime of the nasal airflow under restful breathing conditions for both healthy and NAO patients. On the other hand, concerning the application of CFD as a clinical measurement tool in NAO detection, the potential outcome of the CFD analysis is still under investigation.

From the findings above, we conclude that we need further assessment of several modeling assumptions for CFD simulations in the nasal airflow. With the validated CFD model, we will test a pressure-drop-related NAO detection criterion. Specifically, five objectives will be achieved in this thesis:

- To set up a reliable numerical workflow to model nasal airflow from given CT scans, including reconstruction, mesh generation, and numerical solver.
- To test the sensitivity of the established numerical setup concerning grid dependency and configuration of inflow profile (external face or plane-truncated inlet). The selection of convergence criteria will also be tested.
- To find the optimal turbulence model (or laminar model) with various flow rates under restful breathing conditions for both healthy and NAO patients by external validation using the pressure drop measurement.
- To investigate the validity of the steady-state assumptions by comparing the result with transient simulations.
- To propose a potential criterion of CFD outcome for the NAO detection.

# 3

# General modelling of the nasal airflow

In this chapter, technical details of our modeling approach will be introduced. As it is introduced in section 2.2, the general procedure to numerically study the nasal airflow of one single patient would be “reconstruction, mesh generation, CFD simulation and post-processing”. To better describe the technical details of each procedure, the structure of this chapter is organized as follows. In section 3.1 the focus will be on introducing the “reconstruction” procedure as it requires input from the medical expert. Section 3.2 will discuss “mesh generation” and “CFD simulation” procedures, as we will provide our approach to generating a proper mesh within such a complicated geometry, the evaluation of mesh quality, and the motivation for the selection of solving techniques.

## 3.1. Medical modelling

### 3.1.1. CT scan acquisition

In this study, two subjects with identified NAO symptoms (scan2 and scan2018) and two healthy subjects (FD2 and FD4) were selected as research subjects. In addition, in section 6.3, one subject without NAO, but was identified with nasal cycle and loss of smell, was also investigated. An introduction to the pathology of two obstructive cases is included in figure 3.1.

CT scan datasets were anonymized (meaning patients’ identity information was removed from CT scans) and collected from Erasmus University Medical Center, Rotterdam, the Netherlands. The usage of the aforementioned CT scan is approved by Erasmus MC. A detailed description of the CT scan dataset for each subject is concluded in Table 3.1.

One of the key quantities of CT scans worth mentioning is the slice thickness of CT scans. Slice thickness represents the sample rate in the scanning process when a CT scan is taken. A thinner slice thickness indicates a higher resolution in CT scanning. We also find that subjects with thinner slice thickness require less effort in the paranasal sinus removal process during reconstruction (see section 3.1.2). In comparison, thicker slices of the imaging will result in a blurrier boundary between the airway and the surrounding solid structures, which will increase the uncertainty of the reconstructed geometry. However, slice thickness cannot be reduced unlimitedly, because radiation exposure to the patient has to be increased when the slice thickness is reduced. Therefore, to optimize the outcome of CFD analysis on nasal airflow, it

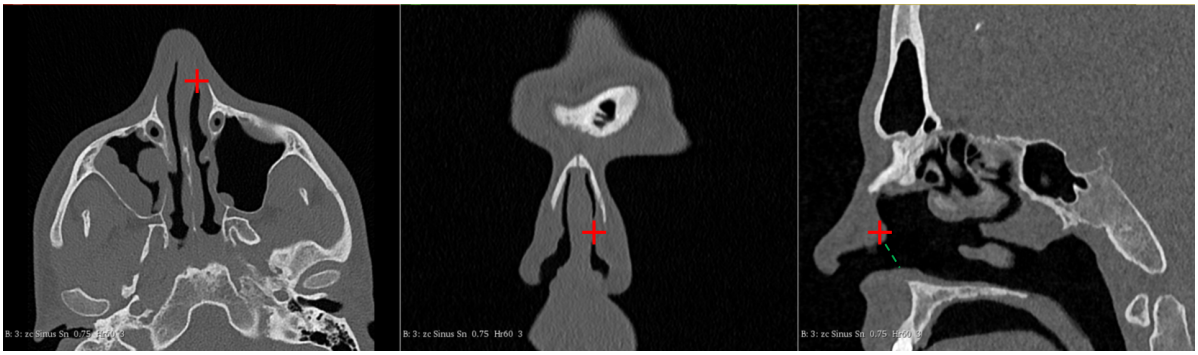

(a) A pathology slice of scan2 CT scan image

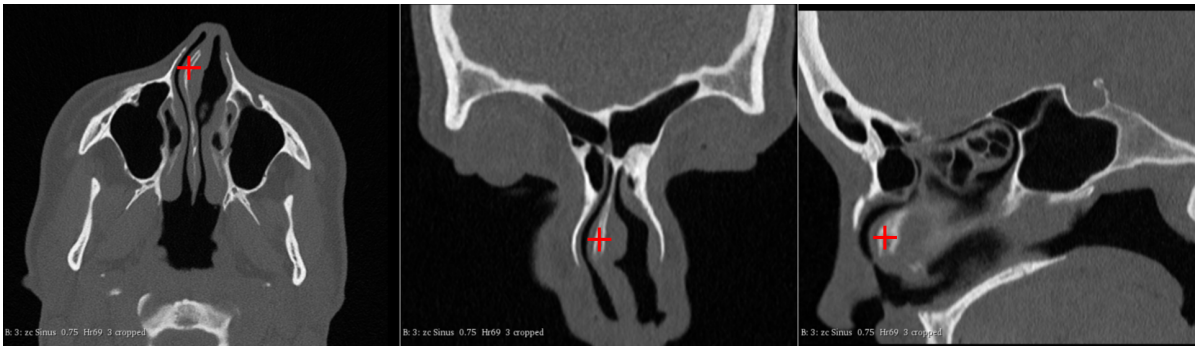

(b) A pathology slice of scan2018 CT scan image

Figure 3.1: A pathological demonstration of CT scans of two NAO subjects. The dysfunctional structure (solid structures, gray/white colored region in CT scans) is marked with red crosshairs. In the scan2 subject (see figure 3.1 (a)), the septal deviation (labeled red crosshair) happens at the internal nasal valve (the green dash line) of the left cavity, causing the airway (the dark region in CT scans) at the internal nasal valve to be suppressed. While in the scan2018 subject (see figure 3.1 (b)), the nasal airway of the right unilateral part is dysfunctional because the septal cartilage (labeled red crosshair) deviates to the right.

would be advisable to balance between a thicker slice thickness to ethically lower the radiation dose to the patient and a thinner slice thickness for a better segmentation process in the reconstruction procedure.

| Case Name | FD2 | FD4 | scan2 | scan2018 | FD6 |
|---|---|---|---|---|---|
| Pixel Spacing (mm) | $0.478 \times 0.478$ | $0.525 \times 0.525$ | $0.3 \times 0.3$ | $0.35 \times 0.35$ | $0.35 \times 0.35$ |
| Slice thickness (mm) | 1.0 | 1.0 | 0.75 | 0.75 | 0.75 |

Table 3.1: Data description of CT scan datasets in this study are shown. Both CT scans for NAO subjects and the CT scan for the nasal cycle subject have better resolution than the CT scan of healthy subjects, with smaller slice thickness and smaller pixel spacing.

An alternative to normal CT scans is cone beam CT (CBCT) scans, containing lower radiation doses and more clinical availability. In this study, we made a trial segmentation with cone beam CT scans. We report the potential for CBCT scans to be applied in CFD analysis in the future.

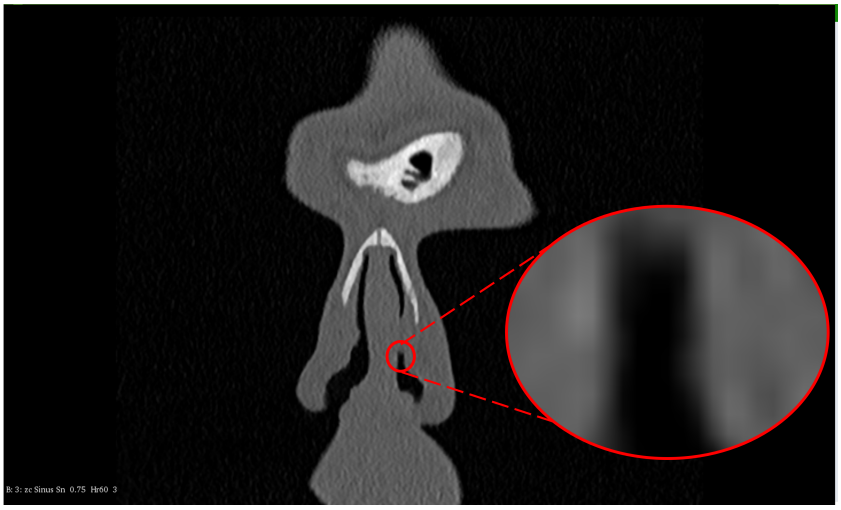

Figure 3.2: A slice of scan2 CT scan image along anterior-posterior direction (same location as figure 3.1 (a)). If we zoom in on the nasal airway boundary, the grayscale of the boundary is gradually changing. This is because the resolution of the CT scan imaging will never be accurate enough to determine the exact location of the boundary between air and its surrounding structures. Therefore, a range of grayscale is specified for the threshold filter to detect the airway boundary.

.

### 3.1.2. From CT scan to surface geometry: reconstruction procedure

After collecting CT scan datasets from so-called DICOM files, we used 3D Slicer (free, open-source software for medical image processing by Fedorov et al. (2012)) to obtain its 3D nasal airway geometry. The general procedure is as follows:

1. **Pre-processing:** For certain CT scans, noise is visible in the CT scan series. If no denoising operation is applied, the resulting geometry will be affected later in the segmentation procedure. Therefore, a denoising filter is applied before segmenting the CT scan.

2. **Filtering out solid structures from the nasal airway:** The main principle of separating the nasal airway from its surrounding solid structures is to utilize the grayscale difference between air and the solid nasal structures in a CT scan. The grayscale of a CT scan is quantified using the Hounsfield unit (HU). Briefly speaking, the Hounsfield unit measures how easily X-ray can penetrate the material. It regulates the grayscale of distilled water to be 0 HU and the grayscale of pure air to be -1024 HU. This fact results in a large grayscale for the dense materials in CT scans, such as bones or cartilage, and the smallest grayscale for air. The grayscale difference allows for filtering out the nasal airway from the surrounding solid structures with a threshold filter for grayscale. We note that the threshold filter here is defined as a grayscale range for two reasons. The first reason is that the solid structures surround the airway so that the grayscale will be higher than the pure air (-1024 HU). The second reason is that the nasal airway boundary gradually changes from large to small grayscale, as seen in figure 3.2.

   Now, one might wonder, to obtain the nasal airway, what will the grayscale range for the threshold filter be? The minimum grayscale value should be held as -1024 HU because our goal is to detect the airway, which has the lowest grayscale of all the structures in the CT image. Nevertheless, there is no fixed answer regarding

the selection of the maximum grayscale value because of the gradually changing grayscale of the nasal airway boundary.

Several existing studies have discussed the selection of the optimal maximum grayscale value for the threshold filter. On the one hand, Quadrio et al. (2016) conducted CFD simulations using 3D nasal airway geometries reconstructed from multiple grayscale ranges for the threshold filter, with the maximum grayscale value varying from -120 HU to -280 HU. To compare flow rate differences among all grayscale ranges, they maintained a prescribed pressure drop of 130 Pa throughout the nasal airway. A comparison of the flow rate of the simulation results from all threshold values shows that with a varying maximum threshold, the flow rate shows a minimal variation at a maximum grayscale value ranging from -220 HU to -240 HU.

On the other hand, Cherobin et al. (2018) investigated the impact of the threshold selection on numerical simulation. They selected three maximum grayscale values for the threshold filter: -300 HU, -550 HU, and -800 HU. The volume of the nasal airway resulting from the -550 HU maximum grayscale shows around a 20% difference compared to the resulting volume by the -300 HU grayscale. The same volume difference also appears comparing the -550 HU segmentation with the -800 HU segmentation. After simulating the nasal airflow of all the resulting 3D geometries numerically, they concluded that certain variables, such as pressure drop, flow rate, and cross-section area, strongly correlate with the threshold selection. However, other parameters, such as intranasal airflow distribution or surface area, are less sensitive to the maximum grayscale value.

Above all the arguments on the selection of threshold filter, there is one rule in choosing the grayscale range. For multiple cases in one study, the segmentation threshold should be kept constant to reduce the deviation of the simulation result among subjects caused by the variation of the threshold choice.

Considering all the above analyses on the threshold selection, the grayscale range for the threshold filter of this study is chosen as -1024 HU to -220 HU, within the optimal range of the grayscale value by Quadrio et al. (2016). It is found that a maximum grayscale value below -220 HU will result in nonphysical discontinuities in reconstructed nasal airways of certain subjects (see Figure 3.3 (c)) for the CT scans of this study. The discontinuities for those scans are presumably caused by the limitation of the CT imaging resolution at thin parts of nasal airways. At those particular thin structures, the grayscale of the nasal airway and its adjacent solid structures will be averaged, resulting in a higher grayscale at those locations. Therefore, we applied a threshold filter of -1024 HU to -220 HU for all the subjects in this study. However, a higher maximum grayscale might result in an increased cross-section area of the reconstructed nasal airway for each subject because fewer structures are filtered out of the computation.

To demonstrate the effect of the threshold filter of the proper grayscale range, we take a certain slice of the FD2 subject as an example and give a brief discussion in Figure 3.3.

3. **Obtaining the 3D nasal airway geometry:** As it is mentioned in 1.2.1, paranasal sinuses are also not included. After the threshold filter is applied, using “paint” and “level tracing” tools and the “grow from seeds” function in 3D Slicer, a 3D

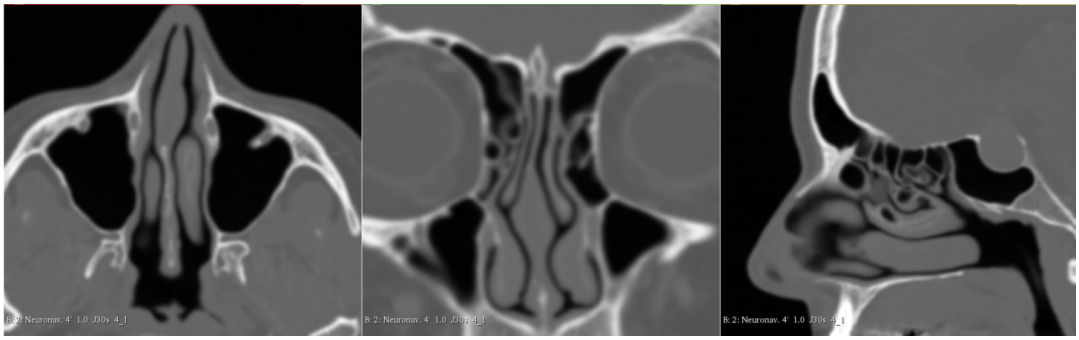

(a) One specific slice of FD2 subject before applying a threshold filter

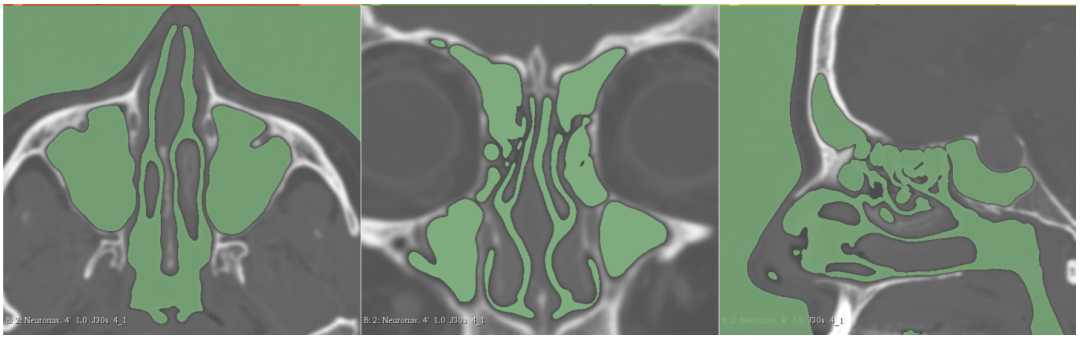

(b) One specific slice of FD2 subject after applying threshold filter of the grayscale ranging from -1024 HU to -220 HU

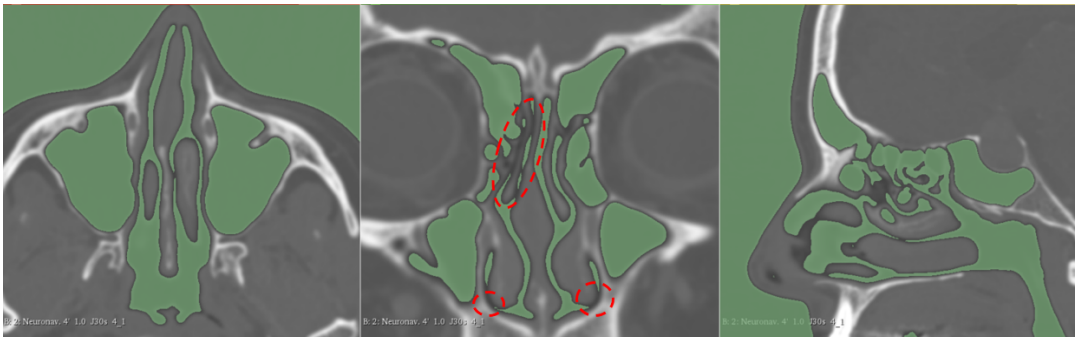

(c) One specific slice of FD2 subject after applying threshold filter of the grayscale ranging from -1024 HU to -300 HU

Figure 3.3: Different grayscale ranges are applied to demonstrate the effect of threshold filters. In figure 3.3 (a), the image contains both the nasal airway (structures shown in black), its surrounding bone structures, and (shown in white) surrounding soft structures (shown in gray). Then we applied a threshold filter (grayscale ranging from -1024 HU to -220 HU) to select the complete nasal airway (see the green color region in figure 3.3 (b)). In this way, the nasal airway will be selected as the volume of interest, and the rest will not be included in the further simulation. However, if a filter with a smaller range is applied (such as from -1024 HU to -300 HU, in figure 3.3 (c)), thin parts of the nasal airway (circled in red in figure 3.3 (c)) will also be filtered out, which is non-physical. Therefore, the threshold filter ranging from -1024 HU to -220 HU is selected in this study.

nasal airway geometry can be obtained. We note that the paranasal sinus removal process is the most time-consuming procedure of all the reconstruction procedures, as we have described that the middle and the superior meatus directly connect the sinuses.

4. **Post-processing:** The resulting 3D geometry from the previous step is reconstructed based on each pixel in the CT scans. Therefore, the surface of the nasal airway geometry is still artificially rough. An additional post-processing procedure is required for smoothing the geometry. To smooth the surface of the 3D geometry, we applied a shape-preserving smoothing filter using *MeshMixer* software (Autodesk, Inc., Mill Valley, CA, USA). Furthermore, the external nose or artificial sphere inlet boundaries (for section 4.3), as well as the artificial extension of the outlet for numerical stability purposes, will also be modeled in this procedure with the help of *MeshMixer*.

The resulting 3D geometry obtained after the above operations is stored in the form of Standard Triangle Language (STL file) and will be utilized for mesh generation.

## 3.2. Mathematical modelling

### 3.2.1. Introduction

This section will introduce the simulation setup using the nasal airway from section 3.1.2. Firstly, we will motivate our choice of the modeling setup (steady-state or unsteady, laminar or turbulence) using non-dimensional analysis. Furthermore, we briefly introduce the governing equations and boundary conditions corresponding to the modeling setup. Finally, the numerical schemes and solvers to solve the governing equations are introduced.

### 3.2.2. Non-dimensional numbers of the nasal airflow

One common distinction for the fluid flow paradigm is laminar/turbulent. From a simulation point of view, another consideration would be selecting a steady/unsteady solver. From the above analysis, the following non-dimensional numbers would be within our focus:

1. Reynolds number (*Re*): Reynolds number is one of the key non-dimensional numbers to reflect the laminar/turbulent flow regime. It can be written as:

$$Re = \frac{uL}{\nu} \tag{3.1}$$

where $u$ is characteristic velocity (m/s), $L$ is characteristic length (m) and $\nu$ is kinematic viscosity ($m^2/s$). Both the characteristic velocity (calculated from flow rate and cross-section area, $u = \frac{Q}{A}$), and the characteristic length (defined as the square root of the cross-section area, $l = \sqrt{A}$) are strongly location-dependent. However, for nasal airflow with such irregular geometries, it is difficult to define a universal area for the entire flow field. A typical *Re* defined at the internal nasal valve is maximally around 1500 for the healthy cases in the study. For the NAO cases under the same respiratory condition, calculated *Re* is around 2500. This result is nearly $Re_{d,crit} \approx 2300$, an accepted critical value for a round laminar pipe flow to transit into turbulence. In addition, for one specific healthy subject (FD2) with a narrow pharynx region, the local *Re* could even exceed 3000. Although

the nasal airflow is less uniform than a round pipe flow, these listed Reynolds numbers at a high inhaling flow rate might still be an alert for the onset of turbulence. The irregular geometry makes the flow field difficult to intuitively analyze if the large-scale turbulence happens. Therefore, it is reasonable to consider applying turbulence models to nasal airflow simulation in this study, especially for high respiratory rates.

2. Strouhal number (*St*): In the nasal airflow, $St$ can also be defined in multiple locations. Large-scale unsteadiness represents the mean flow passing through the nasal airflow. Small-scale unsteadiness, such as separation or the onset of turbulence, usually happens when the flow reaches sudden expansion. However, this study will focus on large-scale unsteadiness for two reasons. The first reason is that experiment from Doorly et al. (2008b) reveals that most of the flow field stays laminar and steady under a flow rate equivalent to 24 L/min, so the local unsteadiness has a limited effect on the mean flow behavior. The second reason is that sudden expansions, which induce small-scale unsteadiness, appear throughout the nasal airway. The location of sudden expansions strongly varies individually. In comparison, since the length scale and the flow speed of the nasal airflow are similar among people, the discussion of mean flow unsteadiness could be extended to other individuals.

   Therefore, we define the Strouhal number as

$$St = \frac{2\pi f L}{U} \tag{3.2}$$

   Here, $St$ represents the timescale for each breathing cycle in comparison with the time for the mean airflow to pass through the nasal airway, similar to the approach in Doorly et al. (2008b). Here, $f$ is the frequency of breathing cycles, $U$ is the mean flow velocity, and $L$ is the length of the nasal airway. Although the factor $2\pi$ is not explained by Doorly et al. (2008b), it can be argued that this factor comes from the time derivative of sinusoidal velocity in time ($\frac{\partial U}{\partial t}$, where $U = Usin(2\pi f t)$). It reflects whether the oscillation will dominate in the flow field at a high Strouhal number or the flow field will be developed all over the breathing cycle at a low Strouhal number. Because the airflow is mainly in the posterior direction during inhaling, the characteristic length $L$ is defined as the length scale of the nasal airway. The characteristic velocity is defined in the same fashion as the way in defining *Re*.

   $St$ in this study is calculated as follows. Currently, there is some disagreement in the reported breathing frequency for healthy people, as stated by McGee (2012), presumably because people tend to change their natural breathing frequency once they pay attention. The breathing frequency in this study is selected as 7.5 breaths per minute, close to the reported range in Hadjiliadis et al. (2021). We should note that this breathing frequency will be lower than the existing literature based on Rennie et al., 2011. From the definition of $St$, a lower flow rate will lead to the flow being influenced more by the pulsation effect, as the bulk flow takes longer to reach the outlet. The calculated *St* is approximately 0.09 for 10 L/min, and 0.036 for 24 L/min. Because $St$ is always smaller than 1 for the studied flow rates, a constant nasal airflow can be applied to approximate a time-varying flow rate profile in time, and the pulsation flow nature will not cause major oscillation

in the mean flow. However, as the cross-section area of the nasal airway is highly varying, using $St$ defined at the internal nasal valve may not be representative of the steadiness of the entire flow field. Therefore, we will also discuss the validity of steady-state simulation in section 5.2.

3. Womersley number (*Wo*): The Womersley number represents the balance between unsteady force and viscous force. $Wo$ is defined as

$$Wo = d\left(\frac{f}{\nu}\right)^{\frac{1}{2}} \tag{3.3}$$

Note that different from the definition of the length scale in $St$, the length scale $d$ here corresponds to the viscous force. Intuitively, this length scale should be half the width of a certain cross-section. Because we deem that the viscous force predominates at the internal nasal valve where the flow rate is at its peak, the length scale $d$ here is half of the internal nasal valve width ($4 \times 10^{-3}$ m). This definition corresponds to Doorly et al. (2008b). The calculated $Wo$ for the selected subject (healthy, FD2) is around 0.92, meaning that unsteady and viscous forces are balanced locally. This also contributes to the approximation to use a constant flow rate for nasal airflow.

With the above analysis, we could assume the nasal airflow in our study to be laminar and steady. We will attempt to justify these two assumptions respectively in section 5.1 and 5.2.

### 3.2.3. Mesh generation

For such a complicated geometry as the nasal airway, mesh generation generally requires more effort. This study will use unstructured mesh, as introduced in 2.2.2. To generate a proper mesh for our geometry, the resulting STL files for each study case from section 3.1.2 are imported into the commercial mesh generation software *CFMESH+* (version 1.1, by *Creative Fields*). By applying the Octree method to the input geometry, *CFMESH+* will generate base cells with large cell sizes and then refine the cells within the boundary of the input geometry. Finally, boundary layer cells will be generated. The resulting mesh will be an unstructured mesh with a hexahedral core and prism layers. Another open-source library implemented in OpenFOAM, *snappyHexMesh*, was also tested. To generate a proper mesh with good quality, parameters in both mesh-generating libraries require many adjustments and tuning. Compared to *CFMESH+*, it was found that boundary layer cells were not properly generated in the resulting mesh of *snappyHexMesh*. However, we note that *CFMESH+* also has disadvantages, that mesh in thin structures cannot be properly generated if the base cell size is large. Additional notes will be given in Appendix C.

After the mesh is generated from *CFMESH+*, an additional step is to tune the $y^+$ value. In section 5.1, turbulence models are used. To avoid the usage of wall models in turbulence modeling, $y^+ \sim 1$ should hold to resolve the sharp velocity gradient at the wall. This is achieved iteratively by an initial simulation with a coarse mesh and then computing the $y^+$ value. If the obtained $y^+$ is larger than the scale of 1 globally, the boundary layer cells are refined until $y^+$ is within such scale.

Finally, the computational mesh is ready for simulation. To evaluate the computational mesh quality, several mesh metrics, including aspect ratio, skewness, and non-

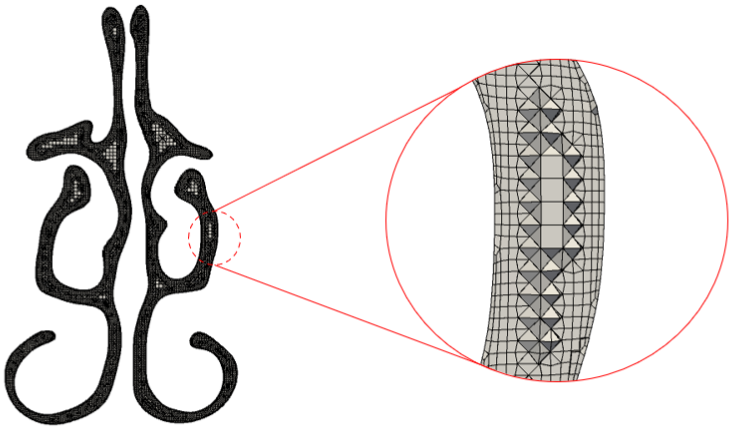

Figure 3.4: The configuration of the computational mesh is observed by slicing at one position. The near wall region is refined until $y^+ \sim 1$, while the inner region is resolved using hex-dominant cells with larger cell sizes. The computational mesh preserves the shape of both the thin structures in the inferior meatus and the thick structures in the middle meatus.

orthogonality, are given by a dictionary implemented in the OpenFOAM utility named *checkMesh*. The resulting mesh for each subject was evaluated through this utility. The reason is that high skewness and high non-orthogonality will increase artificial numerical diffusion. The *checkMesh* utility specifies a default recommended range for these metrics and therefore is considered a test standard for mesh quality.

On a final note for the computational mesh, the computational mesh in this study contains from 5 million to 9 million cells, varying with the internal volume of the patient-specific nasal airway, with hexahedron-dominant internal cells. Figure 3.4 shows a cross-section slice of the computational mesh.

### 3.2.4. Governing equations

Following the assumptions from Section 3.2, the governing equations contain both mass and momentum conservation for incompressible flow. Here, we write the discrete form of the governing equations in index notation (see also Nieuwstadt et al. (2016)). Mass conservation for incompressible flow is written as:

$$\frac{\partial u_i}{\partial x_i} = 0 \tag{3.4}$$

Momentum conservation for incompressible flow is written as

$$\frac{\partial u_i}{\partial t} + u_j \frac{\partial u_i}{\partial x_j} = -\frac{1}{\rho}\frac{\partial p}{\partial x_i} + \nu \frac{\partial}{\partial x_j}\left(\frac{\partial u_i}{\partial x_j}\right) \tag{3.5}$$

It should be noted that here $i = 1, 2, 3$ represents three directions (x, y, z) in Cartesian coordinates respectively. The unknowns in those above equations are velocity components in three directions $u_i$ and pressure $p$. Material constants in the equation 3.5 are density $\rho$ and kinematic viscosity $\nu$. Also in the equation 3.5, the gravity

term $g_i$ was already crossed out because it is considered that the gravity effect is not important in nasal airflow.

Considering the potential turbulence effect from the discussion in section 3.2.2, we apply turbulence modeling in simulations for section 5.1. In this case, there will be additional governing equations to be solved. The introduction of the turbulence model can be found in Nieuwstadt et al. (2016). In a nutshell, the so-called Reynolds stress, an additional term in turbulence modeling, is derived from the manipulation of the governing equation 3.5 and cannot be solved directly. For this closure, different turbulence models are introduced. A brief introduction to different turbulence modeling can also be found in section 2.2.3, which motivated us to use RANS models in this study.

Under the category of RANS modeling, there are still many options. In this study, we will apply the $k-\omega$ and $k-\omega-SST$ models for validation. In the nasal airflow, recirculation is prevalent in the olfactory region of the nasal airflow, as stated by Wen et al. (2008). Therefore, the $k-\epsilon$ group is not selected as a candidate because it behaves poorly in the flow with recirculation and a strong adverse pressure gradient. Although technically $k-\omega-SST$ is categorized as one variant of the $k-\epsilon$ group, it blends $k-\epsilon$ outside the boundary layer and $k-\omega$ within the boundary layer and is deemed to predict better than pure $k-\epsilon$ model in recirculation cases. Other than using eddy viscosity models, another possible approach is to use Reynolds stress models (RSM). However, given the fact that RSM models require more equations to be solved than RANS models, the convergence might be slow or even unstable and thus was not studied in this work.

Since it is not the intention of the study to introduce the RANS equations in detail, the specific governing equations will be given in Appendix B.

### 3.2.5. Boundary conditions

To solve the governing equations 3.4 and 3.5, boundary conditions are necessary. To better model nasal airflow, we could divide the entire computational domain into several regions, namely “inlet”, “outlet”, and “wall”. To better visualize the setup, we show an example of the boundary configuration with the external nose (which will be introduced in detail in chapter 4.3) and show the setup in figure 3.5. Since this study intends to simulate the inhaling process, the “inlet” will be the inflow region entering the nostrils. “Outlet” will be the outflow region leaving the pharynx. “Wall” will be the boundary of the nasal airway, representing the contact surface between nasal airflow and the surrounding solid structures. Then the prescribed boundary conditions can be summarized as follows:

1. inlet. The static pressure at infinity could be considered as the ambient pressure and the dynamic pressure at infinity could be approximated as 0, since the velocity at infinity is almost zero. For an incompressible solver, the pressure is only a reference value, while the pressure gradient is actually solved in equation 3.5. Therefore, we could choose the ambient pressure as zero, then the total pressure at infinity is zero as well. If Bernoulli’s principle is applied from the infinity to the inlet position, then the total pressure at the inlet would be the same as the total pressure at the infinity, which is also a constant value (ambient pressure). Therefore, the constant total pressure is prescribed at the inlet. Since we specified total pressure here, we prescribed *pressureInletOutletVelocity* boundary condition to solve velocities. This combination, generally to solve similar entrainment flows as

the nasal airflow, will increase the numerical stability, as suggested by Weller et al. (1998). For turbulence modeling, boundary condition at the inlet is discussed in Appendix B.

2. outlet: The boundary condition for the pressure at the outlet is prescribed as a zero-gradient boundary condition. For the velocity, the velocity direction is assumed as normal to the outlet boundary. The velocity magnitude is uniform, and calculated from the specified flow rate. To reduce any artificial effect near the outlet boundary, the computational domain is artificially extended to a certain length. During the procedure of analyzing the flow field, such an extension is removed. Such operation is also mentioned by Van Strien et al. (2021). For turbulence modeling, we prescribe a zero-gradient boundary condition at the outlet.

3. wall: A zero gradient boundary condition for pressure is applied at the wall, and a no-slip boundary condition is assumed for solving the velocity. The wall is assumed to be smooth for the convenience of modeling. This might not be the case in practice because there will be mucus and nose hair at the nasal cavity wall. However, it is beyond the scope of this study to include the mucus layer in our simulation. For turbulent quantities, we use wall functions near the wall for preliminary calculations before the $y^+$ value is reduced to the order of 1. For final simulations where the boundary cells are fully refined, the wall functions for all turbulent quantities, except for $\omega$, are not included in the solving procedure. Because the $\omega$ value is theoretically infinite near the wall, the wall function for the $\omega$ variable is always applied.

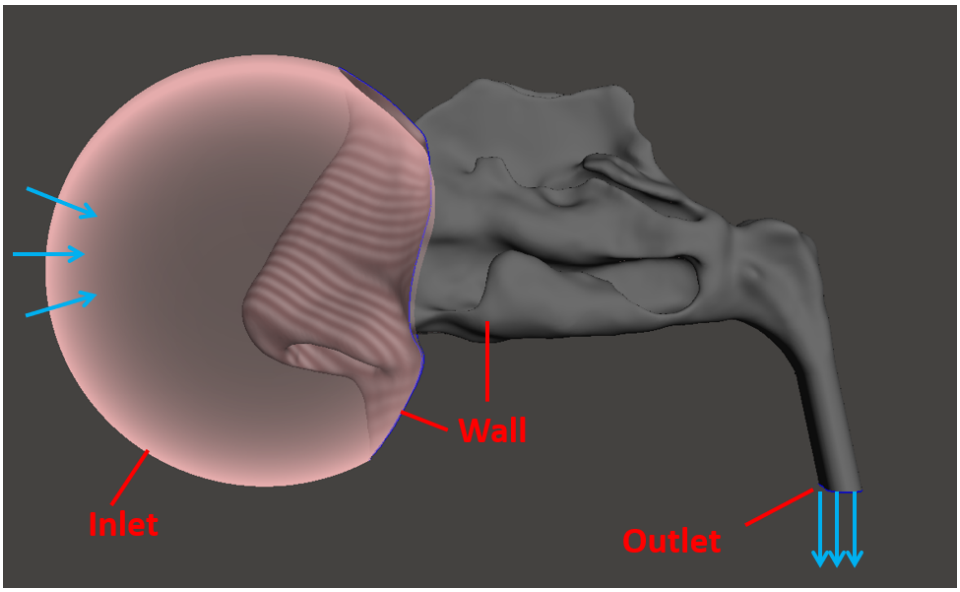


Figure 3.5: An overview of boundary condition settings for the configuration with the external nose is shown in figure 3.5. The inlet patch is prescribed at the artificial surface upstream to the nostril (or directly at the nostril for a plane inlet case in chapter 4). The “wall” region includes the nasal airway boundary and the external nose if it exists in the model. The “outlet” region is defined at the end of the calculation domain.

### 3.2.6. Numerical schemes and solvers

After defining the boundary conditions, the nasal airflow can be solved with our computational mesh by numerically solving the governing equations. In this study, simulations are conducted through OpenFOAM (version 6, by Weller et al. (1998)), a finite volume method (FVM) based software. The workflow for such software is as follows: The first step is to convert each term in the governing equations into discrete form, which requires the definition of numerical schemes. The second step is to solve the discretized equations to obtain the value of the unknowns. Correct implementation of the numerical solver is required in this step. Also, since our mesh has a non-orthogonality of around 65 degrees, it might require special correction for non-orthogonality, which will also be treated in this step.

1. Numerical Schemes: For steady-state simulations, the time-dependent term is not included in the simulation. We apply the linear upwind scheme for spatial discretization. Another potential candidate for spatial discretization here is the central difference scheme. However, the problem with the central difference scheme is that it creates nonphysical solutions near the outlet patch where the gradient of the flow is large. This is presumably caused by its dispersive nature near the jump for a large Peclet number, while the diffusive feature of the linear upwind scheme will smooth out to such a large gradient. Also, in this study, it was later found that the selection of the linear upwind or the central difference scheme will not show a significant difference (around 0.5%) in the static pressure drop. It is worth consulting the book Versteeg et al. (2007) for comparing the central difference scheme and the linear upwind scheme. For non-orthogonality treatment, we apply *cellMDlimited* function for Gauss linear gradient discretization to prevent overshooting in gradient caused by the non-orthogonal mesh. Also, surface normal is approximated with an additional correction to correct the misalignment between the face-normal direction and the corresponding cell centers, caused by non-orthogonality.

   Other discretization schemes, such as the QUICK scheme and total variation diminishing (TVD) van Leer scheme, were also tested. It was found that linear upwind was the most stable scheme of all the tested schemes.

   For transient simulation, the time-dependent term is discretized using a backward scheme, and the spatial discretization is done by using a linear upwind scheme. The central difference scheme is also tried out, however, we note that the simulation diverged, potentially caused by the mesh. Due to time limitations, we decided to use a linear upwind scheme instead, because of the stability caused by its diffusive feature. However, we should note that combining a backward scheme and a linear upwind scheme could be less accurate than the central difference scheme.

2. As for the setup of the solver, the governing equations are solved iteratively by *simpleFOAM* solver using Semi-Implicit Method for Pressure Linked Equations (the SIMPLE algorithm). During each iteration, pressure is solved with the GAMG solver, while other variables are solved with the Gauss-Seidel solver. An additional non-orthogonal corrector is also implemented in each iteration. The scaled residual is selected as $1 \times 10^{-8}$ to ensure the variables are completely solved in each iteration. Meanwhile, the convergence value is required to determine that the simulation reaches the steady state. However, there is no absolute formula

to calculate the choice of convergence value. In this study, unless specifically mentioned, the convergence criterion is selected as $1 \times 10^{-4}$, considering the heavy computational time if such value is too high and the accuracy of the computational result if such value is too low. We will give the justification for selecting such convergence in section 4.2.

Because it is only within the scope of the thesis to justify the selection of numerical setups, it did not cover all the basic knowledge of numerics. For further information on the principle of numerical methods, it is advisable to consult Versteeg et al. (2007).

## 3.3. Time required for each simulation

For future reference, reporting the required time to simulate each case from a given CT scan is advisable. To this end, we recorded the computational time for one subject in this study. Considering that the cluster system used in this study is not easily accessible for medical researchers, we approximated the equivalent computational time when an 8-core workstation with Intel i7 processors is used.

CFD simulation in the nasal airflow generally contains four steps: reconstruction, mesh generation, CFD simulation, and post-processing. For each step, the required time can be found in table 3.2.

| | 1. Reconstruction | 2. Mesh generation | 3. CFD simulation | 4. Post-processing |
|---|---|---|---|---|
| Time cost | 3-5 hours | 0.5-2 hours | 4-6 hours per simulation (on an 8-core workstation) | Pressure drop: 0.5 hours (depending on the variable) |

Table 3.2: Time required to set up a CFD simulation for the nasal airflow, counting from obtaining a new CT scan dataset to completing post-processing.

# 4

# Verification of numerical setup

## 4.1. Introduction

In chapter 3, we have established a numerical setup to simulate nasal airflow with CFD. In this chapter, we will test out the sensitivity of the numerical setup from three aspects: convergence criteria, inflow boundary configuration, and grid dependency. Since it is too time demanding to verify the selection of the parameters in all the subjects, we select the FD2 subject in this study, which is deemed as one clinically representative subject by our ENT surgeon, with symmetrical anatomy on both sides of the nasal airway.

## 4.2. Convergence study

The selection of the convergence criterion (or convergence criteria since we are solving for multiple variables) is a balance between computing resources and the required accuracy, and thereby could be considered an important parameter in the simulation. However, in the previous study, CFD research on nasal airflow rarely justifies or even mentions the selection of convergence criteria. Of all the literature research in this study, there is only one specific research by Zhang et al. (2011) that briefly mentioned changing convergence criteria to a value smaller than $1 \times 10^{-4}$ will not have a considerable impact on the flow field. However, their geometry is a simplified oral airway model, a considerably less complicated geometry than the human nasal airway. This fact motivates us to conduct a convergence study, to find the optimal convergence criteria.

### 4.2.1. Material and approach

In this study, we used the GAMG solver and SIMPLE algorithm in OpenFOAM to solve the nasal airflow. In OpenFOAM, the scaled residual is computed for each iteration in the SIMPLE algorithm, and compared with the convergence criteria. The steady-state simulation stops when the scaled residual is smaller than the convergence criteria.

Since the convergence is more difficult for flow with large *Re* than with small *Re*, we select 24L/min as the flow rate condition (the largest flow rate under the restful breathing range) for the convergence study. Considering the further application of the turbulence model, in the convergence study, we will use the turbulence model ($k-\omega$) instead of the laminar model. This is because using the turbulence model will require more equations to solve than the laminar model, where more equations usually mean

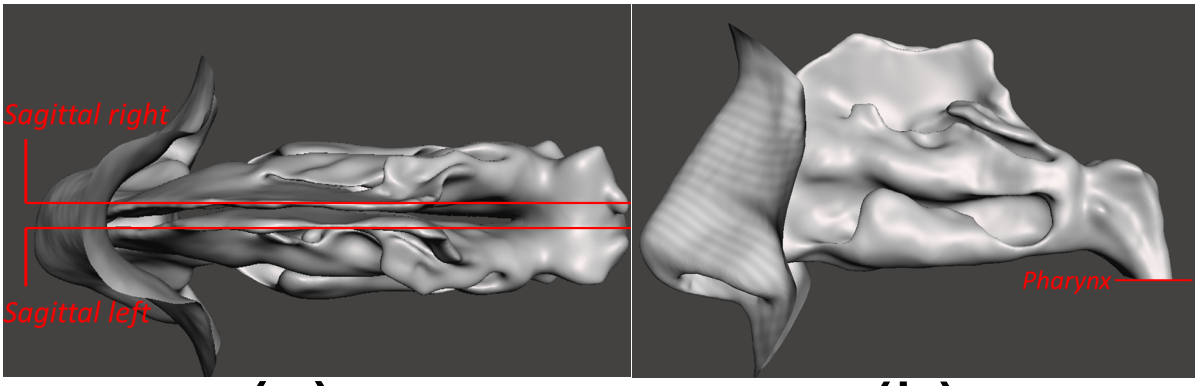


(a) (b)

Figure 4.1: The location of sagittal measurement planes is shown in figure 4.1 (a), and the location of sagittal measurement plane is shown in figure 4.1 (b). The pharynx plane is used for calculating the static pressure drop, while the sagittal planes are used for visualizing the pressure contour.

a slower convergence rate.

The convergence criteria are selected to be $1 \times 10^{-4}$ for all variables in this thesis. We will compare the simulation results under the convergence criteria of $1 \times 10^{-3}$, $1 \times 10^{-4}$, and $1 \times 10^{-5}$ and check if our selection of convergence study is reasonable. Since this study primarily focuses on the pressure field, we will select two relevant metrics for comparison. Firstly, we will look at the static pressure drop under those convergence criteria. The static pressure drop here is calculated from the difference between the ambient pressure at the infinity (defined as zero, from section 3.2.5) and the exit pressure at the pharynx plane (shown in figure 4.1 (a)). The static pressure drop will also be frequently mentioned in later sections. It is calculated from the pressure averaged over the cross-section area of the pharynx plane (the so-called area-averaged pressure) instead of measuring the pressure drop at a certain point of the outlet plane, such that the uncertainty will be reduced. A similar approach can be found in Wen et al. (2008). Furthermore, we will compare the pressure field of two sagittal cross-sectional planes under various convergence criteria. The viewpoint is shown in figure 4.1. Our choice for an optimal convergence criterion will combine the agreement of the metrics and the computational time under different convergence criteria.

### 4.2.2. Comparison of the static pressure drop

The computed static pressure drop is shown in the table 4.1. Changing the convergence criteria will not significantly affect the static pressure drop, as changing the convergence criteria from $1 \times 10^{-3}$ to $1 \times 10^{-4}$ will only cause the pressure drop to vary by $0.34\%$, and even negligible effect on the static pressure drop by changing the criteria further to $1 \times 10^{-5}$. Therefore, the effect of convergence error can be neglected when analyzing the static pressure drop in later sections.

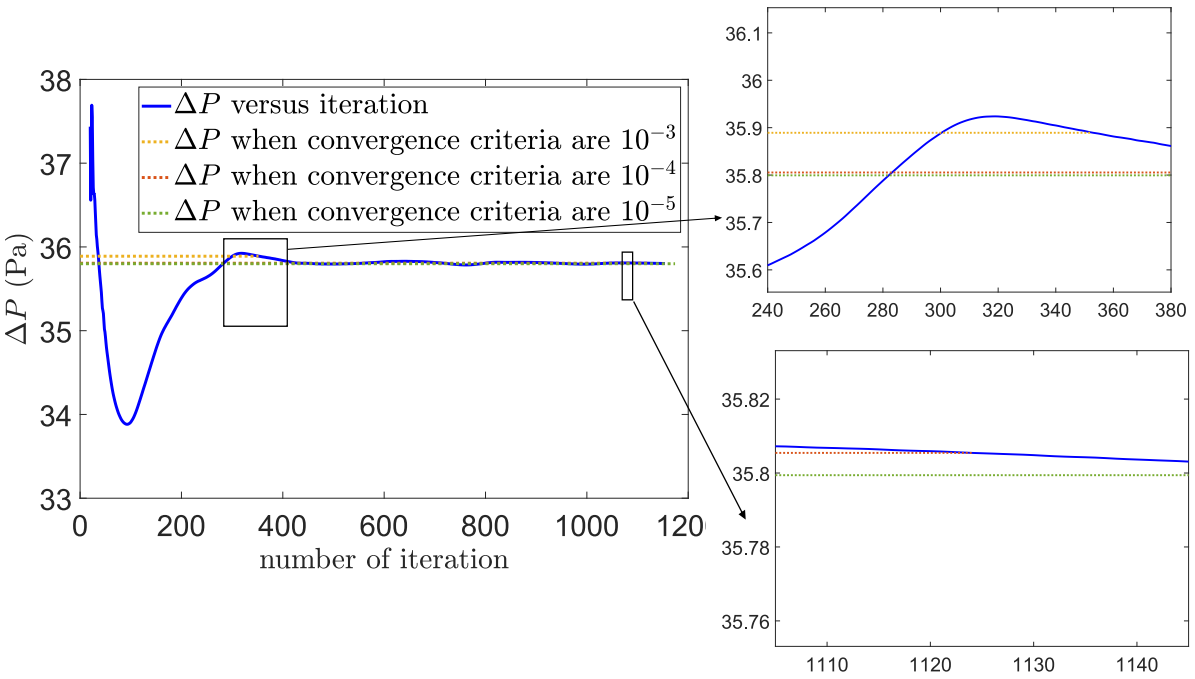


Figure 4.2: The static pressure drop ($\Delta p$) versus the number of iterations is plotted, with pressure drop values under three criteria marked. For visualization purposes, we will not show the entire pressure drop-iteration curve until the iteration under $10^{-4}$ convergence criteria but will show the pressure drop value. A special zoom-in for the comparison between the static pressure drop value under $10^{-3}$ and $10^{-4}$ is located in the right-top corner; under $10^{-4}$ and $10^{-5}$ are located in the right-bottom corner. We note that there is a numerically oscillating pressure drop value at the beginning of the simulation when the flow field is not fully converged. However, iterations for all three convergence criteria have passed the oscillating zone, which proved that the flow field already starts to converge at convergence criteria of $1 \times 10^3$.

| Convergence criteria | $1 \times 10^{-3}$ | $1 \times 10^{-4}$ | $1 \times 10^{-5}$ |
|---|---|---|---|
| Pressure drop (Pa) | 35.5987 | 35.4705 | 35.4695 |

Table 4.1: Static pressure drop values under various convergence criteria are compared. The resulting pressure drop shows a limited difference for the studied three types of convergence criteria.

Furthermore, we could plot the static pressure drop with the number of iterations in figure 4.2, which can indicate whether the flow field is sufficiently converging.

### 4.2.3. Comparison of pressure contour at the sagittal plane

The differences in pressure fields under different convergence criteria are obtained through the *Programmable Filter* in Paraview software (version 5.9.1, by Sandia National Laboratories & Kitware Inc) by subtracting the pressure field of different simulations at the same point and then taking the absolute value. In figure 4.3, we show the comparison for the left cavity, while in figure 4.4, the comparison for the right cavity is shown.

Overall, from the figures 4.3 (d) & (e) and 4.4 (d) & (e), we could see that the result of convergence criteria at $1 \times 10^{-3}$ already gives good agreement except for certain regions. At convergence criteria of $1 \times 10^{-4}$, the difference in pressure field is minimal compared with a convergence rate of $1 \times 10^{-5}$. This means that the flow field

for $1 \times 10^{-4}$ convergence criteria is better converged than the flow field for $1 \times 10^{-3}$ convergence criteria.

### 4.2.4. Computational time

We record that it requires around half an hour for each simulation of $1 \times 10^{-3}$ convergence to complete in a 28-core Linux Cluster system, compared with the computational time of around 2 hours for a $1 \times 10^{-4}$ convergence simulation. It requires more than 10 hours to reach convergence criteria of $1 \times 10^{-5}$.

### 4.2.5. Discussion

The convergence criteria selection depends on the required accuracy and computational resources. On the one hand, from the accuracy point of view, as can be seen in figure 4.3 (a), figure 4.3 (b), and figure 4.3 (d), changing the convergence criteria from $1 \times 10^{-3}$ to $1 \times 10^{-4}$ has an impact on the pressure field of up to around 0.7 Pa, accounting for around $2\%$ of the local pressure value. Moreover, changing the convergence criteria from $1 \times 10^{-4}$ to $1 \times 10^{-5}$ has an impact on the pressure field of up to around 0.05 Pa, accounting for around $0.13\%$ of the local pressure value. Applying convergence criteria of $1 \times 10^{-5}$ results in the most accurate pressure field of all the tested three criteria. On the other hand, considering the required computational time, both $1 \times 10^{-3}$ and $1 \times 10^{-4}$ convergence criteria require an adequate time for the computation to complete. However, convergence criteria of $1 \times 10^{-5}$ are considered too expensive in computational cost. Combining both aspects of the accuracy and computational resources, we will select the convergence criteria of $1 \times 10^{-4}$. However, in clinical applications where computational resources are limited, it might be advisable to increase the convergence criteria to $1 \times 10^{-3}$ for a faster simulation with acceptable accuracy on the pressure field prediction.

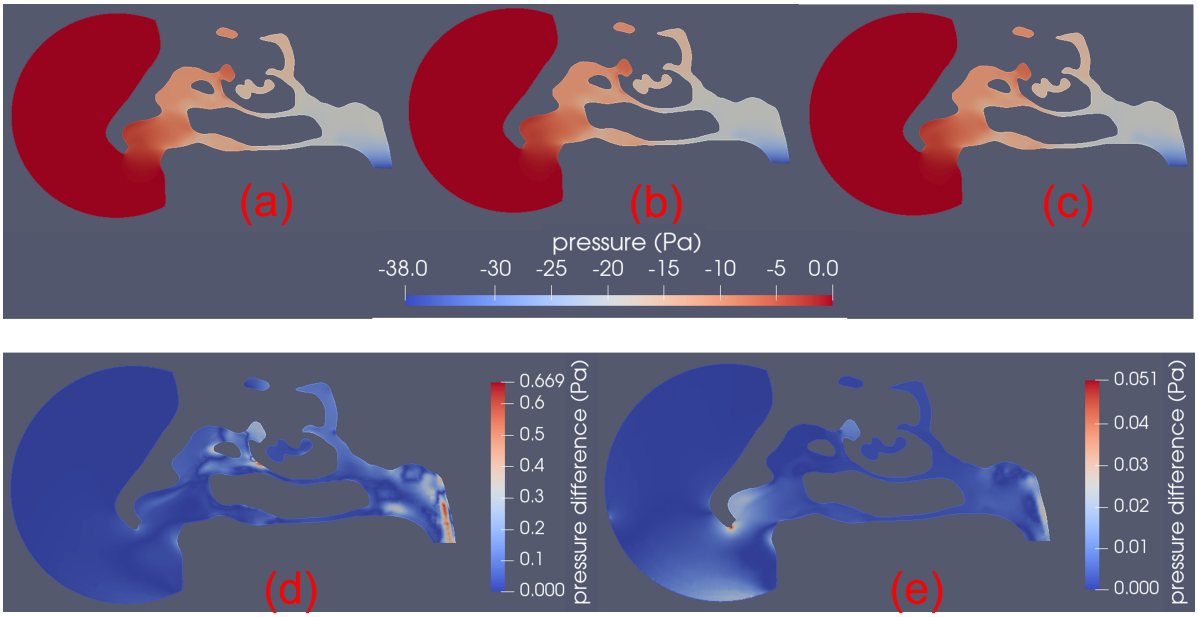


Figure 4.3: Pressure field difference of the left nasal airway among various convergence criteria. (d): pressure field difference between $1 \times 10^{-3}$ (figure 4.3(a)) and $1 \times 10^{-4}$ (figure 4.3 (b)); (e): pressure field difference between $1 \times 10^{-4}$ and $1 \times 10^{-5}$ (figure 4.3 (c)). The description is in the next figure.

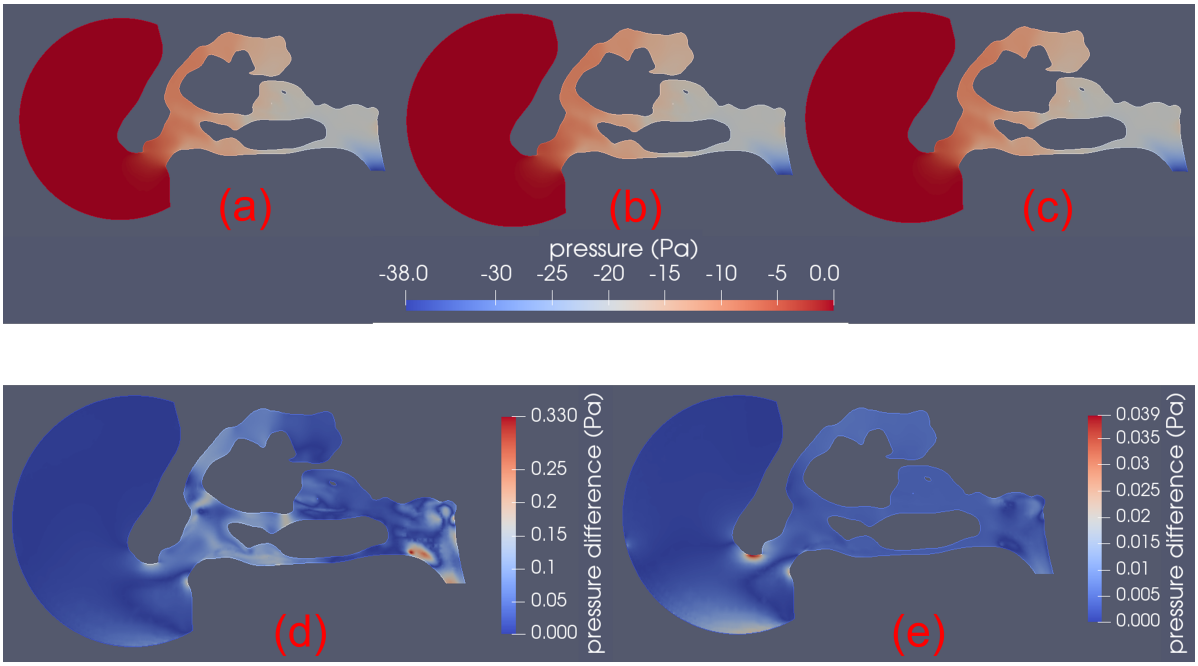


Figure 4.4: Pressure field difference of the right nasal airway among various convergence criteria. (d): pressure field difference between $1 \times 10^{-3}$ (figure 4.4(a)) and $1 \times 10^{-4}$ (figure 4.4 (b)); (e): pressure field difference between $1 \times 10^{-4}$ and $1 \times 10^{-5}$ (figure 4.4 (c)). Both figure 4.3 and 4.4 show that globally the pressure field difference at the criteria between $1 \times 10^{-3}$ and $1 \times 10^{-4}$ is smaller than 1% of the static pressure drop. The pressure field difference between $1 \times 10^{-4}$ and $1 \times 10^{-5}$ convergence criteria is approximately ten times less than that between $1 \times 10^{-3}$ and $1 \times 10^{-4}$. This may indicate that all the test convergence criteria result in a similar pressure field.

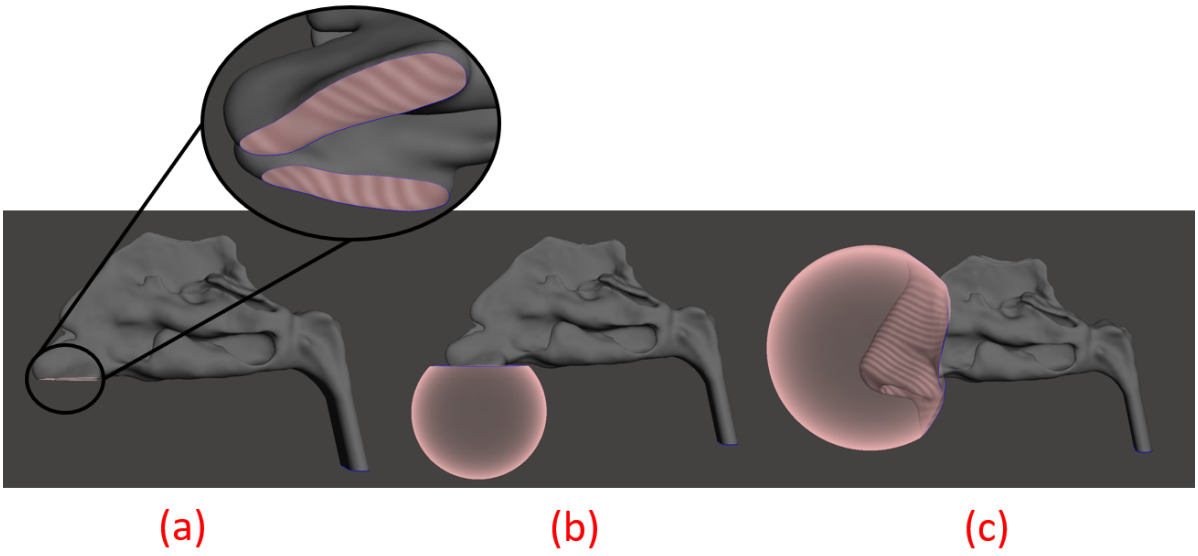


Figure 4.5: Three types of inflow boundary profile configurations are involved in this study. (a): the plane inlet (b): the sphere inlet (c): the inlet with the external nose. Air flows through the pink transparent surface in each configuration.

## 4.3. Configuration of inflow boundary

As we have stated in section 2.2.1, two types of inflow boundary configurations are currently applied: an artificially plane-truncated inlet boundary (named “plane inlet” in later studies) and an inlet boundary combining the external nose (named “external nose” in later studies). Compared to the comprehensive “external nose” approach, the simplified “plane inlet” configuration truncates part of the nasal airway connected to the external airway and the external nose. To reduce the artificial effect near the inlet boundary, we added a small extension at the plane inlet (around $1\times10^{-4}$ m). We deem that this small extension could cause a negligible effect on the flow field. In this study, we select these two types of configurations and one more setup with a hemisphere extended on the plane inlet configuration (named “sphere inlet” in later studies). We consider that the effect of the external nose will be more clear through the comparison between the sphere inlet and the external nose simulation. These configurations will be modeled for the healthy subject (FD2). Other than the modification of the inflow profile, the rest of the nasal airway remains the same. In the future, one may also compare the effect of inflow boundary configurations on NAO patients. However, this will not be discussed in the present study.

These configurations are shown in figure 4.5.

For all three configurations, the same types of boundary conditions are prescribed, as we have discussed in section 3.2.5. The lowest flow rate (10L/min) was selected to avoid potential turbulence effects so that this study can safely apply a laminar model.

### 4.3.1. Area-averaged pressure distribution in the posterior direction

We will first compare the effect of different boundary configurations on the pressure field quantitatively by comparing the area-averaged pressure value. The measurement is investigated through different planes, which are defined at the nostril (slice 1), internal nasal valve (slice 2), nine equal-distance locations posteriorly distributed

from the anterior cavum to the choana (slice 3 to slice 11), and the pharynx (slice 12). The measurement slices were found to be practically perpendicular to the expected mean flow direction (see also figure 1.4). The area-averaged pressure will be plotted against the axial distance along the posterior direction for both the left and right half of the nasal airway. The axial distance is calculated as the distance between the centroid of the current slice and the centroid of the previous slice. For example, we visualize the location of measurement planes on the left unilateral of the nasal airway in figure 4.6.

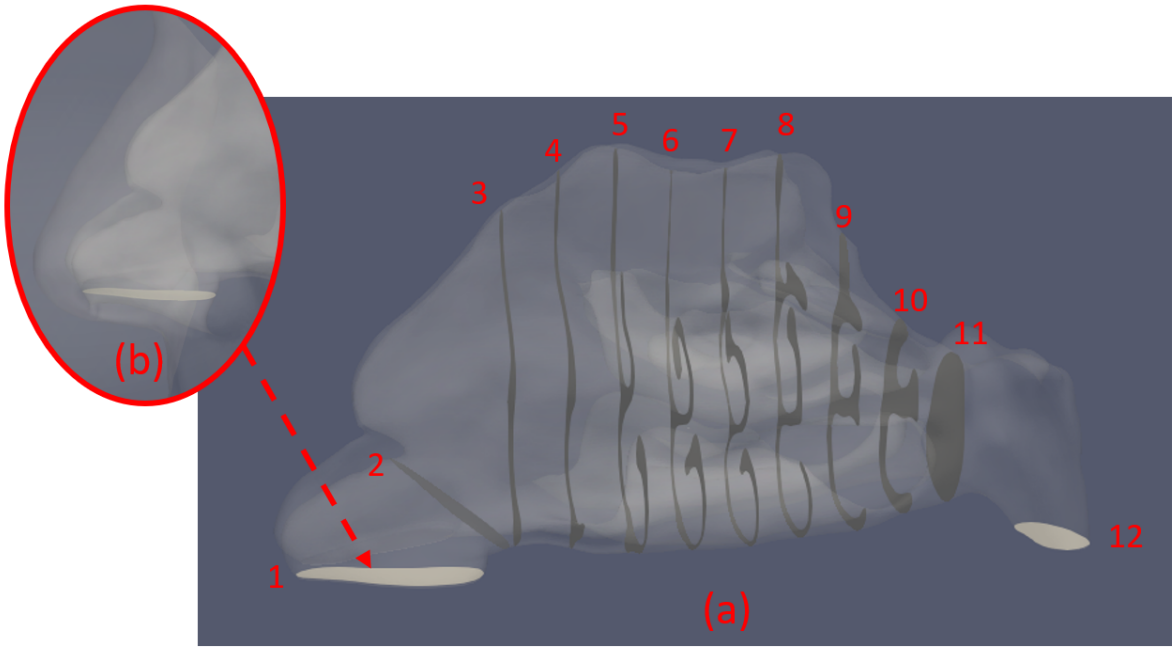


Figure 4.6: For the left side of the FD2 nasal airway, the measurement planes for investigating the area-averaged pressure value are shown in sub-figure (a). Nostril - slice 1; internal nasal valve - slice 2; 9 equal-distance slices - slice 3 to 11; the pharynx - slice 12. Since the plane inlet truncates the airway, to show the relative location of the inlet plane of the plane inlet case within the nasal airway, the location of slice 1 within the external nose setup is shown in sub-figure (b).

Existing research tends to use different definitions of “the pressure”: Some used the static pressure ($p$) and others used the total pressure ($p_{tot} = p + p_{dyn}$, where $p_{dyn} = \frac{1}{2}\rho U^2$ is the dynamic pressure).

Most existing work intends to apply the static pressure to calculate the pressure distribution in the posterior direction, potentially because the static pressure appears in the momentum equation and can be directly obtained from experiments. Wen et al. (2008) compared the area-averaged pressure value under a bilateral flow rate of 7.5 L/min using the ”plane inlet” configuration. They pointed out that static pressure experiences a major reduction passing through the internal nasal valve. The static pressure drop between the nasal vestibule and the beginning of the anterior cavum is around 30% of the static pressure drop for the entire nasal airway. From the definition of total pressure, we could derive that $\Delta p = \Delta p_{tot} - \Delta p_{dyn}$. Therefore, this dramatic static pressure drop ($\Delta p$) is the combined effect of the acceleration due to the geometrical convergence at the internal nasal valve ($\Delta p_{dyn}$) and the friction effect around the nasal valve region ($\Delta p_{tot}$). Similarly, Van Strien et al. (2021) recorded a large static

pressure drop in a subject with a narrow pharynx region (also visible in the healthy subject (FD2), see figure 1.9 (a)), which is also caused by the acceleration effect of a varying area flow.

As an alternative, we deem that the comparison of the total pressure difference between two adjacent slices, to some extent, will only provide the friction loss effect without considering the geometrical variation downstream. For example, total pressure distribution was visualized by Taylor et al. (2010), where they further non-dimensionalized total pressure difference with the dynamic pressure at the internal nasal valve and compared the resulting pressure drop coefficient for both the external nose and the plane inlet of the unilateral nasal airflow at a 6 L/min flow rate. Their findings will also be mentioned in our later analysis.

We state that there is no simple rule of thumb on the better pressure for comparison, and there is also limited research discussing which pressure to be compared in the nasal airflow. In Appendix D, we will briefly discuss the usage matter of static or total pressure in nasal airflow. In this section, both two types of pressure distribution will be calculated to study their variation within different boundary profile configurations. Total pressure distribution (area-averaged, along axial slices) is plotted in figure 4.7, and static pressure distribution is plotted in figure 4.8.

We have the following three observations from figure 4.7.

The first observation is that the total pressure curve shows a different pattern for various configurations. For the external nose case, the total pressure drop from the nostril to the internal nasal valve is the smallest among the three types of boundaries. Downstream to the internal nasal valve, the total pressure value for the external nose setup is always smaller than the other configurations. The overall total pressure drop (from the ambient to slice 12) for the external nose setup is 5.33 Pa, the smallest of all the studied setups. Both the plane inlet and the sphere inlet have a larger total pressure drop within the vestibule and a larger overall total pressure drop (by about 4% for both configurations). The smaller total pressure drop for the external nose setup may indicate that the external nose subject shows the smallest friction loss among the three boundary configurations.

Secondly, we observe that the effect of the inlet boundary configuration on the total pressure tends to become smaller after the third slice. This observation can be seen from the trend of the total pressure curve for all setups. For example, on the left side of the nasal airway, the total pressure drop of the vestibule (slice 1 and slice 2) on both sides has a difference of around 40% between the external nose setup and the plane inlet setup. For the rest slices, this pressure drop difference between the two configurations decreases from 14% in slice 2 and slice 3 and finally arrives at approximately 5% in the nasopharynx. Though qualitatively, this observation was also mentioned by Taylor et al. (2010).

The third observation is that the left and the right side of the nasal airway show high similarity in the posterior distribution of the total pressure. This can be explained by the highly-symmetrical geometry of the nasal airway. Further research into the left-to-right airflow distribution reveals that the flow rate through the nose on either side only differs by 4% (left: 5.11 L/min; right: 4.89 L/min), which is also due to the structural symmetry of the left and right nasal airways. This symmetry will also result in a similar scale of the total pressure drop as well as its distribution over axial slices.

For figure 4.8, similar observations can be drawn as for figure 4.7. Corresponding to the first observation in figure 4.7, we also noticed the difference in the static pres-

sure curve among three boundary configurations. Also, we noticed the smallest static pressure drop within the nasal vestibule and the entire nasal airway for the external nose setup in figure 4.8. Corresponding to the second and the third observation in figure 4.7, we also observed the decreasing impact of the boundary configuration on the downstream nasal airflow and the similarity of the static pressure curve between the left and right sides.

In addition to the similarities, we noticed differences between the static and total pressure curves. Firstly, the static pressure drop (from zero ambient pressure to the static pressure at slice 12) is larger than the overall total pressure drop because of the effect of the dynamic pressure drop. Secondly, the pressure difference between all consecutive slices is less linear, caused by the dynamic pressure difference as a result of the cross-section area difference. We take slice 11-12 (see the zoomed-in part in figure 4.8) as an example. Because the geometry is converging between slice 11 and slice 12 (see figure 1.9 (a)), the flow is accelerating. The accelerating flow speed leads to increasing dynamic pressure. Therefore, the rapid drop in static pressure here is a combination of both total pressure loss and the increasing dynamic pressure. This rapid drop pattern in static pressure is also noticed in Van Strien et al. (2021) under a similar (20 L/min) flow rate. Compared with figure 4.8, total pressure drops less rapidly from slice 11 to slice 12, as seen in figure 4.7, so the effect of the narrow pharynx region is less predominant in the total pressure curve.

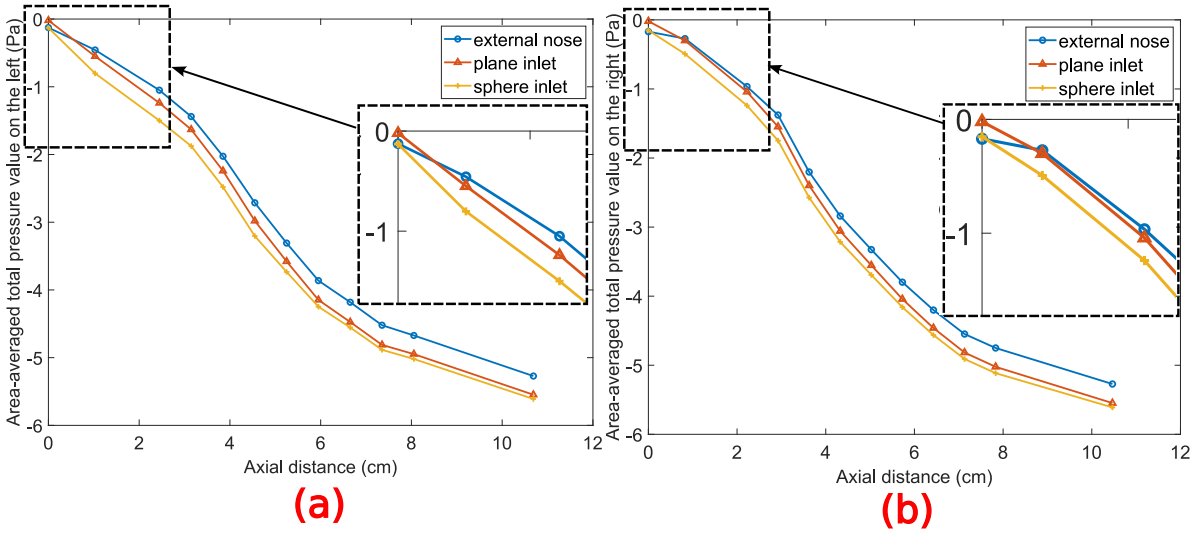


Figure 4.7: The area-averaged total pressure versus the axial distance of each slice is plotted for the left (a) and right (b) sides. The curve of the first three slices is also shown in a zoom-in view. We note that the total pressure for the external nose and sphere inlet cases is lower than zero. This is because the inlet boundary location where we prescribed zero total pressure (see the pink structure in figure 4.5 (b) and (c)) is upstream to the nostril slice. For this reason, upstream of the nostril slice is subjected to the frictional effect, resulting in around 3.4% of the total pressure drop for both configurations. Observations are in the text.

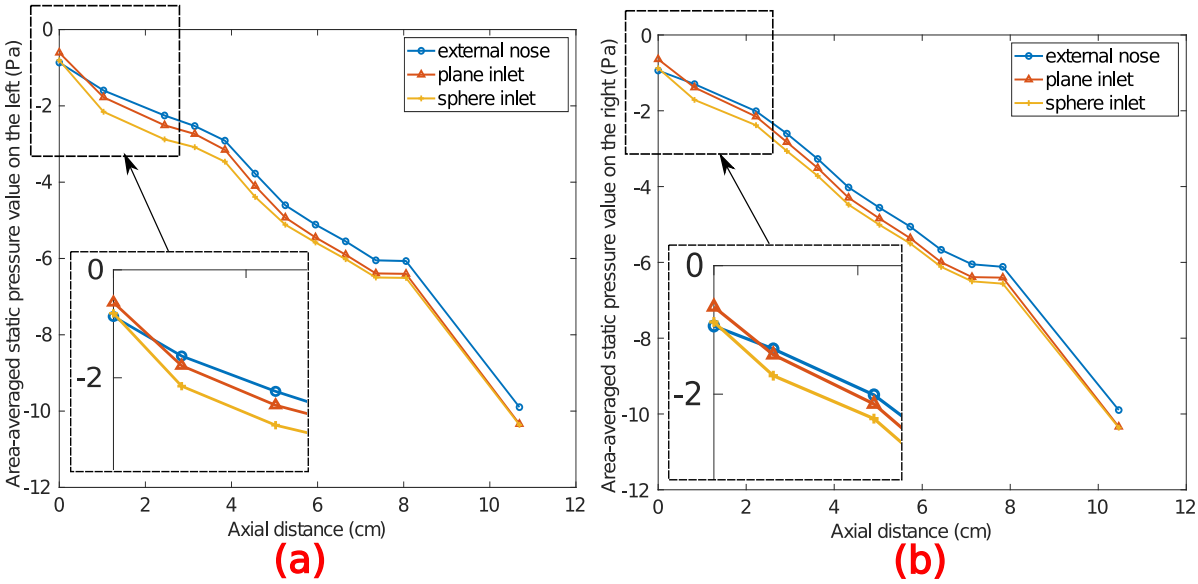


Figure 4.8: Similar to figure 4.7, static pressure against the axial distance of different measurement slices in the posterior direction for the left (a) and right side (b). The trend for the first three slices (nostril, internal nasal valve, and the first slice in the anterior cavum) was zoomed in. Note that the static pressure is smaller than zero because we specified zero total pressure at the inlet boundary so that the static pressure at the inlet is smaller than zero ($p = p_{tot} - p_{dyn}$, $p_{dyn}$ is always positive). The static pressure downstream to the inlet patch is also smaller than zero. Observations are in the text.

### 4.3.2. Velocity profile

The deviation of static and total pressure distribution within different boundary configurations should indicate a difference in the airflow pattern. Additionally, from the second observation in figure 4.7 and 4.8, the impact of the boundary configurations on the nasal airflow should be more predominant in the first three slices. We will investigate the velocity profile to gain further insight into such pressure deviation.

The measurement position of the velocity profile is selected as follows. Initially, because of the similarity between the left and right sides of the nasal airway, the measurement of the velocity profile will be taken only on the left side of the nasal airway. Furthermore, we have observed that the first three slices are affected more by choice of the inflow boundary than the downstream. Because of this, we will select one slice at the nostril, one slice at the internal nasal valve, and two additional slices within the vestibule and the anterior cavum to investigate the velocity profile difference within the inflow area. The latter two slices will be allocated at a short and equal distance from the internal nasal valve slice. In addition, one slice within the end of the turbinate region (slice 8 in figure 4.6) is analyzed to investigate if the velocity profile shows similarity under different boundary configurations. The location of the measurement slices is visualized in figure 4.9.

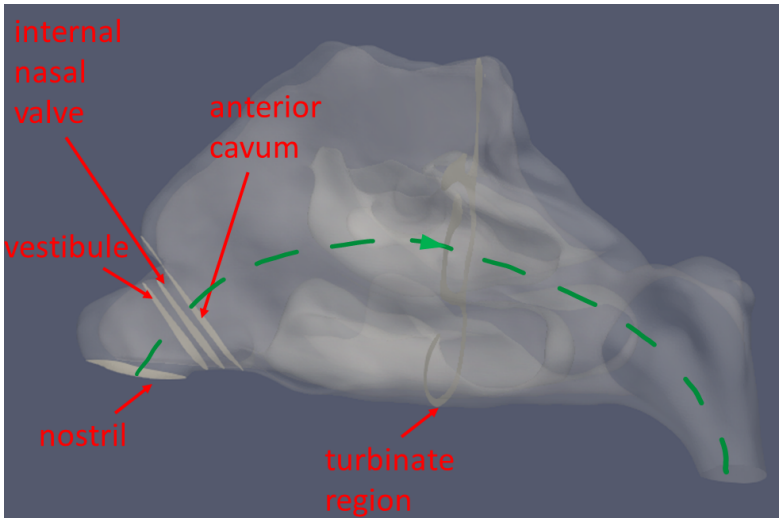


Figure 4.9: The position of the measurement slices is visualized, with the location of the slices in the nasal airway noted. The proposed mean flow direction is indicated with a green dashed line, with its direction pointing posteriorly. As can be seen, the normal direction of slices is aligned with the mean flow direction.

Usually, the velocity magnitude contour is plotted to visualize the flow pattern. However, we consider that such a parameter can not provide the direction of the velocity vector. An alternative is to calculate the surface normal velocity ($u_{normal}$), defined as the projection of the velocity vector ($\underline{u}$) to the slice normal direction ($\underline{n}$):

$$u_{normal} = \underline{u} \cdot \underline{n} \tag{4.1}$$

As one can see from the above equation, the integral of the surface-normal velocity over the entire slice should give the unilateral volumetric flow rate. Therefore, by the $u_{normal}$ contour within different regions of one slice, we can gain insight into the airflow distribution over these regions.

There are two important features of $u_{normal}$. Firstly, the negative sign of $u_{normal}$ can identify the backflow zone. As seen in figure 4.9, the selected measurement slices are approximately aligned with the mean flow direction, so the normal vector of the slices is approximately the mean flow direction. For this reason, the negative part of $u_{normal}$ (velocity vectors have a different direction than the slice-normal direction) is approximately the backflow zone (velocity vectors have a different direction than the mean flow direction). Secondly, $u_{normal}$ can reflect the airflow distribution over a certain region of the slice (the ratio of the flow rate over that region to the flow rate over the whole slice). This is because the surface integral of $u_{normal}$ over a region will provide the flow rate passing through that region, so the airflow distribution can be noticed. With these two features, the surface-normal velocity for each slice is calculated and analyzed as follows.

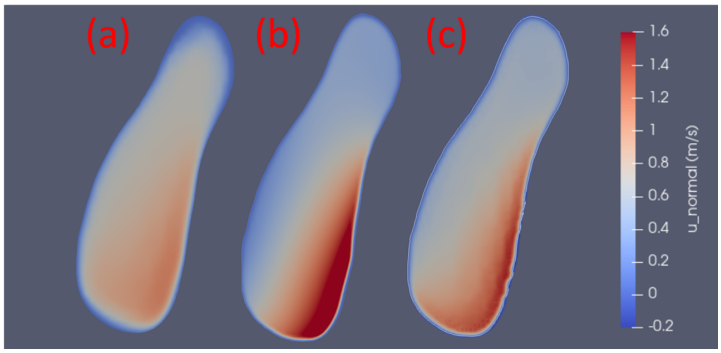


Figure 4.10: Velocity contours of the nostril slice. (a): the external nose case (b): the plane inlet case (c): the sphere inlet case. Explanations are in the text.

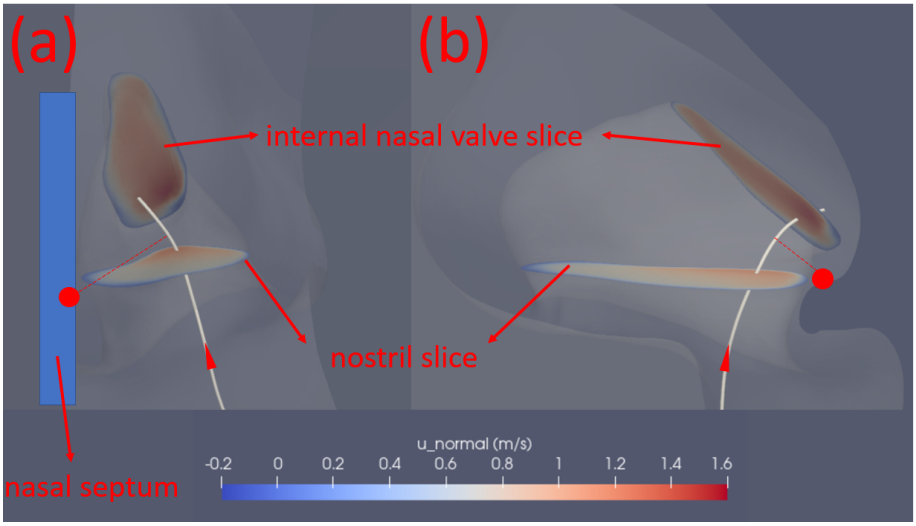


Figure 4.11: The airflow in the nasal vestibule is shown in (a) front view (towards posterior direction) and (b) side view (towards nasal septum). To demonstrate the reason for more surface-normal velocity located near the lower right side of the nostril slice, a representative streamline was drawn. The direction of the curve is marked with a red arrow on the streamline and the center of the curvature is marked with a red circle. The approximated location of the nasal septum is also marked. Observations are described in the text.

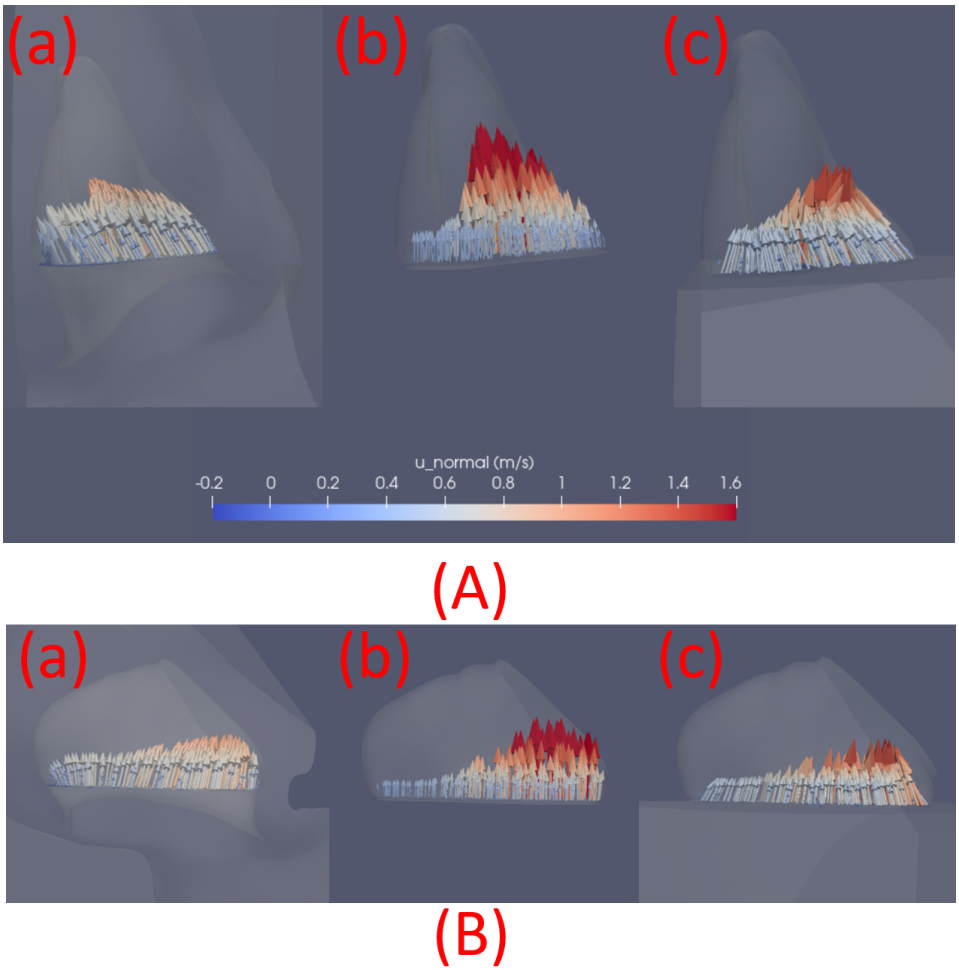


Figure 4.12: Directions of velocity vectors through the nostril slice. Figure 4.12(A) is a front view, and figure 4.12 (B) is a side view of the nasal airway. In both figures, (a): the external nose case (b): the plane inlet case (c): the sphere inlet case. The velocity vectors are colored with surface-normal velocity, to better demonstrate the distribution of $u_{normal}$. Explanations are in the text.

To investigate the effect of inflow boundary configurations on the nasal airflow, we will start with the airflow through the nostril slice (figure 4.10). The flow pattern at the same location (nostril) for each inflow boundary configuration has both similarities and differences. One similarity is that, for all three boundary configurations, the maximum surface-normal velocity always seems to appear at the lower right of the nostril slice in figure 4.10. This phenomenon can be explained by the geometry of the nasal vestibule, as seen in figure 4.11. The location with higher $u_{normal}$ in the nostril slice is anatomically close to both the nasal septum (see figure 4.11 (a)) and the internal nasal valve (see figure 4.11 (b)). As a result, the streamline passing through the vestibule is curved. In figure 4.11, we plot a representative streamline under different views and report that the streamlines passing through other places shows similarity in the curvature direction. The streamline bends towards the nasal septum as seen in figure 4.11 (a) and towards the floor of the internal nasal valve as seen in figure 4.11 (b). Assuming that the flow locally has a negligible viscous effect, the curved streamlines also indicate a change in static pressure, where the static pressure decreases towards the center of the curvature. Since the total pressure along each streamline is conserved,

the velocity near the center of the curvature (the lower right side of the nostril slice in figure 4.10) is larger than the velocity away from the center of the curvature (the rest area of the nostril slice in figure 4.10), which also matches with the finding in figure 4.10 for all three boundary setups.

The difference among the three boundary configurations is that, for the plane inlet and the sphere inlet, the airflow strongly favors the medial and posterior direction of the nostril slice. This airflow pattern can be seen in figure 4.10, where $u_{normal}$ is higher at the lower right corner of the nostril slice compared to the rest area. In contrast, the slice-normal distribution of the velocity vector for the external nose case is more evenly distributed throughout the slice. This difference may come from different directions of the velocity field in different boundary configurations. The velocity direction can be seen by plotting the velocity vector at the nostril slice for each boundary configuration, as seen in figure 4.12. The velocity vectors in the external nose setup show that the airway upstream to the nostril slice redirects the flow towards the posterior and medial direction (see figure 4.12 (A.a) and (B.a)) in a more uniform distribution. This is different in the sphere inlet case (see figure 4.12 (A.c) and (B.c)), where the free entrainment pattern can be seen. For the plane inlet case in figure 4.12 (A.b) and (B.b), because the boundary condition *pressureInletOutletVelocity* regulates an inlet-normal direction inflow, velocity vectors are forced to be perpendicular to the nostril slice. Different airways upstream to the nostril slice resulted in a different flow pattern in the nostril slice among the three boundary configurations.

The difference in the inflow boundary configuration did not only cause the flow pattern of the nostril slice to change, but also caused the downstream flow behavior to vary. As we can see from figure 4.13, the surface-normal velocity of the external nose setup shows a more uniform distribution for both vestibule slices (figure 4.13 (A.a)) and internal nasal valve slices (figure 4.13 (B.a)), benefiting from the inflow profile. In comparison, the airflow still mainly streams favorably in the inferior and medial directions for the other two configurations. The upstream flow pattern within the nasal vestibule also results in a different flow pattern posteriorly, with less airflow going through the lower side of the internal nasal valve and the anterior cavum slice (figure 4.13 (C)) for both the plane inlet and sphere inlet case. This is indicative that the inflow boundary configurations also changed the flow distribution downstream at the anterior cavum slice. Different surface-normal velocity patterns within the nasal vestibule correspond with the difference in axial pressure distribution in figure 4.7 and figure 4.8.

In the further location downstream, we can notice that the surface-normal velocity profile shows only minor differences between these different boundary configurations within the turbinate region slice in figure 4.14, with some slight difference in the magnitude of the velocity maxima in the superior, middle and inferior meatus. This also corresponds with the similarity of the pressure curves further posterior to the internal nasal valve, observed in section 4.3.1.

On a different note, we observe that the recirculation zone happens frequently within the nasal airway, which can be seen by the white arrow. This can be noticed with all the boundary configurations. For example, we could identify a large recirculation zone in the anterior cavum slice (in figure 4.13 (C)), where two arrows at the top are located. Observation of the recirculation zones is not contributing to our discussion in this study, but it is beneficial for the discussion in chapter 5.

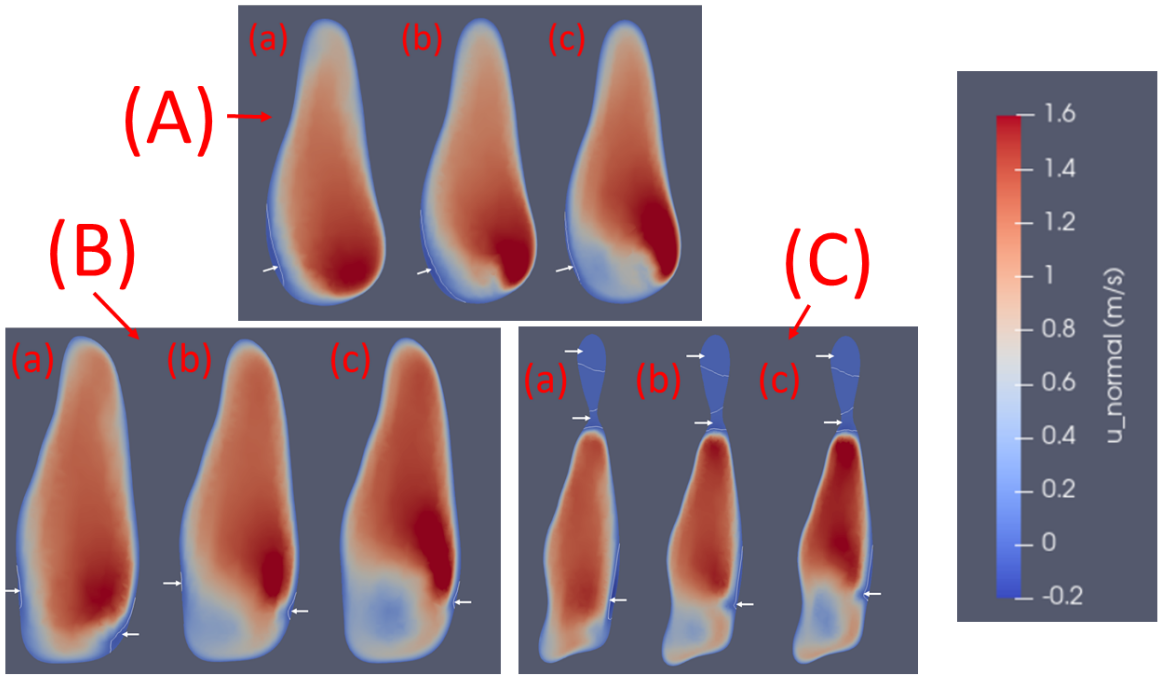


Figure 4.13: Velocity contours (three figures on the left) and color map in this study (the right figure). (A): nasal vestibule slices, (B): internal nasal valve slices, and (C): anterior cavum slices. In each subfigure, (a): the external nose case (b): the plane inlet case (c): the sphere inlet case. The backflow zone is illustrated with a white arrow and is bounded by white lines. Note that the slice size for different locations is rescaled and does not represent the real size in the nasal airway, therefore the slices in the anterior cavum are smaller than the internal nasal valve slices. Explanations for this figure are in the text.

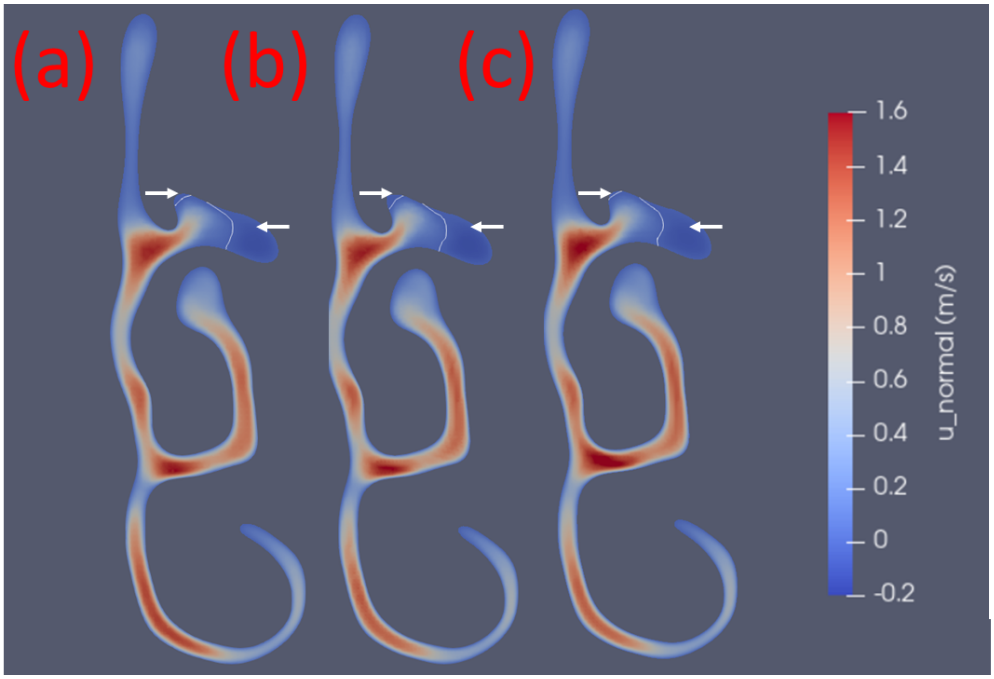


Figure 4.14: The slice of the turbinate region for different boundary setups. (a): the plane inlet (b): the sphere inlet (c): inlet with the external nose setup.

### 4.3.3. Discussion

In this section, we have discussed the effect of different boundary configurations on the flow pattern, especially from the perspective of the pressure distribution and the velocity profile.

Post-processing the nasal airflow is always tricky because of its highly 3D geometry. Currently, there is no universal methodology to post-process the nasal airflow. To discuss the effect of boundary configurations on the downstream nasal airflow, we discussed two methods: static pressure/total pressure (area-averaged) distribution over the selected axial slices. From the comparison between static and total pressure curves, we could state that studying both static and total pressure could lead to similar observations. Therefore, both methods could indicate the preferred boundary configuration. One could further argue that the investigation of area-averaged static pressure versus axial slices combines the information of both total pressure loss (approximately the frictional loss) and dynamic pressure change. Especially, the dynamic pressure change in the static pressure curve will provide more geometrical information (change in cross-section area) than only considering total pressure loss (total pressure curve). We think that the static pressure curve may indicate both the individual (such as a narrow internal nasal valve for NAO patients or the narrow pharynx for healthy FD2 subjects) and the common (converging geometry of nasal vestibule) geometrical variation. Therefore, the usage of static pressure/total pressure distribution over the selected axial slices may depend on the research topic.

Including the external nose in the simulation process is obviously desirable because it provides the most realistic condition for the breathing process. However, applying a plane-truncated inlet boundary has been considered a more straightforward approach in a good deal of existing research. Our study of the healthy subject (FD2) demonstrates that although the overall pressure drop (from the ambient to the pharynx area), both static and total, under different boundary configurations shows a relatively small variation of around 4%. The pressure drop within the inflow area, as well as the flow pattern anterior to the anterior cavum, have shown apparent differences. The additional flow domain in the external nose case, which is left out in the plane inlet case, results in a downstream flow that favors the medial and inferior directions. This may indicate that including the external nose in the calculation is beneficial for the accuracy of the numerical model, despite the additional effort. Therefore, we will integrate the external nose into the simulation for all the case studies.

However, we should note that the discussion only holds for this subject. To draw a firm conclusion on the effect of the external nose, one should also consider the variation of the nasal airflow for individual patients, which requires more datasets. Also, the inflow boundary configuration's effect on the nasal obstructive patient might be interesting to investigate, although this is considered beyond the scope of this thesis.

## 4.4. Grid independence study

In this section, we demonstrate the following problem: is our computational grid sufficiently fine? To answer this question, we will generate a finer grid and compare the flow field difference between both grids. If the difference between a finer grid and our current computational grid is minimal, then our current grid can be deemed as reaching a sufficiently satisfactory resolution.

### 4.4.1. Material

The FD2 subject is selected for this study. Three meshes are involved, two of which are taken from other sections in this study, and one is generated specifically for this section. Of the two meshes in this study, the first is the mesh used in steady-state simulations for sections other than section 5.2, referred to as the “steady-state simulations” mesh in this section. The second mesh is used in transient simulations in section 5.2, named the “transient simulations” mesh in this section. The new mesh for the grid independence study is generated by only changing the base cell size setting (see section 3.2.3) and keeping other parameters in the mesh generation procedure unchanged, compared to the “steady-state simulations” mesh. Specifically, the base cell length scale of the current mesh is 0.8 mm. After refinement, the newly-generated mesh, named “finer mesh” in this section, has a cell length of 0.4 mm. As a result, the cell number of the “steady-state” mesh is 5.89 million, while for the “finer mesh”, the cell number is 36.8 million. The quality of both meshes is checked through the *checkMesh* utility in OpenFOAM.

Since a larger flow rate may result in unsteadiness in the flow field and thus will require finer mesh resolution, in our grid independence study we will select the case with the maximum flow rate (24 L/min) among all the cases. Because the “transient simulations” mesh is not built for turbulence modeling, we will use the laminar model for the grid independence study.

### 4.4.2. Comparison of area-averaged pressure distribution

Since pressure is the main topic of the study, the approach for studying grid independence is through the comparison of the area-averaged pressure along the axial direction, similar to the approach in section 4.3.1.

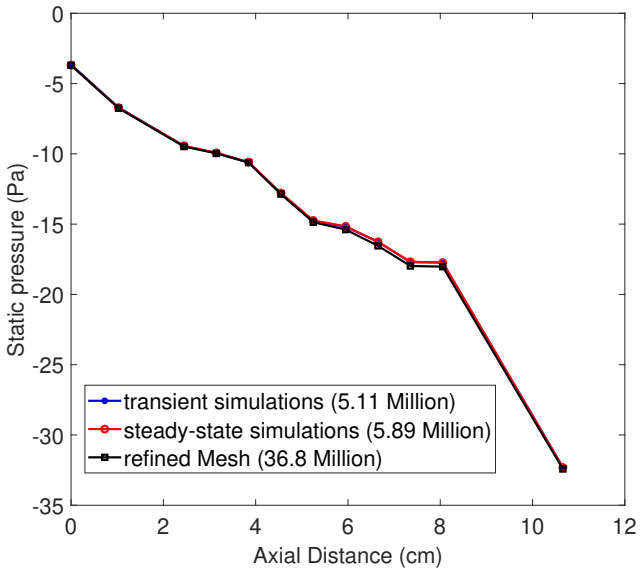


Figure 4.15: The static pressure distribution for slice 1 to slice 12 in figure 4.6 versus the respective axial distances for the “transient simulations” mesh, the “steady-state simulations” mesh, and the “refined mesh”. Two meshes for transient and steady-state simulations almost overlap. The refined mesh has a difference of 1.6% in static pressure near slice 10 and slice 11, compared to the “transient simulations” and the “steady-state simulations” mesh.

As shown in figure 4.15, the trend of the three static pressure distribution curves is strongly similar. Specifically, the static pressure distribution for the “transient simulations” and the “steady-state simulations” mesh has a negligible difference. The difference in static pressure of the same location for the “finer mesh” and the other two meshes is 1.6% maximum, which is acceptable. For the static pressure drop (from the ambient to the pharynx), the static pressure shows a 0.3% difference between the “finer” mesh and the other two meshes. Therefore, the result shows that the static pressure distribution can be well predicted by both meshes used in other sections of this study.

### 4.4.3. Comparison of the velocity magnitude along a line

In addition, to further investigate if the flow field can be sufficiently resolved using the meshes in our study, we also studied the velocity magnitude along one certain line. The measurement location is selected in the internal nasal valve slice (slice 2 in figure 4.6), where the velocity magnitude is the largest in the inflow area. We plotted the comparison of the velocity magnitude under different meshes.

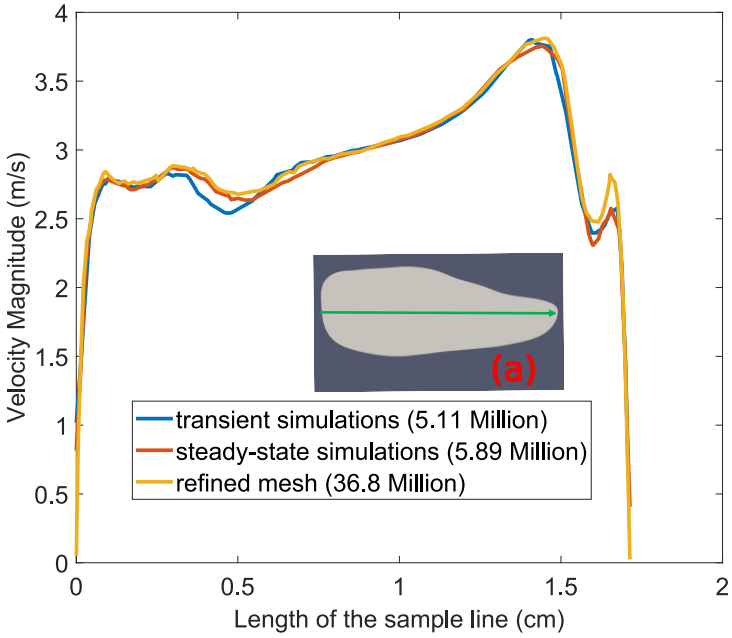


Figure 4.16: The velocity magnitude along one line in the internal nasal valve slice under different meshes is plotted. The line was shown in sub-figure (a). In general, the velocity profiles for three different meshes show an acceptable difference. However, it can be noticed that the “transient simulations” mesh and the “steady-state simulations” mesh may exhibit a less satisfactory result at the locations where the velocity gradient is large.

From figure 4.16, we noticed that the velocity magnitude for three meshes shows a difference when the velocity gradient is high. This difference is presumably caused by the mesh resolution. Because the flow field is linearly interpolated within each cell, sharp velocity gradients can be smoothed out during the interpolation when the mesh is coarser. In comparison, the finer meshes can better capture larger velocity gradients. Therefore, the difference in the velocity magnitude happens.

### 4.4.4. Required computational time

The simulations are conducted in the 28-core Linux Cluster (the *Reynolds* cluster), with Xeon E5-2680 v4 CPU. For the 36.8 million grid, the computation requires about 12 hours. In comparison, using our current mesh with 5.89 million cells took 2 hours to complete the simulation. Such an advantage in CPU time could be more significant when multiple flow rates are elaborated in the study. From the above analysis, we consider the base cell size of our current mesh to be sufficient for the simulation. The later calculation will also use a similar scale of base cell sizes for other subjects.

### 4.4.5. Discussion

The above finding justifies the selection of the computational grid in this study. On the one hand, the “refined mesh” provides better resolution in locations where the velocity gradient is larger with the cost of a higher computational time cost. On the other hand, the two meshes used in our main matter (the “transient simulations” mesh and the “steady-state simulations” mesh) can provide acceptable results in both static pressure distribution and the velocity profile compared to the “refined mesh”. In addition, the two meshes benefit from a shorter computational time. Because there are many case studies in this thesis and the transient simulation requires considerable time to finish, we deem that both meshes used in this study are acceptable.

# 5

# Validation of numerical setup

In this chapter, we will discuss two aspects: the application of the turbulence model and the assumption of the steady-state simulation. We will first address the validation of using the turbulence models by externally validating our simulation with the pressure drop measurements. Next, we will discuss the effect of the steady-state simulation by comparing the steady-state simulation with the unsteady simulation under both constant and sinusoidal inhaling flow rates.

## 5.1. Validation of turbulence model selection

The methodology of the validation procedure is to simulate the growth of static pressure drop under different flow rates (pressure-flow relation) using both the laminar and turbulence models and compare it with the experiments. The experiment aims to validate the turbulence model selection in two applications: (1) bilateral/unilateral airflow and (2) the healthy and NAO patient. Therefore, the experiment should be designed to measure the flow rate and the static pressure drop of healthy and NAO patients for unilateral or bilateral conditions. Although a transitional or turbulent flow will most likely happen at a large flow rate, the individual variation of the nasal airway geometry makes it difficult to define a critical flow rate for different regimes. Therefore, to choose the optimal turbulence setup for pressure drop calculation, $k-\omega$, and $k-\omega-SST$ models, as well as the laminar model, are applied in the simulation for all flow rates both unilaterally and bilaterally. Our final goal is to compare the magnitude of the pressure drop and its growth with respect to the flow rate. To this end, we organized our experimental setup as follows.

### 5.1.1. Experimental and numerical setup

The experiment was set up in the Process & Energy Laboratory, TU Delft. Special thanks to Dr. ir. Willian Hogendoorn and research assistant Ing. Bart Hoek for collaboration. The setup is introduced as follows. We selected two subjects as representatives, one healthy subject (FD2) and one NAO patient (scan2). The flow rate in the unilateral airflow experiment is selected as 5 L/min to 12 L/min, and the bilateral flow rate is 10 L/min to 24 L/min. We have justified the choice of the bilateral flow rate in section 2.2.3. The unilateral flow rate is half of the bilateral flow rate, which is almost true for a symmetrical, healthy nasal airway. The justification for this can be found in section 4.3.1, where we have found that under the bilateral flow rate of 10

L/min, only a 4% difference can be found between the flow rates through each side for the FD2 subject. Yet, the selection of unilateral flow rate has to be justified for NAO patients. However, the two reasons below motivated us to use the same flow rate (half of the bilateral flow rate) as healthy subjects in NAO patients. Firstly, although not yet concluded, in principle, if the structure is constrained due to nasal obstruction, then more than half of the flow should favor the non-obstructed side. Using a higher flow rate than reality on the obstructive side may cause certain variables to increase, which may benefit the NAO detection using CFD. Secondly, if unilateral airflow is to be investigated in research, using a uniform selection of the unilateral flow rate for all the subjects will reduce the simulation effort.

Considering the available measurement equipment in the laboratory, the flow rate and the static pressure drop were measured mechanically using a rotameter and Betz-manometer. Another approach would be to measure these quantities digitally, which is more accurate than the current approach. However, the appropriate pressure sensor was not directly available at the time. The experimental setup is shown in figure 5.1 with a photo and a schematic view of the setup.

The justification for the selection of measurement tools and the design procedure will be given here:

1. **The 3D printed nasal airway models:** The primary consideration for designing the 3D printed model is the possible leakage issue. To this end, two special designs are made. Firstly, we designed connectors at the joining between the nose model and the round pipe connecting the measurement device downstream, as seen in the bottom part of figure 5.2. To be compatible with the connector, we designed the nasal airway model internally in a solid “box” with the patient-specific external nose on the front (labeled “part 1” in figure 5.2 (b)). Secondly, the “nose box” was also designed with an O-ring groove and connected with the connector using bolts. The O-ring design prevents air leakage between the “nose box” and the connector. Such mechanical modeling was carried out with *SolidWorks* and then exported to *PreForm* for 3D printing. The solid model is then printed using *Formlabs 3B+* (Somerville, MA) 3D printer. Printing material is selected as clear resin, a Stereolithography (SLA) liquid material that solidifies under UV light, which will prevent the model from leaking. The layer thickness was set to be 0.05 mm, and it took around 26 hours for each printing to complete.

   In a previous experiment, nose models were printed using a fused deposition modeling printer, which prints a 3D object layer by layer using melted filaments. However, these models were later found to leak, presumably caused by the considerable distance between adjacent filaments. To further prove that the resulting printing is airtight, we made a waterproof test after obtaining each printed object. As the models are designed for bilateral measurement, we used tape to seal the nostril inlet for the unilateral measurement, as seen in the zoom-in part of figure 5.1. To ensure air-tightness for the unilateral measurements, we temporarily block the unsealed side of the nostril and read the rotameter measurement before each measurement. If the flow rate shows zero, the sealed nostril is airtight, and we proceed to the experiment.

2. **Betz-manometer:** The Betz-manometer in this study has a pressure measurement range of $0mmH_2O \sim 50mmH_2O$ (equivalent to $0Pa \sim 490Pa$), with the minimum scale of $0.1mmH_2O$ $(0.98Pa)$. This measurement range is considered

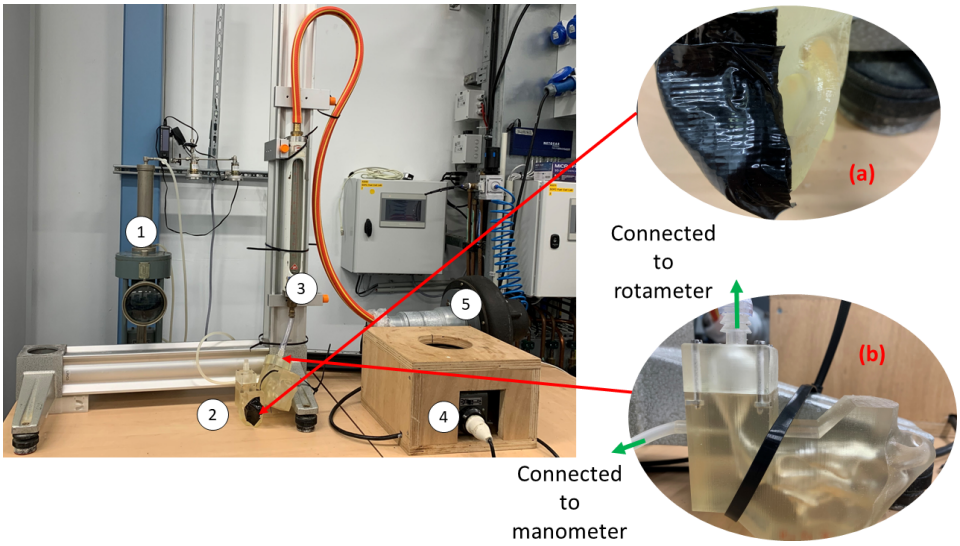


(a) A photo of the experimental setup. Essential components are labeled.

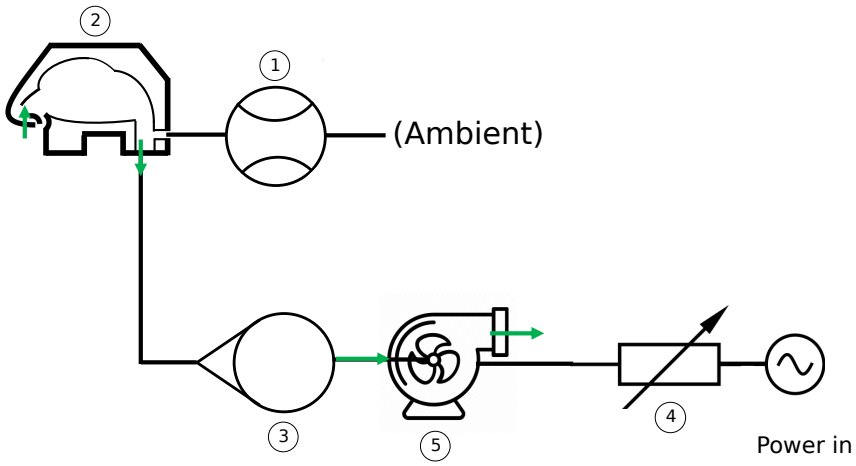


(b) A schematic drawing of the experimental setup, with similar labels as the figure (a)

Figure 5.1: The configuration of the experimental setup can be seen in figure 5.1 (a). The labels represent 1-manometer, 2-nose models, 3-rotameter, 4-rheostat, and 5- centrifugal ventilator. The two nose models in the picture are the 3D-printed healthy (FD2) and NAO (scan2) patients. For the unilateral airflow measurement, the nose model has a tape covered on the nostril (see sub-figure (a)). The bilateral measurement can be directly conducted, as one can see from the model on the right. The rear side of the nose model (FD2) is zoomed in to show the connection between the nose model and the other measuring devices, as shown in sub-figure (b). These connected measuring devices are to measure the pressure and the flow rate.

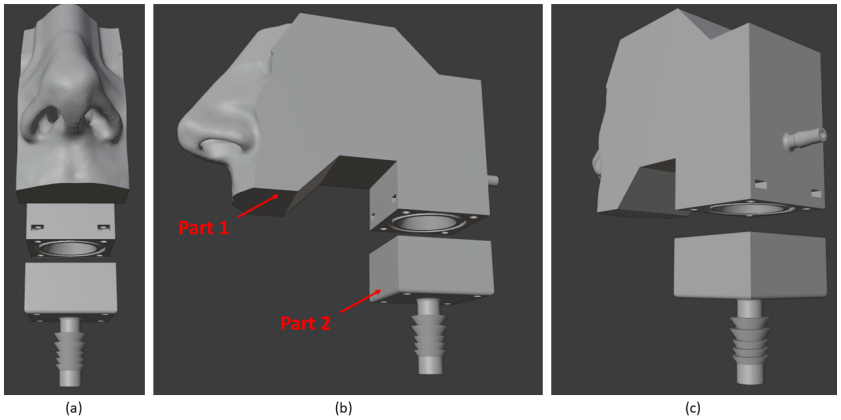


Figure 5.2: The design of the 3D printing model for FD2 subject pressure drop measurement is visualized. The upper part of all three figures is the nasal airway model, while the lower part is the connector. In figure (a), a front view is shown. The airflow in the 3D model will pass through the external nose at the front into the nasal airway, which is embedded inside the “nose box”. The outlet of the nose model is connected with the inlet of the connector using bolts. The hose tail shape of the connector (the bottom of the figure) is specially designed for pipe connection. An O-ring groove is designed at the bottom of the nose model for air-tightness, which is more visible in figure (b). In figure (c), an attached port with an inner diameter of 2.5 mm can be seen, placed at the pharynx region, to connect the nose model with the manometer.

sufficient for our requirement. The working principle of a manometer requires that the device must be placed vertically. We made adjustments every time before the measurement to ensure the correct vertical positioning. In the current setup, the manometer is connected perpendicular to the flow direction (see the zoomed-in view of figure 5.1), so the static pressure at the pharynx location will be measured.

3. **Rotameter:** At the time of the study, the only calibrated rotameter has a measurement range of 10 L/min to 100 L/min, with a minimum scale of 1 L/min. We should note that the minimum flow rate that this rotameter can measure is larger than the minimal unilateral flow rate in our study. Therefore, only larger flow rates of the unilateral experiment can be measured by the calibrated rotameter. The other available rotameter at the time was uncalibrated with an approximated maximum measurement range of 30 L/min. To make lower flow rates measurable, we connected the uncalibrated rotameter with the calibrated one to perform a hands-on calibration. We then could extrapolate the scales of the uncalibrated rotameter by measuring the overlapping flow rates using the calibrated one.

4. **Centrifugal ventilator and rheostat:** In principle, the flow field should be driven by air extraction in the pharynx region to mimic the inhaling process. Therefore, a centrifugal ventilator is required. In order to control the output power and the flow rate of the centrifugal ventilator, a rheostat is connected. The maximum flow rate depends on the overall pressure drop of the setup. In this study, it can smoothly generate a flow rate ranging from 7 L/min to 40 L/min, which is suitable for our requirement.

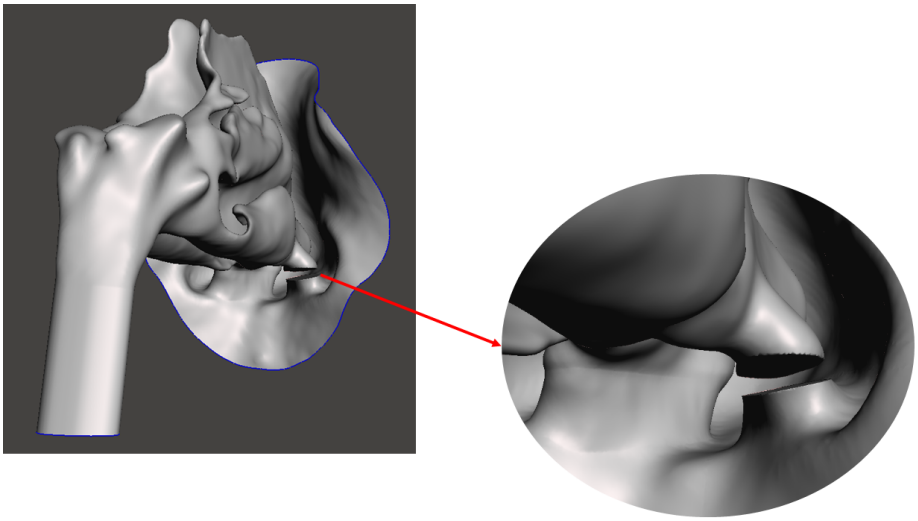

Figure 5.3: The configuration of the unilateral flow model for simulations is demonstrated. The majority of the airway stays unchanged from the bilateral simulation, except for the zoomed-in section. In the zoomed-in section, the joint between the nostril and the vestibule is artificially disconnected.

With the above setup, each measurement was repeated three times and the average value was calculated as the final result.

The numerical setup is as follows. The bilateral airway models used in the simulation are the same as in the experiment. However, to model the unilateral airflow, we artificially disconnected one side of the airway from the nostril inwards, as seen in figure 5.3, so that the airflow will only pass through the other side. The turbulence modeling methods are selected as the laminar model and two RANS models, namely the $k-\omega$ and the $k-\omega-SST$ model. The motivation for such selection is given in 2.2.3. Two sets of boundary conditions are selected for both RANS models. The first kind is based on the turbulent viscosity ratio of 5 and turbulent intensity of 2.2%, as applied in Li et al. (2017). However, we deem that in the restful breathing condition, the turbulence level in the air may be lower than these suggested values. Therefore, we proposed another boundary condition. The turbulence intensity, measured by Schlichting et al. (2003), is obtained from the free stream in the low-speed wind tunnel. The turbulent viscosity ratio is 2, and the turbulent intensity is 0.02%. In the results below, “large” represents RANS models with the first set of boundary conditions, while “small” denotes the simulation based on the second set. The pressure drop is calculated with the pressure value at the same location in the 3D-printed model where we measured static pressure drop.

Because the pressure-flow relation is the primary focus of this section, it is critical to understand how it can be represented. We used both total and static pressure for comparison in section 4.3. However, because the measurement can only capture static pressure, we will refer to “pressure” in this context as static pressure. There are several ways to visualize the pressure-flow relation. The first and most common method is to plot the pressure and flow rate directly, which can be found in Wen et al. (2008), Weinhold et al. (2004), and Van Strien et al. (2021). In addition, a log-log scale can also display the pressure-flow relation, resembling a dimensional Moody chart (see White (2011)). With a log-log scale, the pressure-flow relation can be identified

by a linear line. One might also consider non-dimensionalizing the pressure drop and the flow rate. However, in this study, we noticed that the minimal cross-section area locates differently (for FD2: pharynx, and for scan2: internal nasal valve), which resulted in a remarkable difference in the scale of the non-dimensional parameter. Further description can be found in Appendix A. The above analysis motivates us to plot the dimensional pressure drop and the flow rate on a log-log scale diagram.

### 5.1.2. Bilateral comparison between simulations with experiments

The bilateral pressure-flow relations are plotted below in figure 5.4 for the FD2 subject and in figure 5.5 for the scan2 subject. To structurally analyze the result, we will explain the pressure-flow relation based on the measurement data of figure 5.4 and 5.5 and then present our observations.

We will first comment on the scale of the static pressure drop. As one may notice, the static pressure drop for the healthy (FD2) subject is generally higher than the static pressure drop for the NAO (scan2) subject. For example, at the flow rate of 24 L/min, the FD2 subject has almost twice the static pressure drop as the scan2 subject. This contradicts our conventional understanding, where we expect a higher pressure drop for a nasal “obstruction” patient. There can be two reasons for the unusual pressure drop difference. The first is the interpersonal variation of the nasal geometry. By comparing the volume of the two subjects, we find that the FD2 subject has a smaller volume ($2.67 \times 10^{-5} m^3$), while the scan2 subject has almost twice the volume ($4.66 \times 10^{-5} m^3$). Because the larger volume will result in a lower velocity magnitude, although the scan2 subject is symptomatic, the static pressure drop for scan2 is still lower than for the healthy FD2 subject. The second aspect is the flow distribution difference between the obstructive side and the non-obstructive side of the scan2 case. We notice that only around 24% of the airflow goes through the obstructive side of the nose for this subject, while the majority of the air (76%) is transported through the healthy side. This behavior in which the airflow is redistributed in favor of the healthy side is more prominent under larger flow rates. Therefore, the bilateral pressure drop across the nasal airway is reduced compared to the bilateral pressure drop of an evenly distributed airflow on both sides of the nose. Since the bilateral interpersonal comparison of the pressure shows a counter-intuitive result, in section 5.1.5 we will compare the unilateral pressure drop.

Furthermore, we have some comments regarding the growth of the pressure-flow relation to see if the flow falls in the viscous-dominated or the inertial-dominated region. This can be seen in two approaches. The most straightforward approach is to compare the steepness of the pressure-flow relation with the linear (the green dash line in the main figure of figure 5.4 and 5.5) and quadratic trend line (the black dash line in the main figure of figure 5.4 and 5.5). One can see that none of the data (including experiments and simulations) follows the linear trend line for the lower flow rates nor a quadratic relation for the higher flow rates. The quantification of the error predicted by both trend lines is visualized in the corner sub-figures in figure 5.4 and 5.5. Through the scale of the error, we notice that the linear relation correction increases up to 45% as the flow rate increases in both subjects. In contrast, the quadratic correction increases to a smaller scale (around 20%) as the flow rate decreases. Therefore, the pressure-flow relation shows a closer correlation to a quadratic behavior ($\Delta P \sim \rho U^2$). Moreover, the larger flow rate in this study shows a trend closer to the quadratic profile. Specifically, for both subjects, the quadratic correction is within 5% down to 20 L/min.

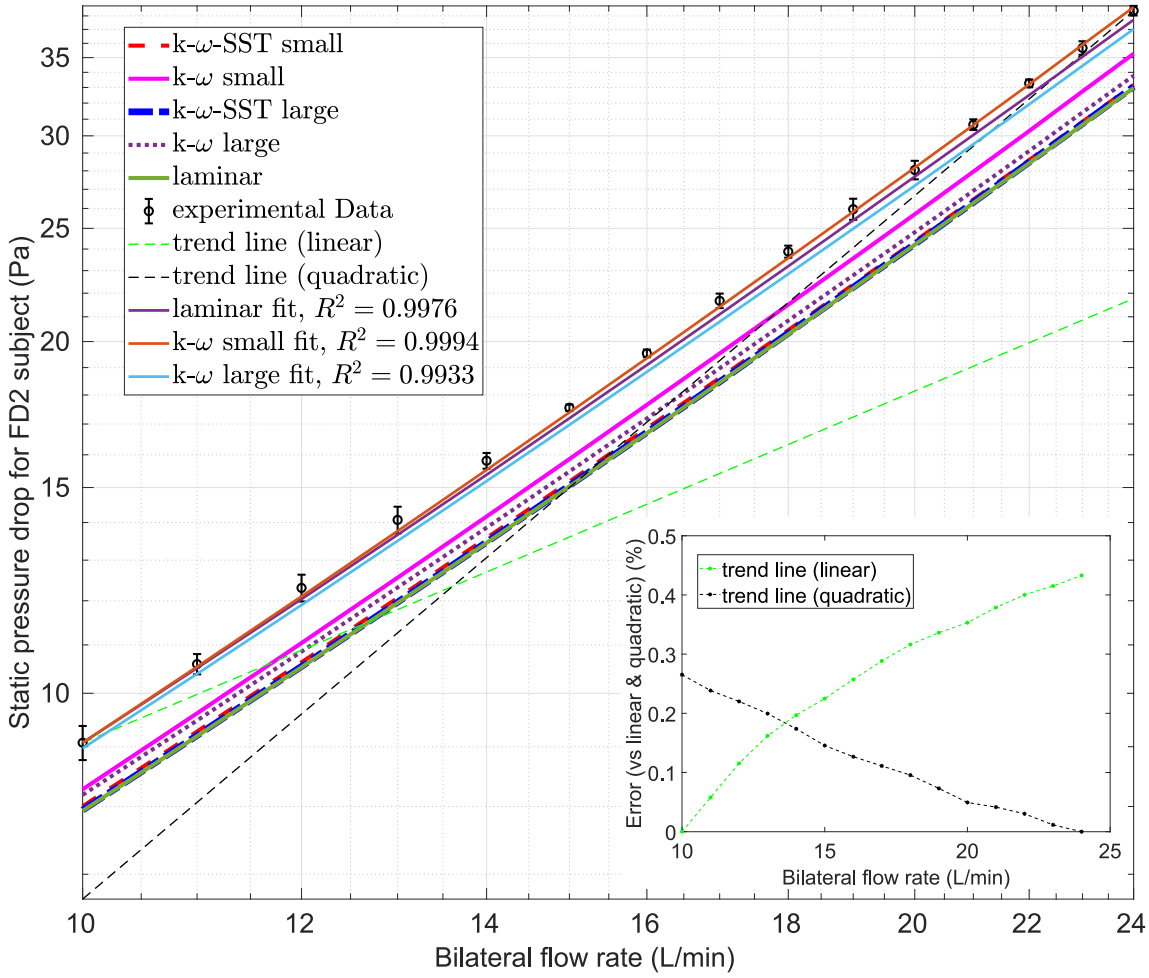


Figure 5.4: Bilateral static pressure drop measurement versus flow rate (with error bar representing standard deviation over three times of measurement) for the FD2 subject, compared with the simulation results using four different RANS setups and the laminar model. Linear and quadratic trend lines are plotted to show static pressure drop growth trends with increasing flow rates. We also shifted the fitted simulation curve to the first measurement point to visualize the consistency of the pressure growth trend. Additionally, we plotted the error between the experimental data and the pressure drop predicted by the trend lines in the sub-figure. Discussions are in the text.

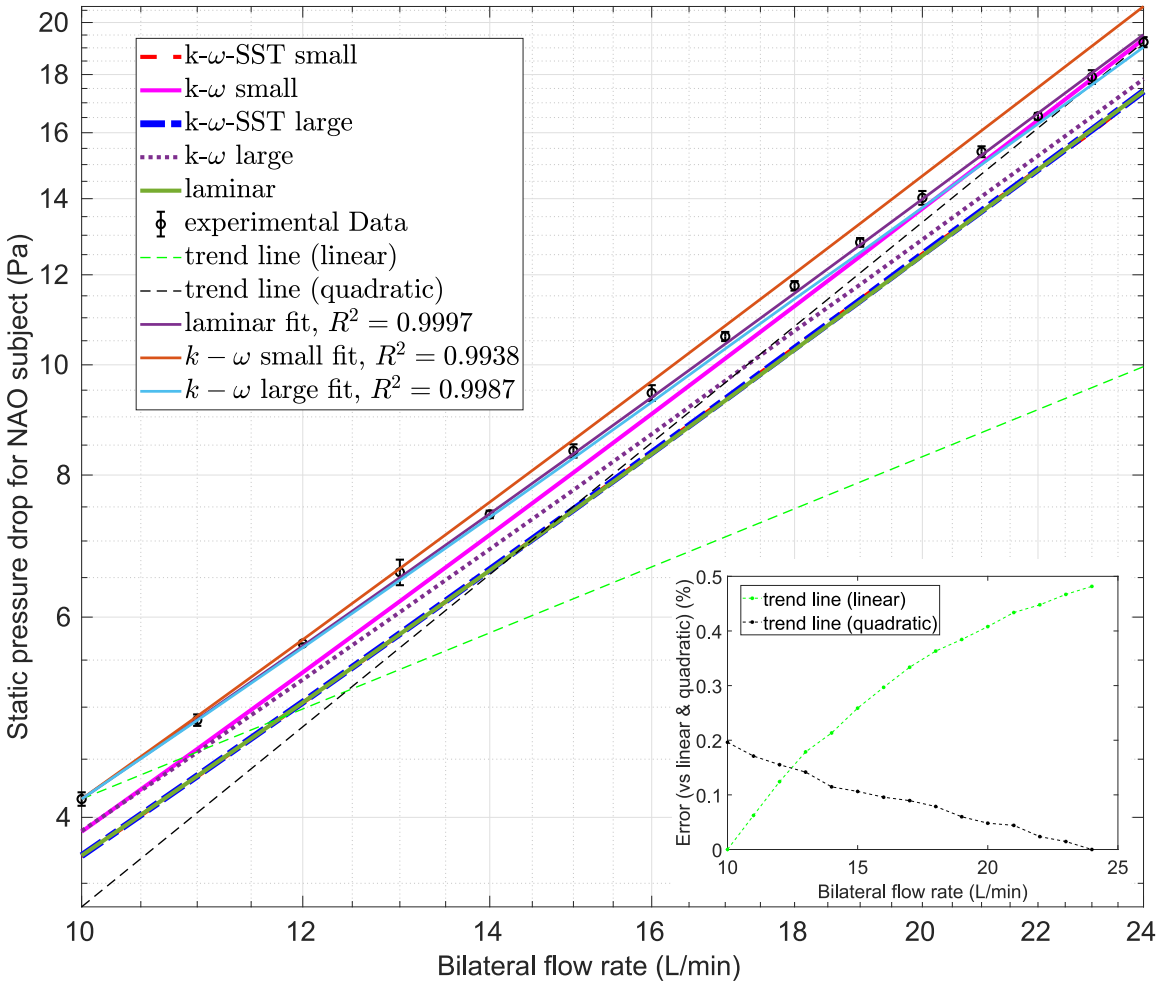


Figure 5.5: Pressure-flow curve of the scan2 subject. Additionally, we plotted the error between the experimental data and the pressure drop predicted by the trend lines in the sub-figure. Objects in the figure are similar to figure 5.4. Discussions are in the text.

In addition, we can quantify the pressure-flow relation through curve-fitting. We find that the power function can provide an accurate estimation through the curve-fitting for all the simulations and experiments. The measurement data, for instance, can be neatly fitted using $0.2075 \times Q^{1.6411}$ for FD2 (healthy subject); and $0.071 \times Q^{1.7632}$ for scan2 (NAO subject), with both $R^2 = 0.9999$. The good fitting by $\Delta P = a \times Q^b$ function explains the reason the pressure-flow relation in figure 5.4 and 5.5 behaves linear on double-log scale diagram. From the above observations, we note that for all our studied cases, pressure drop scales with flow rate to a power between 1 and 2. This factor may suggest that the pressure drop results from both viscous and inertia effects. In addition, the comparison of linear and quadratic correction, as well as the exponents of the curve-fitting function, is more indicative of the inertial transport effect rather than viscous resistance.

From figure 5.4 and 5.5, we notice that the pressure drop value and the steepness of the pressure-flow relation vary among turbulence modeling setups. We have the following observations regarding different turbulence modeling approaches.

Our first observation is regarding the comparison of the static pressure drop value between simulations and measurements. Figures 5.4 and 5.5 suggest that the measured static pressure drop appears to be higher than every simulated result. Of all the tested turbulence modeling setups in this study, the $k-\omega$ model with a smaller prescribed turbulent quantity showed the best correspondence with the static pressure drop measurement. Specifically, the pressure drop difference between the measurement and the "$k-\omega$ small" model is around 10% for the healthy (FD2) subject and from 1.6% (24 L/min) to 4% (10 L/min) for the NAO (scan2) patient. Other turbulence models have shown about a 14% difference in the static pressure drop for the healthy (FD2) subject and about 12% for the NAO (scan2) subject. The "$k-\omega$ large" model is found to give a more inaccurate approximation compared to the "$k-\omega$ small" model. However, it is marginally better than all other models. Using other RANS setups, including the two $k-\omega-SST$ models and the laminar model, shows a similar static pressure drop to the laminar model. Therefore, this may indicate that the models do not detect a fully turbulent flow field for these RANS setups. Also, for the setups except for $k-\omega$ models, the error did not show a strong correlation with the flow rate, which may indicate that the error caused by the turbulence model is not dominant.

To quantify the prediction of the pressure-flow relation further using simulations, we translated the simulation curves vertically to the first point (10L/min) of the measurement and compared the accuracy of simulation prediction using the $R^2$ value. In a log-log plot, parallel lines indicate the same scale of pressure-flow relation. If the pressure-flow relation indeed fits a $\Delta P = a \times Q^b$ function, as we have noticed earlier, $b$ would stay the same for parallel lines. Therefore, a larger $R^2$ value means a better correlation between the shifted simulation curve and the measurement data, hereby representing a better prediction by the simulation. We choose not to plot the $k-\omega-SST$ models because they predict the same trend as the laminar model. As shown in the "fitted" curves of figure 5.4 and 5.5, we notice that almost all the simulated curves showed a good fitting to the measured pressure-flow relation with 99% coefficient of determination ($R^2 > 0.99$). Of all the three turbulent setups, the $k-\omega$ small model underestimated the pressure-flow relation of the FD2 subject, and the $k-\omega$ large model overestimated the slope of the scan2 subject. In comparison, the laminar model gave a relatively reasonable prediction for both subjects.

From the above analysis, we notice that all the above modeling approaches gave an

accurate prediction of the pressure drop with an error of less than 15%. In addition, all the models also gave a reasonable approximation of the pressure-flow relation. However, we notice that (1) the experiments show a constant deviation to the laminar and the $k-\omega-SST$ models, and (2) the $k-\omega$ models showed a different behavior than other models. The first note motivates us to find a possible explanation for this error in section 5.1.3, and we will visualize the flow regime predicted by the RANS simulations in section 5.1.4 for the second note.

### 5.1.3. Reasons for the static pressure drop deviation between simulations and experiments

Two explanations can be found for the observation that the simulations always show a smaller static pressure drop than the experiment. The first explanation would be the uncertainty of the rotameter. Based on the rotameter measurement report, the measured flow rate should allow for a 3 percent error. The second explanation is the potential geometry change of the 3D printed model.

To explore the second explanation, we CT-scanned the 3D-printed model and reconstructed the new CT-scan using the same segmentation setup as when we first made the simulation model. The resulting airway from the CT scan of the 3D printed model is then compared with the simulation geometry in a back-of-the-envelope manner. The comparison is through the total volume of the airway and the surface area of three slices located at the anterior cavum, the turbinate region, and the pharynx region shown in figure 5.6.

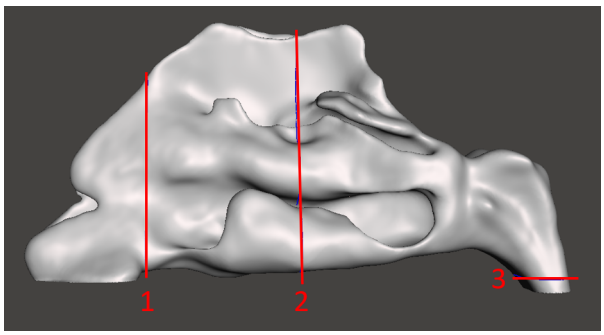


Figure 5.6: The deviation of the experimental geometry from the simulation geometry was investigated through the total volume comparison and the cross-section area comparison at three locations: the anterior cavum (slice 1), the turbinate region (slice 2), and the pharynx region (slice 3).

| Geometry name | Total volume ($m^3$) | Slice 1 area ($m^2$) | Slice 2 area ($m^2$) | Slice 3 area ($m^2$) |
|---|---|---|---|---|
| Geometry for validation | $2.72 \times 10^{-5}$ | $2.43 \times 10^{-4}$ | $2.75 \times 10^{-4}$ | $0.97 \times 10^{-4}$ |
| Simulated geometry | $2.61 \times 10^{-5}$ | $2.32 \times 10^{-4}$ | $2.61 \times 10^{-4}$ | $1.00 \times 10^{-4}$ |

Table 5.1: Both the total volume and the area of slice 1 and slice 2 for the 3D printed airway increased by around 4% compared to the simulation airway. This difference could be artificial, potentially because of the threshold in the segmentation process. As there is no existing threshold selection standard, obtaining the real volume of the models is impossible. Such a threshold is expected to cause the entire airway to enlarge. However, even with a threshold causing the volume to increase, the cross-section area at the pharynx still decreased by 3%.

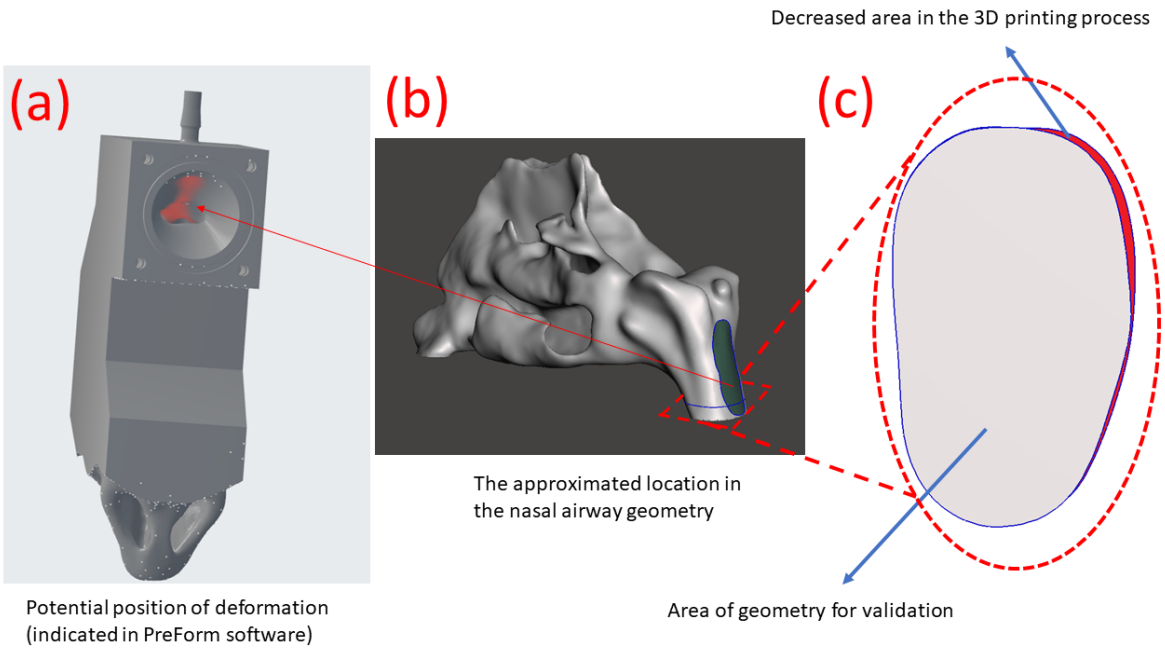


Figure 5.7: The area change of the pharynx slice is explained. In figure (a), the potential position of deformation was indicated in the 3D printing software. It locates internally at the rear side of the pharynx airway. This marked region is approximately located in the green-colored region of figure (b). The pharynx slice in figure 5.6 locates within this region and was zoomed-in in figure (c). In figure (c), we show this specific slice from the geometry for validation (the smaller white color area) and the deformed region compared to the simulated geometry (the red area). If we assume that the anterior structures (slices 1 and 2) for the simulation and the printed geometry have the same area, then the deformed area takes up 7% of the total area of slice 3 in the simulated geometry.

By analyzing the pharynx slice in figure 5.7, we deem that, near the pharynx region, the airway could deform because of lacking supporting structures. In 3D printing, supporting structures are usually added to prevent structures from deforming. The potential deformation locates inside the geometry. However, supporting structures cannot be added inside the nasal airway because it is impossible to remove them after the printing is completed. Altering the orientation of the model during the 3D printing process could, to some extent, resolve the deformation. However, because of the size limitation of the 3D printer, the current orientation was the only possible approach. This orientation will lead to a narrower airway (as one can see in figure 5.7(c)), because of which a higher pressure drop is measured. To exclude the effect of the segmentation threshold, we can approximate the resulting pressure drop difference by assuming that slice 1 and slice 2 have the same area. The resulting pharynx area difference is around 7%. Using the curve-fitted equation of the measured pressure-flow relation, we approximated the measured pressure drop to be 11.7% higher than the simulated pressure drop, similar to the magnitude of the constant error found in the previous section. Nevertheless, the precise amount of error caused by the 3D printing process is uncertain.

### 5.1.4. Turbulent viscosity ratio

One possible explanation for the higher static pressure drop predicted by the $k-\omega$ model is the additional turbulence effect, which can be visualized by the turbulent

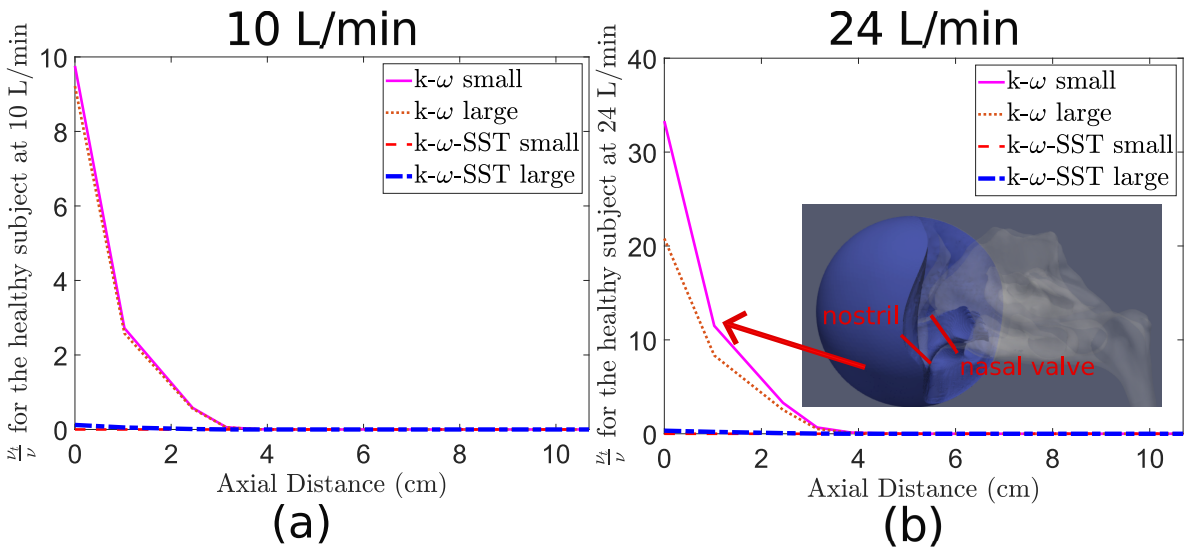


Figure 5.8: The area-averaged turbulent viscosity ratio versus the distance of axial slices of the healthy (FD2) subject is displayed. In addition, the contour of the turbulent viscosity ratio larger than 5 is plotted in figure (b), obtained from the "$k-\omega$ small" setup under the flow rate of 24 L/min. Of all the measured slices for the $k-\omega$ models, the turbulent viscosity ratio shows the highest magnitude at the nostril for both 10 L/min and 24 L/min. The value at the nostril slice is at least doubled compared to our prescribed turbulent viscosity ratio at the inlet. The contour indicates that a large turbulent zone fills the entire external nose area and extrudes into the vestibule. The turbulent viscosity ratio keeps decaying downstream and reaches a value close to zero near the pharynx plane. In comparison, for the $k-\omega-SST$ models, an almost zero magnitude of turbulent viscosity ratio holds for both flow rates.

viscosity ratio. The turbulent viscosity ratio ($\frac{\nu_t}{\nu}$) is defined as the ratio of turbulent viscosity ($\nu_t$) to molecular viscosity ($\nu$). The turbulent mixing is directly related to the turbulent viscosity in eddy viscosity models, so we could learn whether the turbulent model indicates turbulence by comparing the resulting turbulent viscosity ratio. For simplicity, we select the flow field at the minimal (10 L/min) and maximal (24 L/min) flow rates for both subjects and calculate the area-averaged turbulent viscosity ratio at different locations. The measurement locations are selected with a methodology similar to the area-averaged pressure investigation in section 4.3.1. For both subjects, the slices locate in the left airway. The results are shown in figure 5.8 and figure 5.9.

Note that the turbulent viscosity ratio for the $k-\omega$ small model at the nostril slice is above 5 times the prescribed boundary condition at the flow rate of 10L/min and about 16 times the prescribed value at the 24 L/min flow rate for both subjects. The turbulent viscosity ratio is 2 times and 5 times the boundary-prescribed value for the $k-\omega$ large model at 10 L/min and 24 L/min flow rates, respectively. Such high turbulence mixing is only generated within the flow field from the hemispherical boundary to the external nose under the prediction of $k-\omega$ models, which we deem to be physically impossible. In addition, we notice that changing the prescribed turbulent kinetic energy ($k$) and dissipation rate ($\omega$) dramatically affects the predicted turbulent quantities at the inlet. Surprisingly, a larger prescribed boundary value decreased the amount of turbulent viscosity entering the nostril.

The behavior of the $k-\omega$ model was well studied in Durbin et al. (2010). The excessive turbulent viscosity ratio may come from the fact that the $k-\omega$ model can show a significantly large turbulence production near the outer part of an adverse

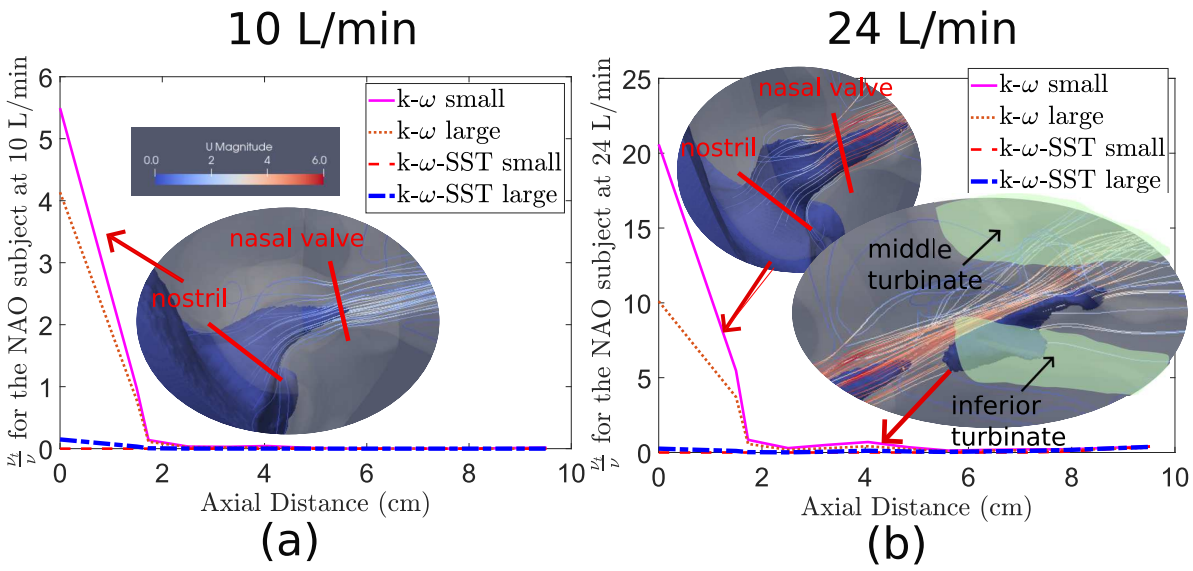


Figure 5.9: The area-averaged turbulent viscosity ratio versus the axial distance of each slice of the NAO (scan2) subject is displayed. Similar to figure 5.8, the large turbulent viscosity ratio at the nostril plane and the decreasing trend towards the posterior direction are also observed. In addition, we noticed a second peak in the turbinate region. To explain this, we draw the contour with a turbulent viscosity ratio larger than 5 and the streamlines passing through the internal nasal valve. Because of the nasal obstruction, the spreading after the nasal valve is less prominent, and flow mainly passes through the turbinate in the same direction as upstream. At the airway between the inferior and middle turbinate, where the cross-section area suddenly expands, the $k-\omega$ model indicates turbulence locally. The simulated onset of turbulence will not grow into a fully turbulent state.

pressure gradient boundary layer. It is also recognized that the $k-\omega$ model is spuriously and artificially sensitive to the free-stream conditions, which may result in an even lower turbulent mixing under higher prescribed $k$ and $\nu_t$ values. In comparison, the $k-\omega-SST$ models show no turbulence within the entire airway. However, We cannot be sure that the flow field is free of turbulence in reality. As the $k-\omega$ model is heavily used in existing literature, such as Wen et al. (2008) and Li et al. (2017), we aim to raise the attention of the artificial turbulence generated at the inlet section in nasal airway simulations. However, it is beyond the scope of the thesis to understand where the $k-\omega$ model fails.

### 5.1.5. Unilateral comparison between simulations with experiments

From the previous discussion, we have identified the nonphysical turbulence gathering in the inlet region predicted by the $k-\omega$ model, and the $k-\omega-SST$ models have shown no turbulence within the flow field. This observation motivates us to use the laminar model in the unilateral study. The static pressure drops from measurement and simulations are plotted in figure 5.10. The simulation for the right side of the unilateral airflow was not included because of the highly similar scale of the static pressure drop seen in figure 5.10 (a).

We have the following observations from figure 5.10.

On the one hand, we will describe both subjects' measured static pressure drop and the pressure-flow relation. Firstly, we noticed a similar magnitude of the pressure drop for the healthy (FD2) subject between the left and right in figure 5.10 (a). This can be explained by the symmetric geometry of the FD2 nasal airway. In comparison,

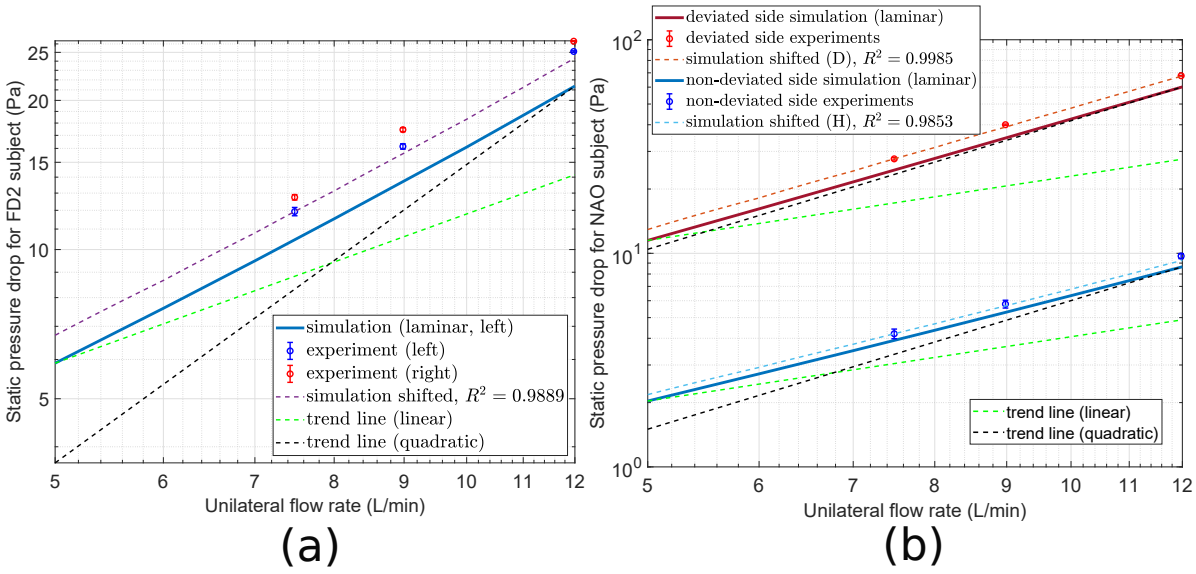


Figure 5.10: Unilateral static pressure drop measurement and its comparison with the laminar model for (a): the healthy subject (left and right), and (b): the NAO subject, both deviated side (obstructive, D) and healthy, non-deviated side (non-obstructive, H). In figure (a), we noticed a static pressure drop difference below 7% on both sides of the healthy airway, although the pressure-flow gradient seems to be slightly different. In comparison, the static pressure drop of the deviated side is approximately 6 times greater than the static pressure drop of the non-deviated side. In addition, the laminar model shows around 15% of errors for the FD2 model for measured flow rates, around 12% for the deviated side of the scan2 model, and around 8% for the non-deviated side. The shifted simulation curve shows an acceptable correlation with the experimental data, which may indicate that the gradient of pressure drop on the flow rate is also predicted well.

the magnitude of the pressure drop for both sides of the NAO (scan2) subject shows a dramatic difference. This is because the septal deviation resulted in a constriction in the nasal airway, which caused the pressure drop to increase on the deviated side. Secondly, from comparing the trend lines, we notice that the unilateral pressure drop of the deviated side of the scan2 subject shows a strong correspondence to the flow rate square. Curve-fitting also indicates the pressure drop of the scan2 deviated side fits with $0.6087Q^{1.90}$ simulated by the laminar model, compared to the FD2 ($0.5903 \times Q^{1.5329}$) and the scan2 non-deviated side ($0.1155 \times Q^{1.7845}$). The exponent of Q indicates that the airflow of the deviated side is strongly inertial dominated, in which separation and turbulence may happen. We cannot utilize the RANS models to determine precisely whether separation or turbulence exists or dominates due to their limitations.

On the other hand, we notice that the laminar model still gives a reasonable pressure drop prediction within 15% error under the studied flow rates. However, we may note that future investigations should simulate the severely deviated side to research unilateral airflow for NAO subjects using simulation setups that can better resolve the flow field, such as LES or DNS. This is because the flow may stay in a highly inertial-dominated zone, where large-scale separation and the onset of turbulence may happen.

### 5.1.6. Discussion

In this section, we thoroughly studied the pressure-flow relation modeled by various turbulence setups for bilateral and unilateral nasal airflow compared to the experiment. To understand the effectiveness of the turbulence setups, we examined (1) the value of static pressure drop and (2) the gradient in the log-log plot.

(1) From the value of the static pressure drop, the $k-\omega$ small model shows the best consistency with our measurement results. However, our simulations found that it tends to exaggerate turbulence scale at the inlet. Existing work such as Li et al. (2017) claims that the $k-\omega$ model of all the RANS models correlates the best with the experimental data for larger flow rates (33.6 L/min) in terms of the velocity profile or turbulent intensity. In light of our validation using the turbulent viscosity ratio, we suggest more caution in the future when studying nasal airflow with the $k-\omega$ model, besides its merits shown in Li et al. (2017). Other models, such as the $k-\omega-SST$ model, did not predict any existence of evident turbulence. In comparison, the laminar model shows an overall error of 15% for both unilateral and bilateral airflow for healthy and NAO subjects. This 15% error can be contributed partly by the area deviation in the 3D printed model and partly by the unsteadiness effects, which cannot be captured in steady-state simulations (will be discussed in section 5.2). Overall, we recommend using a laminar model under restful breathing.

(2) From the pressure-flow relation, we notice that the nasal airflow is transitional to an inertia-dominated zone under the studied flow rate. The nasal airflow under restful breathing rates is a combination of the laminar region, separation region, and possible onset of turbulence, which makes the flow field challenging to model accurately. Especially for higher flow rates of the unilateral study of NAO subjects, we noticed an almost quadratic behavior on the obstructive side. This quadratic behavior will not be visible in the pressure-flow relation for bilateral study because more airflow (about 76% for the scan2 patient) can be redistributed to the healthy side of the NAO subject. The flow rate passing through the obstructive side is then lower, and the quadratic behavior will not be observed bilaterally. Further investigation with LES or DNS models may resolve the flow field. However, the laminar model still shows a good prediction of the experimental data from the aspect of the static pressure drop.

## 5.2. Validation of a steady state solver

In this section, we aim to answer this question: is the steady state solver accurate enough for resolving the nasal airflow? We deem that the unsteadiness can be caused by two factors: (1) the geometry of the nasal airflow, which may lead to flow separation and other unsteady effects, and (2) the time-varying flow rate during the real-life inhaling process (if quasi-steady approximation applies). From these two factors, we built the following setups.

### 5.2.1. Setup

The first factor is discussed with a constant flow rate simulation with transient simulation (the quasi-steady simulation). Since unsteadiness is more likely to happen under large flow rates, we will use a 24 L/min flow rate in the simulation. The quasi-steady simulation will be studied using the time-averaged flow field and its standard deviation. The usage of the steady-state simulation will be examined by its comparison with the quasi-steady simulation.

The second factor is investigated through the transient simulation with a sinusoidal flow rate profile with time. As the equivalent mean flow rate is 24 L/min ($\overline{\dot{V}_i} = 24L/min$ in section 2.2) and the inspiratory time is 4 s (from section 3.2.2), we could calculate the prescribed time-varying flow rate as $\dot{V}_{sin}(t) = 37.7sin(\frac{\pi}{4}t)(L/min)$. This function indicates that the inclining phase (discussed in chapter 3) is at 0-2 s, and the declining phase is at 2-4 s. As the flow field is time-varying, we will compare the instantaneous flow field when the flow rate matches the restful breathing range.

In general, unsteady simulations require more time to complete than steady-state simulations. We might coarsen the mesh locally to increase the time step, as the time step is often chosen so that the Courant number is less than 1, which would further minimize the computing time. The final mesh (verified by the *checkMesh* utility) has a cell number of around 5.1 million. Although a turbulence model is not applied here, near-wall cells are refined to resolve the near-wall flow better. All the simulations (steady-state, quasi-steady, and breathing-cycle simulations) in this section utilized the same mesh to allow for fair comparisons.

### 5.2.2. Unsteadiness caused by the geometry

We will first examine the time-averaged and area-averaged static pressure values over the posterior slices. The static pressure is defined using the area-averaged static pressure values over the posterior slices, the same methodology as in section 4.3.1. The results are shown in figure 5.11.

From figure 5.11, we observed that (1) unsteadiness happens throughout the flow field, although the fluctuation is relatively small. This can be seen from the fact that the standard deviation of static pressure, which represents the fluctuation of the flow field, is only 3.4% of the mean pressure value. And (2) the mean static pressure value predicted by both simulations did not show a significant difference. Of all the slices in figure 5.11, the largest difference in static pressure value happens in the pharynx region, where the difference between steady-state simulation and quasi-steady simulation is around 1%.

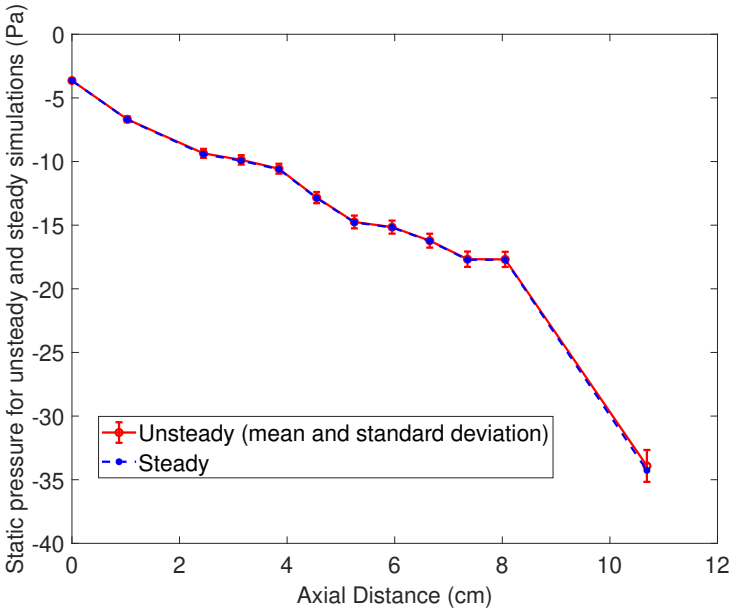


Figure 5.11: Area-averaged static pressure values over axial slices for the steady-state and the quasi-steady (mean value/standard deviation) simulation under a flow rate of 24L/min are displayed. The difference in static pressure between steady-state and mean value of quasi-steady simulation is around 1% for the pharynx slice (the last slice) and negligible (around 0.2%) for the rest. As a result of unsteadiness, the standard deviation accounts for approximately 3.4% of the static pressure value for all slices.

To better visualize the unsteadiness in the internal flow field, we selected a sagittal measurement plane that slices the anterior cavum, the middle and the inferior meatus, and the posterior part of the pharynx, as shown in figure 5.12. We subtracted the steady-state flow field from the time-averaged quasi-steady flow field, and compared the result at the sagittal measurement plane. The resulting velocity magnitude and the pressure difference are plotted in figure 5.13. A larger difference in velocity and pressure field is found in the rear side of the nasopharynx (the red-circled region in figure 5.13) compared to other places.

A possible reason for this difference concerns the unsteady effect in the nasopharynx region, which the steady-state simulation fails to capture. Because the velocity fluctuation over time can express the unsteady effect, the temporal standard deviation of the velocity field, both dimensional and non-dimensional (normalized by the local time-averaged velocity magnitude), is plotted in figure 5.14.

We can observe in figure 5.14 (a) that the red-circled region of figure 5.13 is unsteady, because $U_{stddev}$ is the highest in this region. In figure 5.14 (b), we recognized several regions with a large value of normalized standard deviation ($\frac{U_{stddev}}{U_{average}}$). These regions exist because of a locally small value in $U_{average}$ and a large value in $U_{stddev}$, which in principle should exist in the flow separation zone. The zoomed-in visualization of the streamline plots also indicates the separation flow pattern. However, comparing the separation regions in figure 5.14 (b) and these regions in figure 5.13, we should note that in these flow separation regions, the steady-state simulation shows excellent correspondence with the time-averaged quasi-steady simulation. In comparison, we noticed that the red-circled region of figure 5.13 has a smaller $\frac{U_{stddev}}{U_{average}}$ value compared

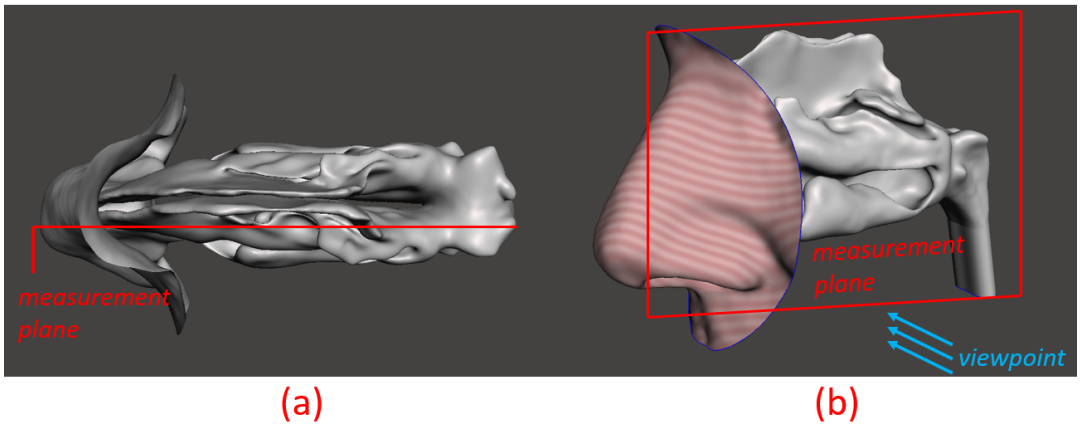


Figure 5.12: To better visualize the flow field, we selected a representative sagittal plane. The location of the measurement plane in the FD2 nasal airway is shown in figure 5.12 (a), and we will examine the flow field from the location specified in figure 5.12 (b).

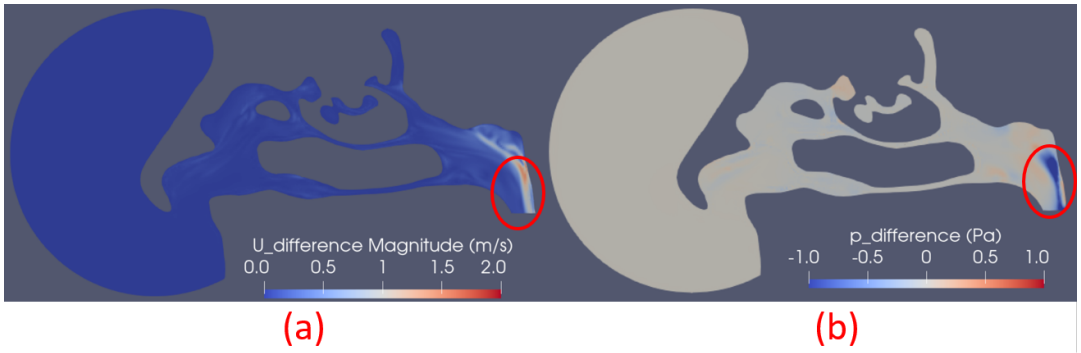


Figure 5.13: We subtracted the steady-state flow field from the time-averaged quasi-steady flow field, to study if the steady-state simulation matches the quasi-steady simulation. Both pressure (in figure 5.13 (a)) and velocity field (in figure 5.13 (b)) show a large difference in the flow field near the rear side of the nasopharynx region (the red-circled region in both figures) and a small difference in other locations, comparing these two simulations. Our focus will be to explain why a large difference happens in this region.

to the flow separation regions. This may indicate that this region is not the separation zone, where $\frac{U_{stddev}}{U_{average}}$ is usually larger.

One possible explanation of how this unsteady region is formed is the mixing effect of the airflow coming from each side of the nasal airway. We first selected two representative streamlines passing through this region to demonstrate this potential mixing effect, as seen in figure 5.15. The streamline plot shows that at the location where unsteadiness (velocity fluctuation) is the largest, the airflow from two sides of the nasal airway converges. This may indicate that the velocity fluctuation comes from the interaction between two streams of the nasal airflow from two sides of the nasal airway.

A more direct illustration can be found in figure 5.16, where we compared the bilateral simulation for a flow rate of 24 L/min and the unilateral simulation for a flow rate of 12 L/min. From this comparison, we observed that the unilateral simulation (in figure 5.16 (a)) in the unsteady region (circled-out region) shows a more uniform flow going

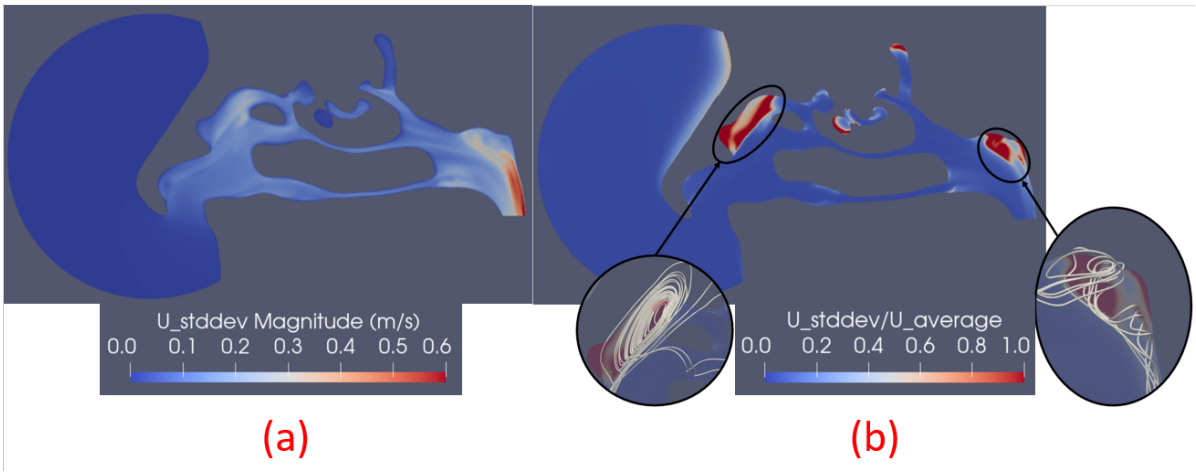


Figure 5.14: The standard deviation contour of the velocity magnitude ($U_{stddev}$) is shown in figure 5.14 (a). We also found a high standard deviation in velocity magnitude at the red-circled region of figure 5.13. In addition, the normalized temporal standard deviation contour of the velocity magnitude ($\frac{U_{stddev}}{U_{average}}$), normalized by the local velocity magnitude ($U_{average}$), is shown in figure 5.14 (b). We found that in the anterior cavum (the left circled-out region), the end of the olfactory region, the middle meatus, and the upper side of the nasopharynx (the right circled-out region), $\frac{U_{stddev}}{U_{average}} > 1$. This means that at these locations, the velocity fluctuation is higher than the mean velocity. To visualize the flow pattern at these locations, streamlines were computed through the time-averaged velocity field and plotted in the circled-out regions. At the location where the unsteady effect is the strongest, we could identify large-scale flow separation.

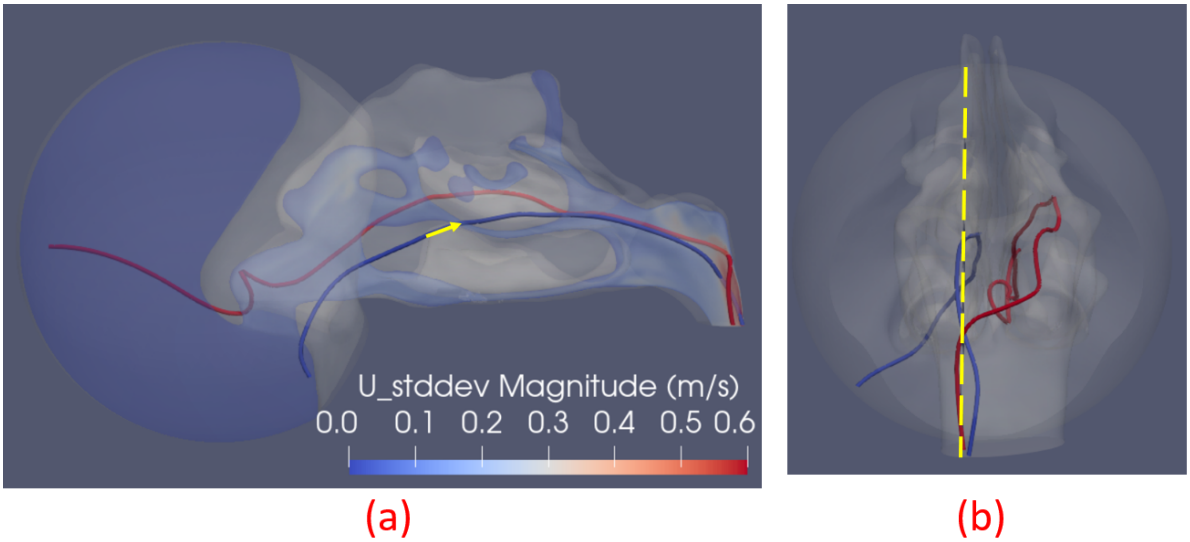


Figure 5.15: Two representative streamlines, passing through the red-circled region of figure 5.13 are plotted in figure 5.15 (a): side view, and figure 5.15 (b): rear view. The flow direction is indicated in a yellow arrow in figure 5.15 (a), and the location of the measurement plane is indicated in a yellow dash line in figure 5.15 (b). It can be seen in figure 5.15 (a) that these two streamlines pass through the rear side of the nasopharynx region, where high fluctuation in velocity appears. In figure 5.15 (b), the blue streamline represents the flow from the left airway, and the red streamline represents the flow from the right airway. As seen in figure 5.15 (b), the airflow in the high fluctuation zone in the pharynx region originates from different sides of the nasal airway.

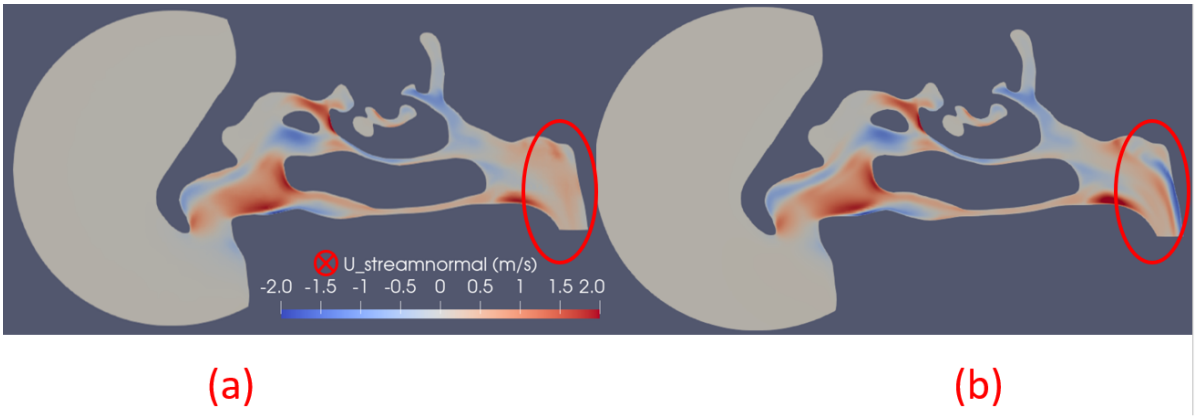


Figure 5.16: The stream-normal (normal to the mean flow direction) velocity distribution (positive direction: into the page) is plotted for (a) unilateral (flow through the left airway) and (b) bilateral airflow steady-state simulations under the same flow rates. Although the stream-normal velocity has a similar profile upstream between the two simulations, the contour differs significantly within the nasopharynx region (circled-out region). For the bilateral simulation, the unsteady region in figure 5.13 shows a high stream-normal velocity component. In comparison, the unilateral airflow mainly passes in a streamwise (mean flow) direction.

in the streamwise direction, in which case the bilateral airflow shows high variation in the stream-normal velocity. This observation contributes to the explanation that the unsteady region is caused by the joining airflow from both sides of the nasal airway. If one side of the airway is involved, the flow pattern of the red-circled region of figure 5.13 will change.

Overall, we noticed a large difference between the steady-state and time-averaged quasi-steady flow field on the rear side of the nasopharynx region. We observed that the airflow in this region is highly unsteady and is also the converging flow of two streams coming from both sides of the nasal airway. This may indicate that this large difference is caused by the unsteady effect of the joining of two streams of unilateral nasal airflow. We can possibly find the reason steady-state simulation is inaccurate in this situation from Franke et al. (1990), where they simulated flow past a square cylinder for $Re = 150$. They investigated the difference between a streamline plot from a steady-state simulation and a time-averaged streamline plot from an unsteady simulation. The resulting separation zone past the cylinder for the steady-state simulation is considerably too long. They claimed that the steady-state simulation lacks an important momentum exchange process due to the interaction of the shed vortices. In our case, the two streams from two sides of the nasal cavity combine in the red-circled region of figure 5.13, and momentum will also exchange in unsteady simulations. However, this may not be resolved in steady-state simulations.

### 5.2.3. Unsteadiness caused by time-varying flow rates

In this section, we will first discuss whether the static pressure drop is well predicted for all flow rates in the restful breathing range.

Considering the simulation time for quasi-steady simulations are generally longer, transient simulations for multiple flow rates will be too time-consuming. Also, because we have observed that the pressure values for 24 L/min match well between quasi-steady and steady-state simulations, we will only compare the breathing-cycle (both

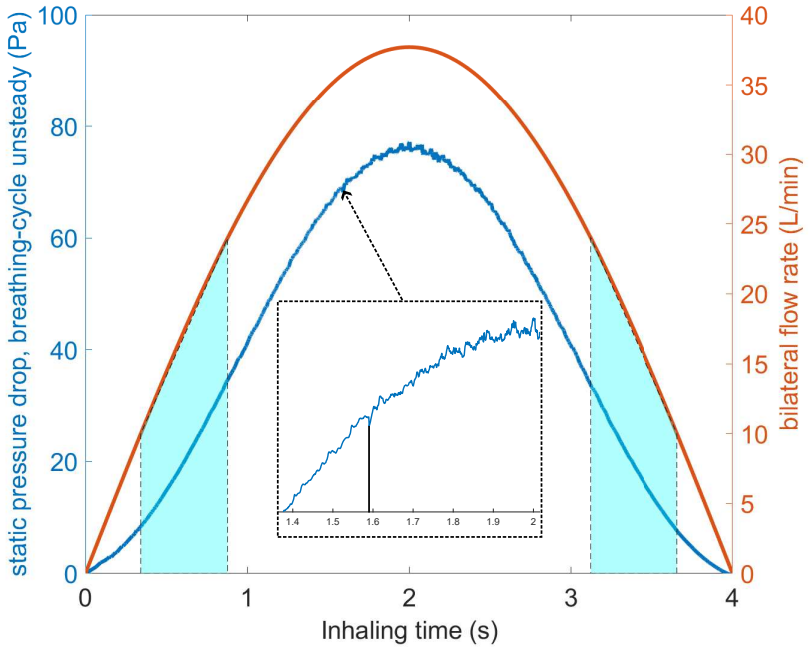


Figure 5.17: The flow rate versus inhaling time (the orange-colored curve with its axis on the right) and the overall static pressure drop versus inhaling time (the blue-colored curve with its axis on the left) for the breathing-cycle simulation are plotted. The highlighted region is the range of steady-state simulation in this study. It can be noticed that similar to the flow rate profile (the orange-colored curve), the pressure-time curve can be divided into the inclining phase and declining phase. The magnitude of oscillation seems to start growing after 1.6 s, as seen in the zoomed-in figure. However, the oscillating region is beyond the restful breathing flow rates.

phases) and the steady-state simulations. The prescribed flow rate profile at the inlet patch is visualized in figure 5.17. The maximum flow rate in breathing-cycle simulation exceeds the restful breathing flow rates in steady-state simulation. Therefore, our discussion will mainly focus on the overlapping flow rates, also covered by the steady-state simulations, as the highlighted zone in figure 5.17.

The two observations in figure 5.18 (see the caption) are potentially caused by the acceleration and deceleration of the airflow. In principle, the fluctuation decreases under lower flow rates, so it is less likely to have a large deviation in pressure drop for lower flow rates because of temporal fluctuation. As shown in figure 5.17, the flow rate changes more rapidly with time when the flow rate is lower. This acceleration in flow rate could cause an additional effect on the flow field, leading to the difference in the pressure drop of the inclining/declining phase. We may get the mathematical interpretation from the definition of *St*. As $St = \frac{2\pi f L}{U}$, for a lower flow rate, $U$ will decrease. As a result, *St* will increase, which means the unsteady effect will be dominant compared to the inertial transport. Therefore, it can be inferred that, under the same flow rate, the pressure drop will show a larger difference for lower flow rates when it changes more rapidly over time.

We will first explore the second observation in figure 5.18. Since in figure 5.18 we noticed that the pressure drop for the steady-state simulation stays in between both phases of the pressure drop for the breathing-cycle simulation, we will only select one branch of the breathing-cycle simulation for comparison. We deem that the patient is

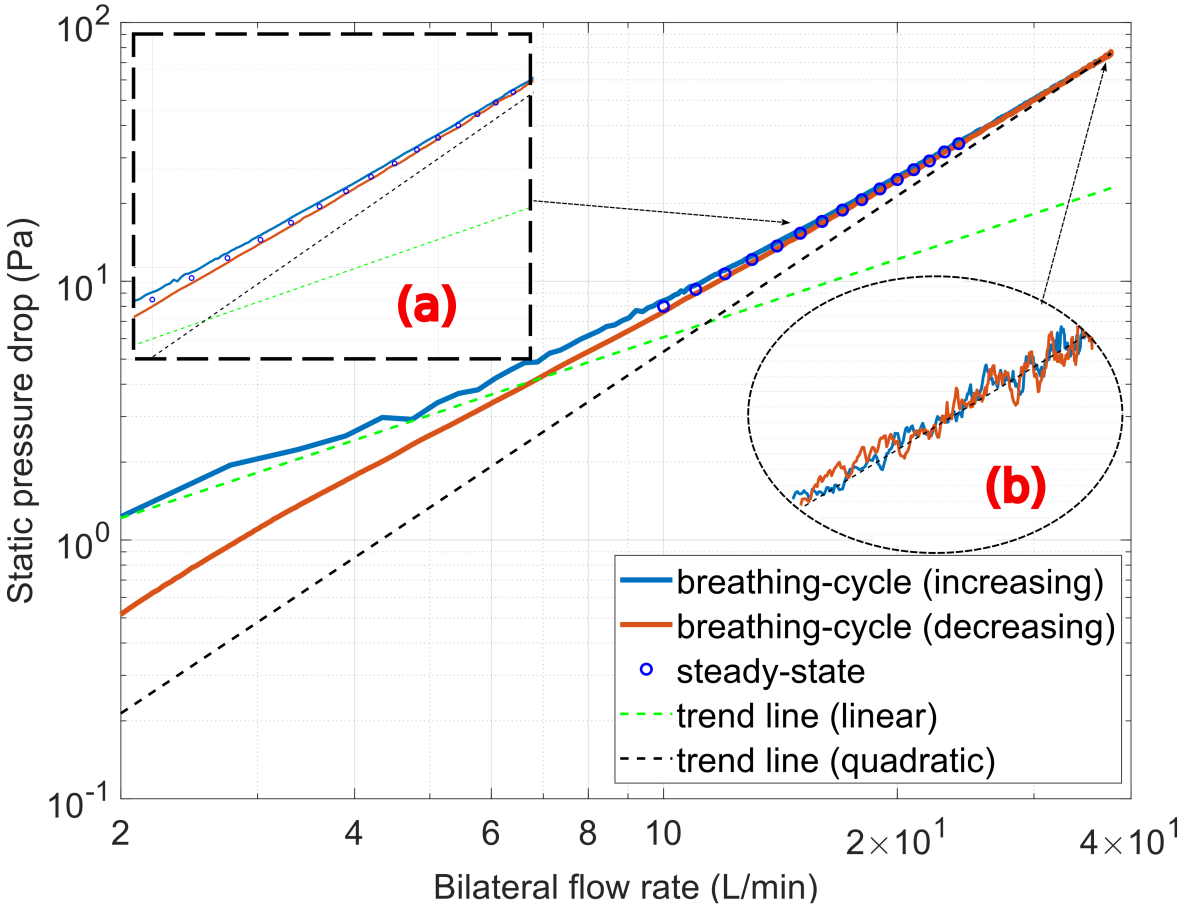


Figure 5.18: Bilateral flow rates against static pressure drop for the inclining and declining phases of the breathing-cycle simulation and the steady-state simulation are plotted on a log-log scale. In addition, the trend lines for linear and quadratic pressure-flow relations are plotted. We zoomed in on the static pressure drop for restful breathing flow rates in sub-figure (a) and the quadratic trend lines for higher flow rates in sub-figure (b). We have two observations from this figure and sub-figure (a). Firstly, we noticed that the static pressure drop curve differs in the inclining and the declining phase, which has a smaller magnitude for larger flow rates and a larger magnitude for smaller flow rates. Under the restful breathing flow rate range, this deviation is around 10% for 10 L/min and around 3% for 24 L/min, as seen in sub-figure (a). Secondly, we noticed that the pressure drop for steady-state simulation stays between the pressure drop for the inclining and declining phase of the breathing-cycle simulation. The deviation in pressure drop between steady-state and breathing-cycle (both phases) simulation is around 5% for 10 L/min and 1.5% for 24 L/min.

most likely to complain in the inclining phase of the inhaling process when the air first enters the nose. In addition, we will select the quasi-steady simulation for comparison to avoid the unsteadiness in the flow field caused by the geometry (see section 5.2.2). Therefore, we will compare the flow field for 24 L/min between quasi-steady and breathing-cycle (inclining phase) simulations by subtracting the breathing-cycle from the quasi-steady flow field. The result is shown in figure 5.19.

Next, we will explore the first observation in figure 5.18. Since the smaller flow rate corresponds with a larger pressure difference between the inclining and declining phase of the breathing-cycle simulation, we will compare the pressure difference under flow rates of 10 L/min and 24 L/min. Because we did not simulate quasi-steady cases for lower flow rates, we will show the flow field difference between steady-state simulation and breathing cycle simulation in figure 5.20. Based on figure 5.13, we should not expect too much difference between steady-state and quasi-steady simulations, except for the red-circled region.

Figure 5.20 is indicative that the increase in pressure difference in figure 5.19 is more significant for lower flow rates. It also corresponds with our observation in figure 5.18, where we found the static pressure drop predicted by steady-state simulation is less accurate (less than 5%) for lower flow rates.

There is existing literature that introduced the pressure drop difference between the inclining and declining phases of breathing cycles. Moniripiri et al. (2021) also set up a sinusoidal flow rate versus time profile with a smaller peak flow rate ($\dot{V}_{sin}(t) = 25sin(\frac{\pi}{2}t)$ and simulated the nasal airflow for a patient went through paranasal sinus surgery. They also noticed a larger pressure drop difference under lower flow rates between the inclining and declining phases of each breathing cycle, where steady-state simulations cannot predict the pressure drop accurately. However, to our best knowledge, few studies mentioned the flow field difference between the steady-state simulation and breathing-cycle simulation.

Overall, our simulation suggests that we could expect less than 5% error in static pressure drop if we use steady-state simulations under the lower flow rates of a real-life breathing cycle. Although the scale of the error corresponds with the acceleration of the inhaling flow rate, it is still yet uncertain if the flow acceleration indeed causes this error.

Aside from the main topic of this section, as an additional note to section 5.1, we also noticed that the trend line in figure 5.18 shows an approximately linear trend at a lower flow rate and a quadratic trend at a higher flow rate. The pressure-flow relation is strongly correlated with the quadratic trend at a flow rate larger than 37 L/min (see figure 5.18 (b)), with $R^2 > 0.98$. The critical flow rate for a quadratic trend is above the restful breathing flow rate range. In addition, a close-to-linear trend can be found at a flow rate lower than 4 L/min, with a linear correlation of $R^2 > 0.96$. This also contributes to the finding in section 5.1.2, that the flow is in a transition zone between the viscous and the inertial-dominated region under restful breathing.

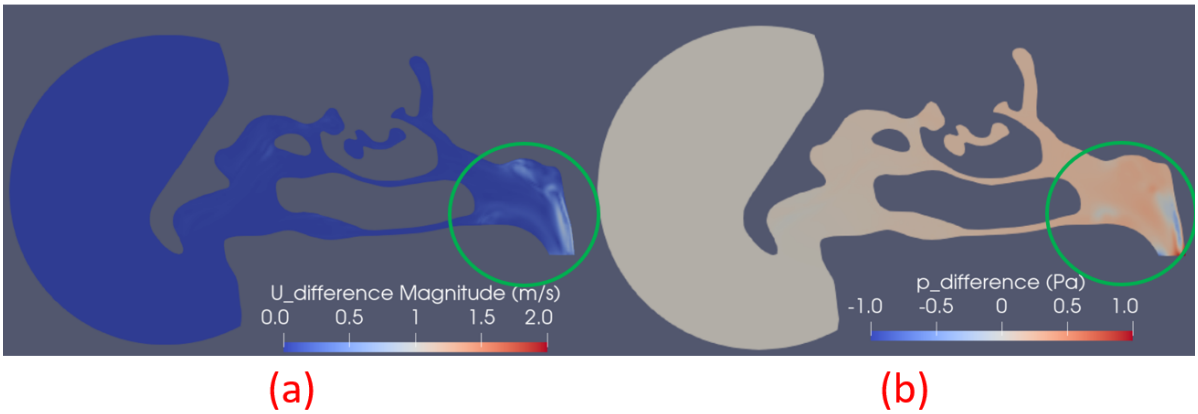


Figure 5.19: The difference in the flow field for 24 L/min between the quasi-steady and the breathing-cycle (inclining phase) simulation is studied. Both the velocity field (in figure 5.19 (a)) and pressure (in figure 5.19 (b)) are plotted. The rear side of the nasopharynx region (the red-circled region in figure 5.13) is still the main contributor to flow field difference. However, the flow field difference of this region in the current figure is not as large as in figure 5.13, presumably because both simulations are transient, which can resolve the temporal effects discussed in section 5.2.2. In addition, we found a non-local increase in pressure difference downstream (see the scale of pressure field difference in the green-circled region in this figure). The pressure field difference reached a maximum value of around 0.3 Pa (2% compared to the local pressure value) in the nasopharynx. This posterior increase in pressure difference was not noticed in figure 5.13.

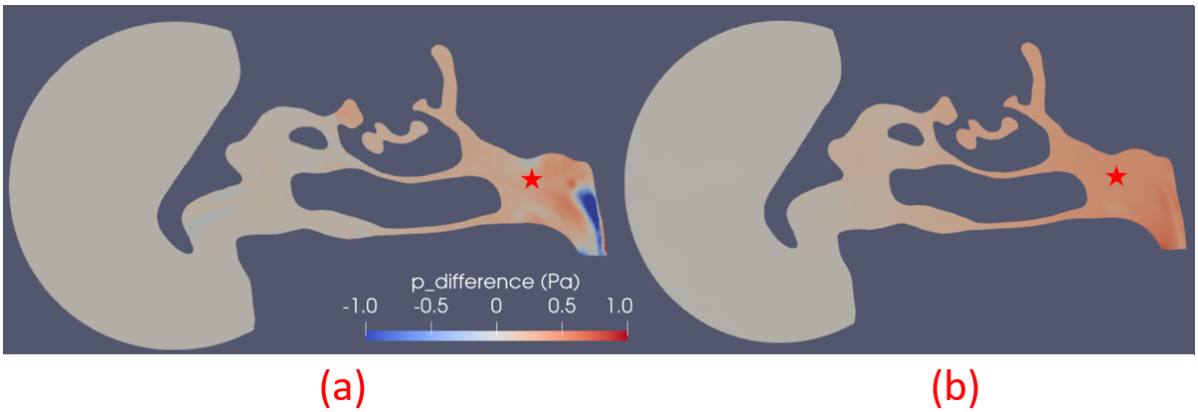


Figure 5.20: The flow field differences between steady-state simulation and breathing-cycle simulation for 24 L/min (in figure 5.20 (a)) and for 10 L/min (in figure 5.20 (b)) are plotted. Because the change in flow rate causes the static pressure value to vary, we compared the pressure value and pressure difference under different simulations at the same point (the star point in both figures) of the flow field. For 24 L/min, the pressure value is 17.6 Pa and the pressure difference for both simulations is 1.3% (0.23 Pa). For 10 L/min, the pressure value is 5.38 Pa and the pressure difference for both simulations is 7.4% (0.40 Pa).

### 5.2.4. Surface-normal velocity comparison

In the above discussions, we have noticed differences in the flow field in the nasopharynx concerning the geometry (the joining effect of two streams) and the flow rate (potential acceleration effect). Because the upstream structures are yet not quantitatively validated, we will compare the surface-normal velocity for all three simulations in the

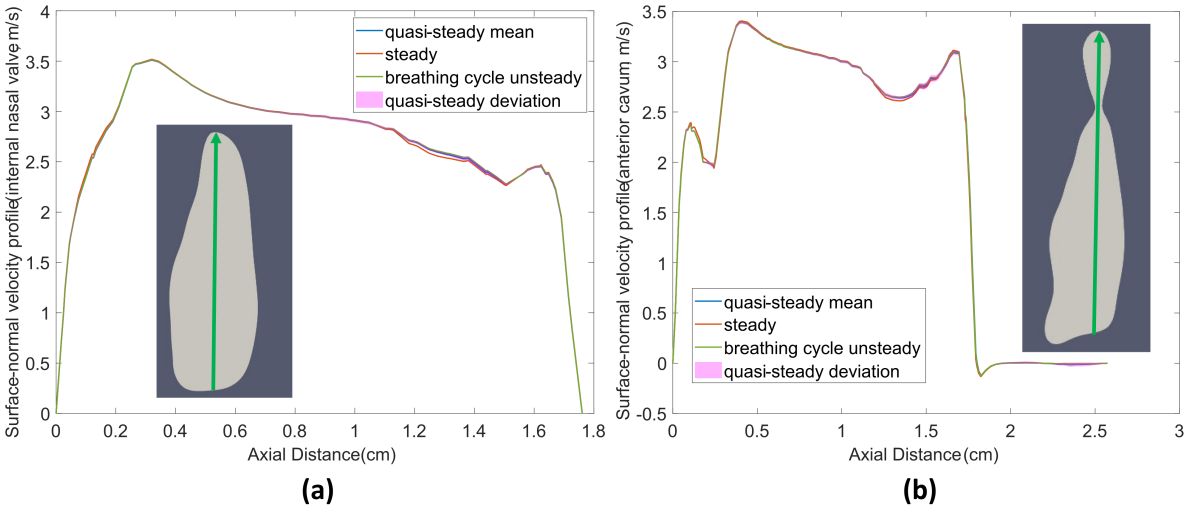


Figure 5.21: The surface-normal velocity comparison shows a minor difference among the three simulations. We observed little difference between the quasi-steady simulation and the breathing-cycle simulation. A small deviation between the steady-state simulation and the other two unsteady simulations can be observed at the axial distance of around 1.2 cm in the internal nasal valve slice, and at around 1.4 cm in the anterior cavum slice. The locations where this small deviation happens correspond to the location with more unsteadiness in quasi-steady simulation.

inflow area in figure 5.21. The definition of surface-normal velocity is the same as section 4.3.2. Two cross-sections will be involved, namely the anterior cavum slice and the internal nasal valve slice. The large recirculation zone in the anterior cavum introduced unsteadiness, as we have seen in figure 5.14, so the surface-normal velocity comparison here can indicate the effect of unsteadiness. Although we noticed no predominant unsteadiness near the nasal valve, the nasal valve slice is selected because the velocity is maximum throughout the flow field.

As seen in figure 5.21, the surface-normal velocity comparison shows almost no difference between the quasi-steady simulation and the breathing-cycle simulation. Comparing the steady-state simulation with the unsteady simulations, we noticed a minor difference in the selected two slices in the inflow area.

### 5.2.5. Computational time

The computational time required for a full-time breathing cycle, or even quasi-steady simulation determines that unsteady simulations have limited clinical applications. It takes 3 hours to finish the steady-state simulation. The transient simulation with a constant flow rate (named quasi-steady simulation) was found to fully develop after 1.2 physical seconds, and the computational time running in the 28-core Linux cluster is around 580 hours. In comparison, the transient simulation with varying flow rates (named breathing-cycle simulation) requires 2000 hours to complete.

### 5.2.6. Discussion

In this section, we compared the flow field for the steady-state simulation, the quasi-steady simulation, and the breathing-cycle simulations from two aspects: the area-averaged static pressure (drop) and the flow field difference at one certain sagittal slice. In conclusion, we recommend using steady-state simulation in the nasal airflow simulation, and the reasons are as follows.

1. Most importantly, the steady-state simulation shows an acceptable difference compared to other types of transient simulations. In section 5.2.2 and 5.2.3, we attempted to identify two sources of unsteadiness: (1) the unsteadiness caused by two streams joining at the rear side of the nasopharynx, and (2) the unsteadiness related to the time-varying flow rate, mainly affect the posterior regions (see the circled area) under lower flow rates. Although these two sources of unsteadiness can cause some deviation between the steady-state and the transient simulation results, we note that the unsteadiness will lead to limited static pressure drop. The first source of unsteadiness can cause only a difference of 1% in the mean static pressure drop, with around 3.4% standard deviation value under a constant flow rate of 24 L/min. The second source can maximally lead to a 5% difference in pressure drop under a 10 L/min flow rate in a sinusoidal flow rate-time profile.
2. As discussed in section 5.2.4, other than the nasopharynx region, the surface-normal velocity profile at specified locations shows a negligible difference for all three types of simulations.
3. As shown in section 5.2.5, the computational time for transient simulations is too long to be applied in the research with multiple cases.

To avoid this unsteadiness, one could consider limiting the region of interest upstream, for example, to the choana region. However, we note that it will give additional difficulty in experimental investigation. Because the flow is not uniform in the choana region, the experimental result can depend on the measurement position. Therefore, if the choana is selected as the measurement plane for calculating static pressure drop, the experimental design might have to measure pressure drop in multiple locations of the choana plane and calculate the average.

# 6

# Potential CFD outcome for NAO detection: case studies

## 6.1. Introduction

In this chapter, we use the validated (steady-state, laminar) configuration to attempt to detect NAO. Given the scenario in section 5.1.2 that static pressure drop in the healthy subject is higher than in the NAO subject, we deem that a criterion to detect NAO among subjects should exclude the interpersonal variation of, for example, the nasal airway volume. Alternatively, because of the symmetrical anatomy of the nasal airway of one individual, this interpersonal variation can possibly be reduced by comparing unilateral parameters of the same subject. Following this idea, in section 6.2, our attempt will be based on the unilateral (static) pressure drop ratio. However, as indicated in section 1.2.5, the nasal cycle of a healthy patient can also occur during the CT-scan procedure, which may confuse the detection of NAO symptoms. In section 6.3, we will scratch the surface of the nasal cycle effect on NAO detection by presenting the unilateral pressure drop ratio of one patient with an apparent nasal cycle.

## 6.2. Unilateral pressure drop ratio

Our research in section 5.1.5 (see figure 5.10) revealed that the scan2 (NAO) subject has a different unilateral pressure drop over the deviated side compared to the non-deviated side, but the FD2 (healthy) subject has a comparable pressure drop over either side. We will extend the investigation of the pressure drop with two more subjects. One is a healthy subject named FD4, and the other is an NAO subject suffering from septal deviation, named scan2018. We simulated the unilateral pressure drop and plotted the resulting ratio in figure 6.1. Note that the unilateral pressure drop ratio for the NAO subjects is calculated as the pressure drop over the deviated side to the pressure drop over the non-deviated side. The unilateral pressure drop ratio for the healthy subjects is calculated as the left to the right side.

Compared to the scan2 subject, the smaller pressure drop ratio of the scan2018 subject in figure 6.1 can be explained by visualizing the flow pattern as in figure 6.2. Figure 6.2 (a) shows the streamlines of the scan2018 subject, where we can still see the inspiratory jet effect, that the airflow passing through the nasal valve spreads throughout the entire nasal airway. The septal deviation affects the flow downstream

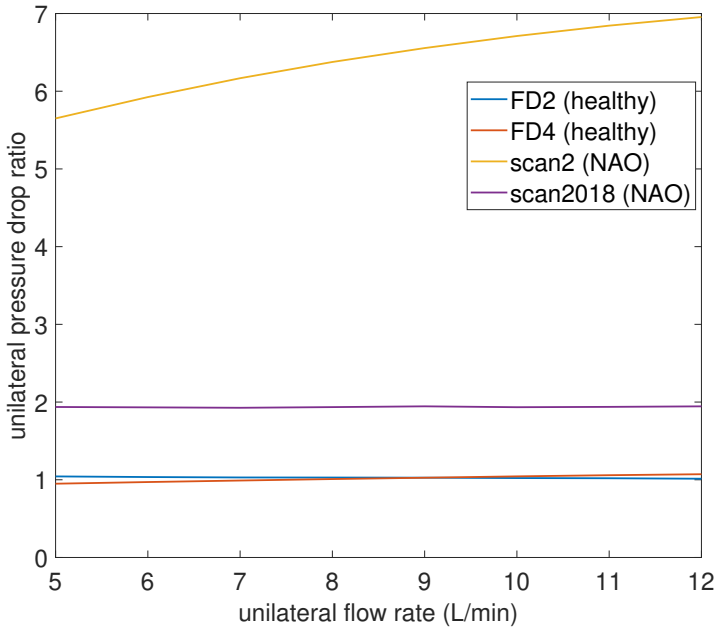


Figure 6.1: The ratio of unilateral static pressure drop for the studied four subjects is plotted. The static pressure drop ratio is uniform in both healthy persons. In contrast, both NAO subjects show a static pressure drop ratio larger than one. Specifically, the scan2 subject shows a significantly (around 5 to 6 times) higher pressure drop ratio than the healthy subjects. The scan2018 subject shows twice the pressure drop ratio of the healthy subjects.

of the nasal valve in the circled area, where we notice a “flow past blunt body” pattern forming. The location of the symptomatic structure (the circled area in figure 6.2) is shown in the CT scan in figure 6.2 (b). The deviated nasal septum blocks the air passage locally at the cross-hair marked area. Therefore, the flow is deflected by the deviated nasal septum. Compared to the scan2018 subject, the deviated septum of the scan2 subject causes the area of the internal nasal valve to shrink and changes the flow pattern completely. As shown in figure 6.2 (c), the deviated septum causes a narrower internal nasal valve, which compresses the inspiratory jet. The contraction in the internal nasal valve results in two massive recirculation zones downstream (the yellow-shaded zone in figure 6.2) and a high-velocity mean flow over a certain area between the two yellow-shaded zones in figure 6.2. The recirculation in the anterior cavum is also noticed in other healthy subjects, as we have introduced in section 4.3.1. However, this recirculation zone in the scan2 subject, originating from the internal nasal valve to the superior meatus, is significantly larger than for the healthy subjects. The high-velocity mean flow causes the static pressure to decrease compared to the healthy side, thus will be reflected in a higher magnitude of the unilateral pressure drop ratio than the scan2018 subject.

## 6.3. The confounding effect of nasal cycle

Only one individual (FD6) has an evident nasal cycle out of all the available subjects. The FD6 subject, reporting the sense-of-smell loss, shows a decongesting state in the left and congesting state in the right airway. We report that the pressure drop value on the congestion side is significantly higher than on the decongestion side.

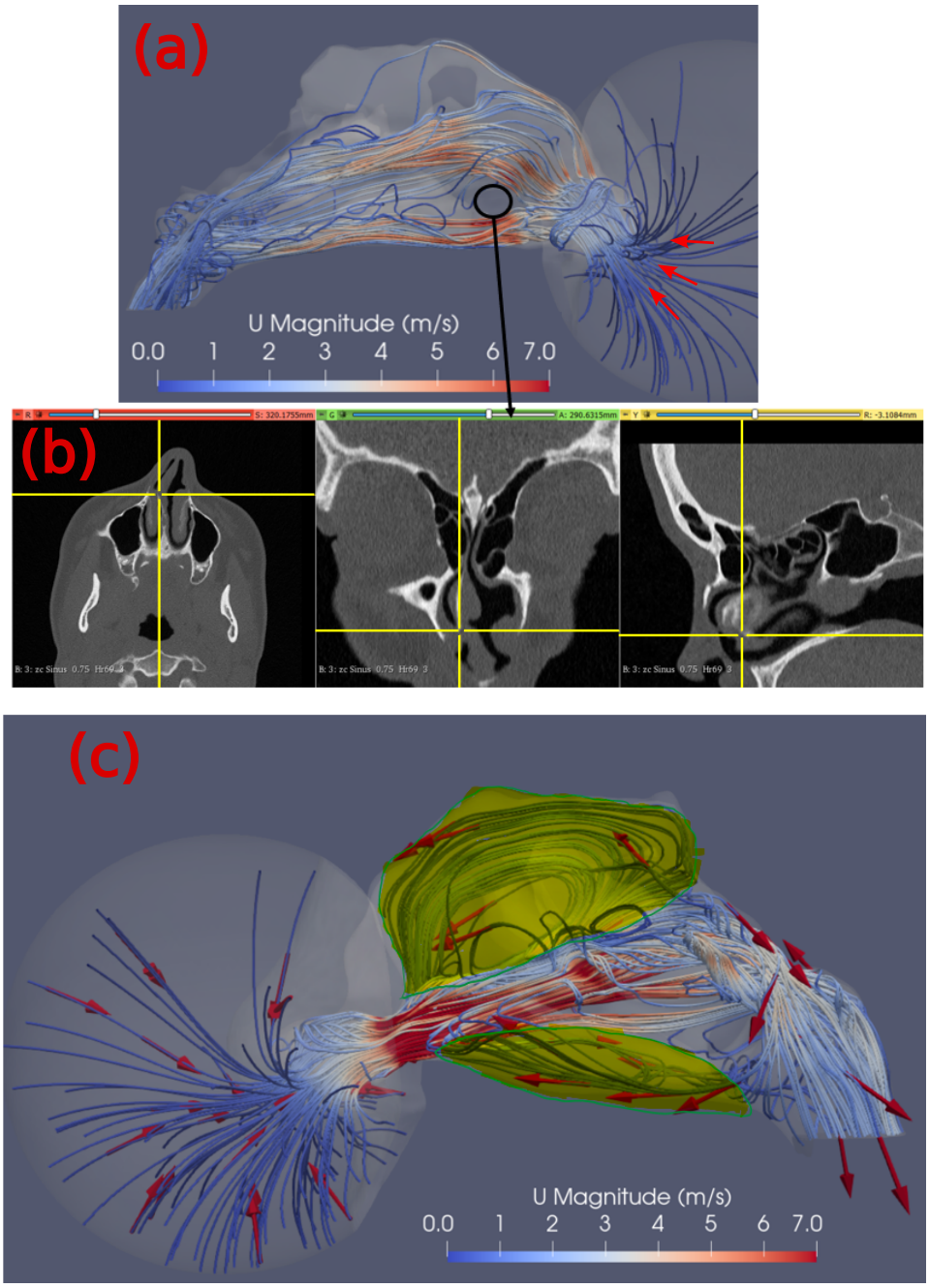


Figure 6.2: To visualize the flow pattern of both NAO subjects, we plotted the streamlines passing through the internal nasal valve for (a) scan2018 subject and (b) scan2 subject. The color of the streamline plot represents the velocity magnitude. In figure 6.2 (a), we showed the right (obstructive) side of the scan2018 nasal airway. The red arrow indicates the flow goes from right to left. We see a "flow past blunt body pattern" in the anterior cavum region, which is not seen in other subjects. The anatomy can explain the reason, as shown in the CT scan image of figure 6.2 (b). The crosshair represents the location of a deviated septum, which blocked the airway in the anterior cavum. Therefore, the airflow is deflected by the blockage. In figure 6.2 (c), we showed the left (obstructive) side of the scan2 airway. The red arrows represent the direction of velocity vectors, which indicate that the flow goes from left to right. We noticed a different "inspiratory jet" flow pattern passing the internal nasal valve compared to figure 6.2 (a) because the deviated septum reduces the area of the internal nasal valve. In addition, two large recirculation zones form downstream in the upper and lower nasal airway.

The unilateral pressure drop and its ratio are plotted in figure 6.3.

The different scales of pressure drop could indicate that the nasal cycle subject may only breathe through the decongested side. As for the comparison of unilateral pressure drop, the nasal cycle could also lead to a unilateral pressure drop ratio larger than uniform. One could argue that the ratio is significantly larger than the range displayed by the four subjects in section 6.2. However, when we consider a subject experiencing the nasal cycle but not at the peak (less congestion and decongestion than the FD6 subject), the unilateral pressure drop ratio can also decrease to a similar magnitude as for the NAO subjects. Overall, the nasal cycle effect can complicate the analysis of the unilateral pressure drop ratio.

## 6.4. Discussion

In this section, we test the usage of the unilateral pressure drop ratio as a potential CFD outcome for NAO detection. We record that the unilateral pressure drop ratio scale shows a difference between 2 healthy and 2 NAO subjects. It has the following two advantages:

1. Unilateral pressure drop ratio requires less effort to obtain. The nasal airflow has a complicated geometry that varies considerably among individuals. In a statistical study with multiple subjects involved, locating nasal structures in each nasal airway could be highly time-consuming. For the benefit of the statistical study, or eventually NAO detection in clinical applications, an important feature is its simplicity to post-process. Obtaining the unilateral pressure drop requires only one additional step in making the unilateral airway model, without extra time to distinguish individual nasal structures.

2. The accuracy of unilateral pressure drop predicted by CFD is thoroughly discussed in this study. Specifically, the usage of laminar and steady-state simulation to obtain static pressure drop is validated in section 5.1.5 and section 5.2 respectively.

However, there is also space for future study:

1. The result is not statistically sufficient to obtain any conclusive statement. Therefore, we encourage further research to study the unilateral pressure drop ratio with more datasets. In addition, increasing the flow rate did not alter the high uniform pressure drop ratio for NAO subjects. Hence, fewer samples of flow rates can be involved in a statistical study.

2. The nasal cycle could also practically lead to an obstructive sensation for a healthy subject and confound the NAO detection. We recorded a test simulation with a nasal cycle subject and noted the possible confounding effect in future studies. One potential remedy, as suggested by Wong et al. (2021), is that decongestants can be applied to the subject prior to clinical imaging to avoid the nasal cycle effect. We encourage obtrusive studies in the future to consider applying decongestants to test subjects.

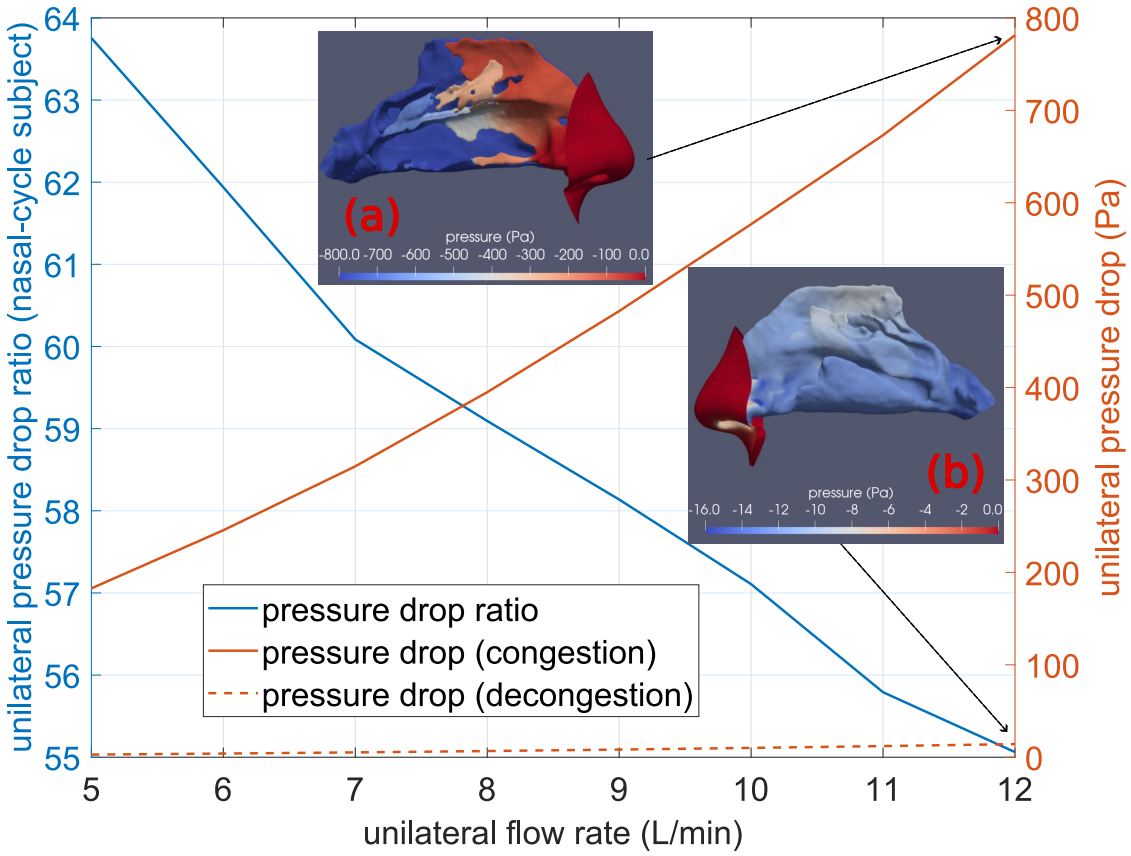


Figure 6.3: The unilateral pressure drop ratio (blue line plotted on the left y-axis) for all the studied flow rates has a significantly larger magnitude than all the simulated cases in figure 6.1. The unilateral pressure drop value (orange lines plotted on the right y-axis) indicates that the pressure drop on the congestion side (orange straight line) is an order of magnitude higher than on the decongestion side (orange dash line). The reason can be found by visualizing the pressure contour (12 L/min) on both sides. On the congestion side (see sub-figure (a)), the nasal airway in the turbinate region is narrowed because of the congested nasal turbinates. The clear air passage is mainly through the middle meatus, and the passage in other locations is highly constricted, where a strong pressure gradient exists. In comparison, on the decongestion side, as seen in sub-figure (b), the nasal airway is less constricted, and the pressure gradually decreases downstream with a less strong gradient.

# 7

# Conclusions and recommendations

## 7.1. Conclusions of this study

In this study, we have discussed the robustness and accuracy of the CFD simulations of the nasal airway. Specifically, the following aspects are considered.

1. The limitations of current techniques and the motivation of using CFD to detect nasal airway obstruction (NAO) are explained.
2. An open-source workflow to set up CFD simulations from clinical imaging is presented. Technical details to reconstruct nasal airways from CT scans and the simulation setup are introduced.
3. 2 healthy subjects (FD2, FD4), 2 NAO (scan2, scan2018) subjects, and one subject with apparent nasal cycle (FD6) are reconstructed from CT scans. In addition, the possibility of reconstruction from cone-beam CT scans, a more clinically accessible imaging technique, has been explored.
4. **Verification:** Firstly, convergence criterion setup and grid size selection were examined with a healthy subject. Additional comments on the robustness and the simulation speed are made. Secondly, the effect of boundary profiles, namely the commonly-used plane-truncated profile, an artificially modeled hemisphere inlet profile, and the external-nose incorporated profile, on the inlet velocity profile and the downstream airflow is studied with a healthy subject. The benefit of the external nose airway on the static and the total pressure is discussed.
5. **Validation:** The validation mainly concerns the laminar and steady-state setups in simulations. In the case of validating the laminar setup, the nasal airway models of a healthy subject and an NAO subject are designed and 3D-printed. The overall static pressure drop of nasal airway models is measured. Both subjects are also simulated with the laminar model and different turbulence models ($k-\omega$ and $k-\omega-SST$ models). We further examined and compared the resulting flow field using various RANS setups. The selection of laminar simulations for both bilateral and unilateral nasal airflow is justified by comparing the simulation and the experimental result. In the case of validating the steady-state simulations, we aim to validate two types of unsteady effects. The first type of unsteady effect is the unsteadiness caused by the geometry, which can be validated from the comparison between the steady-state simulation and transient simulation with a constant

flow rate. The second type is the unsteadiness caused by the time variation of the flow rate in the real-life breathing profile, which is validated by comparing the steady-state simulations and transient simulations for a sinusoidal flow rate-time profile. This flow rate profile is deemed to represent the real-life inhaling flow.

6. Finally, with the validated simulation setup to predict pressure drop, we explored the possibility of using unilateral pressure drop ratio as an NAO indicator.

The main findings are:
**Verification**:

1. The convergence criteria of $1 \times 10^{-4}$, commonly used by many researchers, are justified to be sufficient for pressure field calculations using *OpenFOAM* software. In addition, we found an acceptable difference in the static pressure drop calculation if the convergence criteria are increased to $1 \times 10^{-3}$, which may benefit a faster computation for clinical applications.

2. The boundary configuration was shown to have an impact on the inlet flow profile and direction, and eventually, the pressure drop (both static and total pressure, by around 4%). However, its effect on the flow field decreases downstream. Incorporating the external nose is recommended, although more operations are required to reconstruct the airway model.

3. To generate a shape-preserving computational mesh for the nasal airway using both tested mesh-generation libraries (*snappyHexMesh* and *CFMESH*) can require parameter-tuning and hence be time-consuming. Regarding the mesh generation setup, we recommend using *CFMESH* with a cell size length of 0.6 mm because of simplicity and mesh dependency.

**Validation**:

1. Under restful respiratory flow rates, the bilateral and unilateral static pressure drop predicted by the laminar model gives a fair approximation, with an error of less than 15% compared to the experimental results. The growth rate of static pressure drop with flow rates predicted by the laminar model also matches well with the experiments. In addition, we emphasize the caution of applying the $k-\omega$ model in the nasal airflow simulations because of the unphysical turbulence in the inlet section.

2. We observed two sorts of unsteadiness effects in the nasal airflow. The first unsteady effect mainly happens on the rear side of the nasopharynx region, where two streams from each side of the nasal airway were found to be joining. This unsteadiness may correspond to the mixing effect because of the two mixing flows. The second unsteady effect mainly happens for lower flow rates. Under lower flow rates, the flow rate increases larger with time. For this reason, unsteadiness may occur because of the acceleration/deceleration effect of the airflow. However, the usage of steady-state simulation is still recommended because of the following reasons. (1) the flow field apart from the unsteady region can still be well predicted by steady-state simulations. (2) In terms of the static pressure drop, the steady-state simulation can perfectly approximate the nasal airflow under a constant flow rate, with a variation of around 1% in pressure drop. Furthermore, the

steady-state simulation can also give an acceptable prediction for the nasal airflow for time-varying flow rates with a sinusoidal profile, with a maximum error of approximately 10% in pressure drop.

3. The above two statements prove that steady-state laminar CFD simulations show a satisfying prediction of pressure-related quantities, both bilateral and unilateral, under restful breathing conditions.

**Application**:

1. With the validated simulation setup, the unilateral pressure drop ratio is found to be around 1 for healthy subjects and larger than 1 for NAO subjects. A value of unilateral pressure drop ratio deviating from 1 may be a potential NAO detection criterion that can be found using CFD. However, we also noticed the possibility for the nasal cycle effect to be a confounding factor.

The findings of this thesis provided an estimation of the robustness and accuracy of the CFD simulations of the nasal airway from the aspect of pressure drop prediction. It mainly contributes to the application of CFD analysis in detecting NAO and can be extended into a guideline for multiple case studies and utilized in studies to analyze the potential outcome of the CFD analysis statistically.

## 7.2. Future improvement

There are a number of topics as follows that we did not address in this study because of time constraints.

1. Choosing the optimal threshold for clinical imaging segmentation is essential for the accuracy of CFD analysis in nasal airflow, as it will alter the volume and the shape of the nasal airway. However, there is currently no firm guideline on the selection of the segmentation threshold. We call for more attention to this matter.

2. Due to the limitation of eddy viscosity models, the onset of turbulence cannot be captured under higher flow rates. In the course of time, more accurate simulations (such as DNS) can be applied to detect whether there exists turbulence in the flow field. In addition, existing research has shown the possibility of conducting PIV experiments to visualize the flow field, which may also benefit understanding the detailed nasal airflow.

3. Our recommendation on the steady-state simulation for nasal airflow is based on the study of a healthy subject. Because NAO nasal airflow may have different flow patterns than the healthy subjects, the unsteadiness of NAO patients' nasal airflow may also be investigated in future studies. In addition, we choose one sinusoidal flow rate profile for the transient versus steady-state comparison in this thesis. More flow rate versus time profiles can be tested in future studies.

4. Regarding the potential NAO indicator, we encourage more investigation on the usage of unilateral pressure drop ratio. Besides, most current studies correlating CFD variables with subjective measurements use the steady-state simulation for lower time costs. According to our results in section 5.2.3, we wonder if correction for the pressure drop in the time-varying flow of a real breathing cycle is required.

# A

# Non-dimensional pressure-flow relationship

Many existing works of literature on nasal airflow defined a dimensionless pressure-flow relation. For example, in Zamankhan et al. (2006), the non-dimensional pressure (friction factor $f$) is calculated by $\mathrm{f} = \frac{\Delta \mathrm{p}/\rho}{(\mathrm{L}/\mathrm{d_h})\mathrm{u_m^2}/2}$, where $\Delta \mathrm{p}$ is the pressure drop, $\mathrm{L}$ is the length of the nasal airway, $\mathrm{d_h}$ is the hydrodynamic diameter of the cross-section at the nostrils, and $\mathrm{u_m}$ is the velocity at the nostrils. The non-dimensional flow rate is calculated as $Re = \frac{\mathrm{u_m d_h}}{v}$.

Non-dimensionalization of the pressure-flow relationship may be useful when the geometry has only one characteristic length. However, when the geometry has multiple relevant characteristic lengths, the non-dimensionalized pressure-flow relationship can be location-dependent. We take the healthy (FD2) subject as an example. In the geometry of the healthy (FD2) nasal airway, because of the narrow nasopharynx of the subject, two characteristic length scales can be distinguished. The first length scale can be defined at the internal nasal valve, and the second length scale can be defined at the pharynx. In this appendix, as obtained by our experiments, we use the total pressure drop and the flow rate data from section 5.1.2. Since we only measured the static pressure drop ($\Delta p$) in the experiments, we calculate the total pressure drop ($\Delta p_{tot}$) for our experimental data as $\Delta p_{tot} = \Delta p_{st} + 0.5\rho(\frac{Q}{A})^2$. Here, $Q$ is the flow rate, and $A$ is the pharynx slice area. The respective friction factor, and Reynolds number using the same formulation as Zamankhan et al. (2006), were plotted in figure A.1.

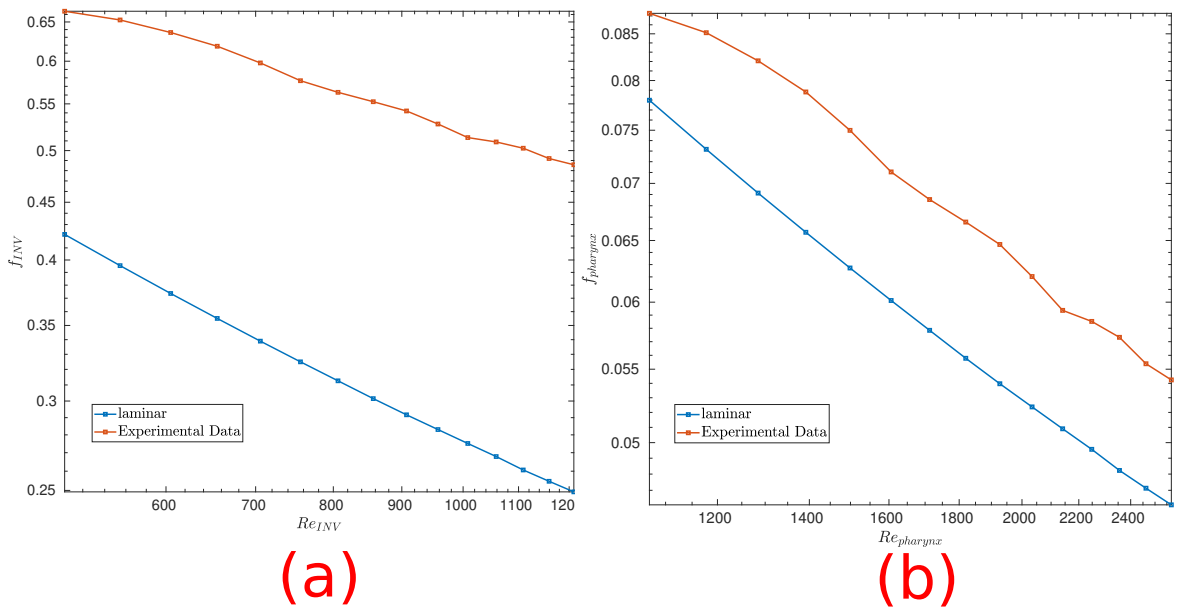


Figure A.1: Non-dimensionalized pressure-flow relationships (friction factor, $f$ versus Reynolds number, $Re$) at the internal nasal valve and at the pharynx slice are plotted in figure A.1 (a) and (b) respectively. In figure A.1 (a), We noticed that the friction factor calculated at the internal nasal valve using the experimental data is around 2 times the friction factor calculated from the laminar simulation. In comparison, the friction factor calculated at the pharynx slice using the experimental data is only 15% larger than the friction factor calculated from the laminar simulation in figure A.1 (b).

The difference in the $f - Re$ curves (in figure A.1) calculated by different positions is presumably caused by the difference in velocity. Only one side of the nasal airflow goes through the internal nasal valve on each side, and two sides of the nasal airflow go through the pharynx slice. This will cause the velocity to double. From the difference in the $f - Re$ curve calculated at different locations, we might notice that the non-dimensionalization will be location-dependent. For this reason, we did not non-dimensionalize the pressure-flow relationship in section 5.1.

# B

# RANS equations

## B.1. $k-\omega$ model

The $k$ (turbulent kinetic energy) equation can be written as:

$$\frac{\partial k}{\partial t}+\langle u_j\rangle\frac{\partial k}{\partial x_j}=\tau_{ij}\frac{\partial\langle u_i\rangle}{\partial x_j}+\frac{\partial}{\partial x_j}\left(\left[\nu+\frac{\nu_t}{\sigma_k}\right]\frac{\partial k}{\partial x_j}\right)-C_\mu k\omega \tag{B.1}$$

and the $\omega$ (turbulence specific dissipation rate) equation can be written as:

$$\frac{\partial \omega}{\partial t}+\langle u_j\rangle\frac{\partial \omega}{\partial x_j}=\alpha\frac{\omega}{k}\tau_{ij}\frac{\partial\langle u_i\rangle}{\partial x_j}+\frac{\partial}{\partial x_j}\left(\left[\nu+\frac{\nu_t}{\sigma_\omega}\right]\frac{\partial \omega}{\partial x_j}\right)-\beta\omega^2 \tag{B.2}$$

In this equation, $\tau_{ij}=\nu_T.\frac{\partial\langle u_i\rangle}{\partial x_j}$ is the Reynolds stress, $\alpha=0.52$, $\beta=0.072$, $\sigma_k=\sigma_\omega=2$ are the turbulent Prandtl numbers for each equation, $C_\mu=0.09$

Here $k$ and $\omega$ can be converted through $\nu_t=\frac{k}{\omega}$.

## B.2. $k-\omega-SST$ model

The $k$ (turbulent kinetic energy) equation can be written as:

$$\frac{\partial k}{\partial t}+\langle u_j\rangle\frac{\partial k}{\partial x_j}=\widetilde{P}_k+\frac{\partial}{\partial x_j}\left(\left[\nu+\frac{\nu_t}{\sigma_k}\right]\frac{\partial k}{\partial x_j}\right)-C_\mu k\omega \tag{B.3}$$

Here, $\widetilde{P}_k=min(\tau_{ij}\frac{\partial\langle u_i\rangle}{\partial x_j},10C_\mu k\omega)$ is the limited production in the $k-\omega-SST$ model, which prevents excessive turbulence production near the stagnation points.

and the $\omega$ (turbulence specific dissipation rate) equation can be written as:

$$\frac{\partial \omega}{\partial t}+\langle u_j\rangle\frac{\partial \omega}{\partial x_j}=\alpha(\frac{\partial\langle u_i\rangle}{\partial x_j})^2+\frac{\partial}{\partial x_j}\left(\left[\nu+\frac{\nu_t}{\sigma_\omega}\right]\frac{\partial \omega}{\partial x_j}\right)-\beta\omega^2+(1-F_1)\,2\rho\sigma_{\omega2}\frac{1}{\omega}\frac{\partial k}{\partial x_j}\frac{\partial \omega}{\partial x_j} \tag{B.4}$$

One feature of the $k-\omega-SST$ model is the usage of blending functions $F_1$ and $F_2$. This blending function switches from the $k-\omega$ model near the wall to the $k-\epsilon$ model near the free stream. The parameters in equation B.3 and B.4 are also blended:

$$\varphi=F_1\varphi_1+(1-F_1)\,\varphi_2, \tag{B.5}$$

where $\varphi \in \{\sigma_k, \sigma_\omega, \alpha, \beta\}$, $\varphi_1$ is the parameters from the $k-\omega$ model, and $\varphi_2$ is the parameters from the $k-\epsilon$ model. The value of the $\varphi_1$ parameters in the $k-\omega-SST$ models is also slightly different from the value of the parameters in the $k-\omega$ model.

$$\begin{aligned} \sigma_{\mathrm{k1}} = 1.176, \sigma_{\omega 1} = 2.000, \quad \alpha_1 = 0.5532, \beta_1 = 0.0750, \mathrm{c}_1 = 10 \\ \sigma_{\mathrm{k2}} = 1.000, \sigma_{\omega 2} = 1.168, \quad \alpha_2 = 0.4403, \beta_2 = 0.0828, \end{aligned} \tag{B.6}$$

and $C_\mu = 0.09$ has the same value for both models.

In equation B.5, the first blending function $F_1$ is calculated as:

$$F_1 = \tanh\left(\arg_1^4\right) \tag{B.7}$$

$$\arg_1 = \min\left(\max\left(\frac{\sqrt{k}}{C_{mu}\omega y}, \frac{500\nu}{y^2\omega}\right), \frac{4\rho\sigma_{\omega 2}k}{CD_{k\omega}y^2}\right) \tag{B.8}$$

$$CD_{k\omega} = \max\left(2\rho\sigma_{\omega 2}\frac{1}{\omega}\frac{\partial k}{\partial x_j}\frac{\partial \omega}{\partial x_j}, 1.0e^{-10}\right) \tag{B.9}$$

where $y$ is the distance to the nearest wall.

The turbulent viscosity is calculated as:

$$\mu_t = \rho\frac{a_1 k}{\max\left(a_1\omega; S \cdot F_2\right)} \tag{B.10}$$

where $S = \|\frac{\partial\langle u_i\rangle}{\partial x_j}\|_{,1}$ is the absolute value of the strain rate, $a_1 = 0.31$, and $F_2$ is the second blending function. It is calculated as:

$$F_2 = \tanh\left(\arg_2^2\right) \tag{B.11}$$

$$\arg_2 = \max\left(2\frac{\sqrt{k}}{C_{mu}\omega y}, \frac{500\nu}{y^2\omega}\right) \tag{B.12}$$

## B.3. Wall modeling

In this study, we selected the wall functions for $k$ and $\nu_t$ with low Reynolds number corrections.

For the wall functions for $k$, *OpenFOAM* calculates the $k$ at the wall in two different approaches under different situations.

$$k = \left(\frac{C_k}{\kappa} \times \log\left(y^+\right) + B_k\right)u_\tau^2 \quad \text{if} \quad y^+ > y^+_{\text{intersection}} \tag{B.13}$$

$$k = \left(\frac{2400}{C_{eps2}^2} \times C_f\right)u_\tau^2 \quad \text{if} \quad y^+ <= y^+_{\text{intersection}} \tag{B.14}$$

where $y^+_{\text{intersection}}$ is the $y^+$ value at the location where viscous and inertial sublayer intersects. $C_f$ is calculated as $C_f = \left[\frac{1}{(y^+ + C)^2} + \frac{2y^+}{C^3} - \frac{1}{C^2}\right]$, and $u_\tau$ is calculated as $u_\tau = C_\mu^{1/4}\sqrt{k}$.

The constants $\kappa = 0.41$, $C_{eps2} = 1.9$, $C_k = -0.416$, $B_k = 8.366$ and $C = 11$. The resulting $k$ value is always infinitesimal (lower than $10^-8$).

For the wall function $\nu_t$, the turbulent viscosity near the wall is set to be zero.

The wall function $\omega$ also calculates $\omega$ in different approaches depending on the location of the boundary cell.

$$\omega = \frac{k^{1/2}}{C_\mu^{1/4}\kappa y} \quad \text{if} \quad y^+ > y^+_{\text{intersection}} \tag{B.15}$$

$$\omega = \frac{6.0\nu}{\beta_1 y^2} \quad \text{if} \quad y^+ < y^+_{\text{intersection}} \tag{B.16}$$

Here, $\beta_1 = 0.075$. In this study, $y^+ < 5$ always applies, and equation B.16 is used as the wall function for $\omega$.

## B.4. Calculation of boundary conditions for the ”inlet” patch

In this study, we specified the turbulent viscosity ratio $\frac{\nu_t}{\nu}$ and the turbulent intensity $\frac{U'}{U}$. Here, we need to define $U$ (the velocity scale) within a specific area, calculated by the local cross-section area and the flow rate passing through the area. For bilateral simulations, the flow rate passing through each side of the nose differs. If this area has a different scale for each side of the nasal airflow, then $U$ will also differ for each side of the nasal airflow. However, the inlet boundary condition for turbulent quantities is prescribed externally as a uniform quantity for both sides of the nasal airflow. For this reason, we approximated the flow rate ratio of each side of the nose by the cross-section area ratio of the unilateral location.

For example, if $U$ is calculated at the internal nasal valve, then the flow rate on the left is calculated as $Q_L = \frac{A_{INV,L}Q}{A_{INV,L}+A_{INV,R}}$. The velocity scale on the left side $U_L$ is calculated as $U_L = \frac{Q_L}{A_{INV,L}} = \frac{Q}{A_{INV,L}+A_{INV,R}}$.

After obtaining $U$ with the specified flow rate and the specified location, $U'$ can be calculated with the specified turbulent intensity. Then $k$ is calculated by definition as

$$k = \frac{3}{2}(U')^2. \tag{B.17}$$

$\nu_t$ can be directly obtained from the specified turbulent viscosity ratio.

Finally, $\omega$ can be calculated from

$$\omega = \frac{k}{\nu_t}. \tag{B.18}$$

We record that the $k$ and $\omega$ for ”small” boundary conditions have a scale of $1 \times 10^{-7}$ and $1 \times 10^{-4}$ respectively, even for the highest flow rate.

# C

# Mesh generation: comparing *snappyHexMesh* and *CFMESH* libraries

Generating a computational mesh for nasal airflow is not always straightforward. In this study, we tested both the *snappyHexMesh* and the *CFMESH* libraries implemented in the *OpenFOAM* software. From our experience, we have the following observations.

1. *CFMesh* will require less effort and better preserves the surface. The *CFMESH* script can be extended to other geometries with medium parameter-tuning effort, once the script for one geometry gives an acceptable result. However, generated boundary layers appear to be less orthogonal than the boundary layers from the *snappyHexMesh*. Also, it may be troublesome to mesh geometries with small gaps.
2. *snappyHexMesh* has the potential to give a good-quality mesh in terms of orthogonality. However, it will require much more effort in tuning parameters, as the layer generation can be poor with incorrect parameter setups.

We will start with the number of variables in these two libraries. One can already get the difficulty of using *snappyHexMesh* by the number of parameters in the settings. In addition, to use *snappyHexMesh*, one needs to define the base mesh as well, through the *blockMesh* utility. From our experience, in a complicated geometry like the nasal airway, around 50 parameters can be involved for the *snappyHexMesh* dictionary to generate a proper mesh. In comparison, *CFMESH* only requires 20 parameters to generate a mesh for the same geometry.

In addition, in terms of the effort for maintenance, *snappyHexMesh* may show poor repeatability if we reuse the script which generates a good-quality mesh for one geometry to another geometry. *snappyHexMesh* often requires parameter-tuning, i.e., modifying the parameters in the previous script, to improve the mesh quality for another geometry. Although both libraries require parameter tuning for a new geometry, *CFMESH* requires fewer efforts in parameter-tuning under the same condition compared to *snappyHexMesh*.

Furthermore, in terms of boundary layer generation, we recorded the results of *snappyHexMesh* and *CFMESH* using the same geometry with the same calculated cell size and compared them in figure C.1 and C.2. However, we note that these meshes are not applied in our simulations.

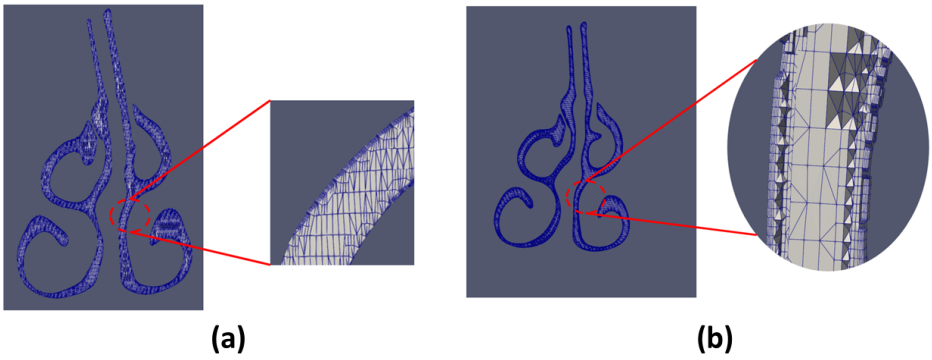


Figure C.1: The performance of *snappyHexMesh* for the layer generation process. In figure C.1 (a), we notice that the resulting mesh will sometimes contain discontinuous boundary layer cells. After many efforts in parameter-tuning, such as changing the base cell size, refinement level, and the desired mesh quality, we were able to obtain a mesh with continuous boundary layer cells, as shown in figure C.1 (b).

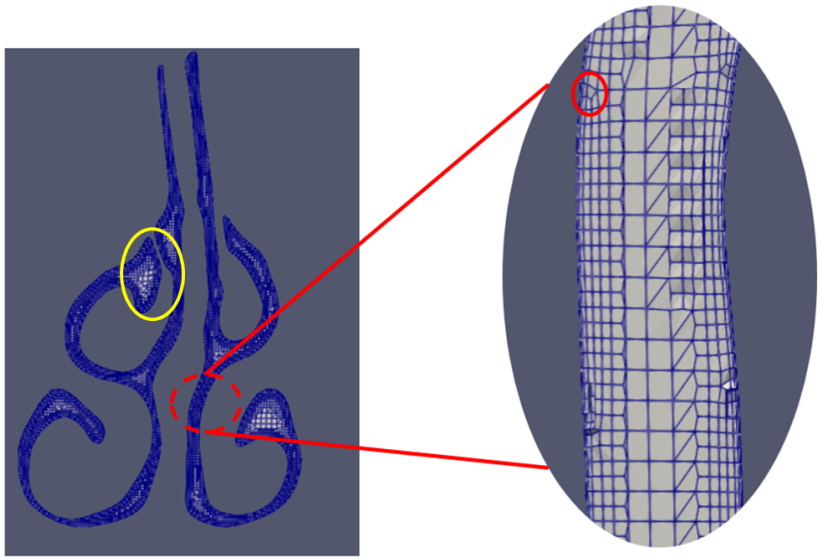

Figure C.2: The performance of *CFMESH* in terms of the layer generation process. The resulting mesh contains a similar number of cells (around 6 million) as the mesh in figure C.1. From our experience, continuous layers of boundary cells can always be generated.

Moreover, we have some additional comments on *CFMESH*. *CFMESH* sometimes could not resolve specific regions of the nasal airway where the geometry is thin, such as the nasal septum or some sections in the middle meatus, where the base-cell size is larger than the size of these thin structures. For the nasal septum, one remedy is to split the STL file for the nasal airway into the left and right sides and mesh these two sides as different regions. However, we had to decrease the base cell size for resolving the middle meatus. However, as a result, this will increase the total number of cells and lead to longer computational time.

Overall, both libraries have their own merits. We decided to use *CFMESH* for this study, because of its low-maintenance and easy-to-use feature. However, we note that our observation could be subject-specific, so some users may prefer *snappyHexMesh* in the nasal airflow study.

# D

# Static or total Pressure?

As discussed in section 4.3, although research has studied the pressure distribution over axial slices, there is no literature introducing which pressure we should examine or how we should examine this pressure. The nasal airflow is extremely 3D, resulting in a non-uniform flow velocity distribution, a non-uniform total pressure, and static pressure distribution at a certain cross-section and in a streamwise direction (seen in section 4.3.1.).

As the issue of static, or total pressure in the nasal airflow can be expanded into independent research work, here we will merely address our understanding from two aspects: firstly, what information will static or total pressure analysis provide, and secondly, what approximation will the analysis require?

## D.1. Theoretical background

Ignoring the elevation loss, the static pressure curve over axial distances resembles an integral form of the “hydraulic grade line” along the approximated streamwise direction. Similarly, the total pressure curve over axial distances can be seen as an integral (area-averaged) form of the “energy grade line”. The concept of the “hydraulic grade line” and “energy grade line” was introduced by White (2011). As a short recap, the hydraulic grade line is calculated from the static pressure head, and the energy grade line is calculated from the total pressure head. **Variation of static pressure** is more straightforward, representing the variation of static pressure over streamwise direction, and may provide information about force if, say, fluid-structure interaction is considered. The nasal airflow can also indicate how much driving force is required for the human lungs to achieve the nasal airflow. Because of cross-section variation, the static pressure curve will also vary as the velocity increases/decreases. In contrast, **variation of the total pressure** describes the flow field from an **energy perspective** and can reflect the energy loss of the flow, including the friction loss and the substantial loss for the recirculation zone. Also, additional losses should be added if the airflow deforms the nasal structure, which is not considered in this study.

As we have stated in section 4.3.1, there is no strict criterion on which pressure should be considered in the nasal airflow. One could argue that comparing total pressure may provide information on the flow state, such as flowing through an orifice where permanent loss exists. In comparison, from this perspective, the static pressure curve represents both permanent loss and the dynamic pressure change caused

by the geometrical variations, as we can already see in figure 4.8. This gives difficulty if we only want to interpret permanent loss from the pressure distribution analysis.

## D.2. Error analysis and an alternative for area-averaged total pressure

A common approach for flow in a smooth pipe or through an orifice plate is to assume an existing streamline at the center line, which is often acceptable because of axis symmetry. However, this approach will not be realistic for the nasal airflow because it is impossible to define a universal streamline for all the geometries. Therefore, in this work, as well as existing literature, for example, Taylor et al. (2010) and Wen et al. (2008), the pressure curve is calculated using area-averaging. Especially for the total pressure distribution where we are interested in the loss between adjacent slices, as we may see below, an additional approximation is added from the area averaging.

Let us consider a steady, incompressible (without heat transfer) flow field passing from cross-section A to cross-section B without elevation. Using energy conservation for this control volume, we will obtain:

$$\iint_A \left(p + \frac{1}{2}\rho \underline{u}^2\right)(\underline{u}\cdot\underline{n})dS = \iint_B \left(p + \frac{1}{2}\rho \underline{u}^2\right)(\underline{u}\cdot\underline{n})dS + \dot{E}_{loss,AB}. \tag{D.1}$$

From equation D.1, we notice that $p + \frac{1}{2}\rho \underline{u}^2$ is total pressure. Also, from mass conservation, we have:

$$\iint_A (\underline{u}\cdot\underline{n})dS = \iint_B (\underline{u}\cdot\underline{n})dS = Q \tag{D.2}$$

Combining equation D.2, we could rewrite equation D.1 as:

$$\frac{\iint_A \left(p + \frac{1}{2}\rho \underline{u}^2\right)(\underline{u}\cdot\underline{n})dS}{\iint_A (\underline{u}\cdot\underline{n})dS} = \frac{\iint_B \left(p + \frac{1}{2}\rho \underline{u}^2\right)(\underline{u}\cdot\underline{n})dS}{\iint_B (\underline{u}\cdot\underline{n})dS} + \frac{\dot{E}_{loss,AB}}{Q}. \tag{D.3}$$

In equation D.3, *the first and second terms are flux-averaged total pressure at cross-sections A and B, respectively*. The third term is then the loss.

If we take one step further and assume that the airflow is uniform, then we have

$$\iint \left(p + \frac{1}{2}\rho \underline{u}^2\right)(\underline{u}\cdot\underline{n})dS = (\underline{u}\cdot\underline{n}) \iint \left(p + \frac{1}{2}\rho \underline{u}^2\right)dS. \tag{D.4}$$

And we can substitute equation D.4 into equation D.3, which will finally be simplified to:

$$\frac{\iint_A \left(p + \frac{1}{2}\rho \underline{u}^2\right)dS}{\iint_A dS} = \frac{\iint_B \left(p + \frac{1}{2}\rho \underline{u}^2\right)dS}{\iint_B dS} + \frac{\dot{E}_{loss,AB}}{Q}. \tag{D.5}$$

Now in equation D.5, *the first and second terms are the area-averaged total pressure at cross-sections A and B, respectively*.

In principle, under the assumption of steady and adiabatic flow, equation D.3 is accurate. Therefore, we could say that *using flux-averaged can give a perfect interpretation for the loss between two adjacent cross-sections*. In comparison, the uniform-flow approximation is required to obtain D.5. Therefore, **one can only use area-averaging**

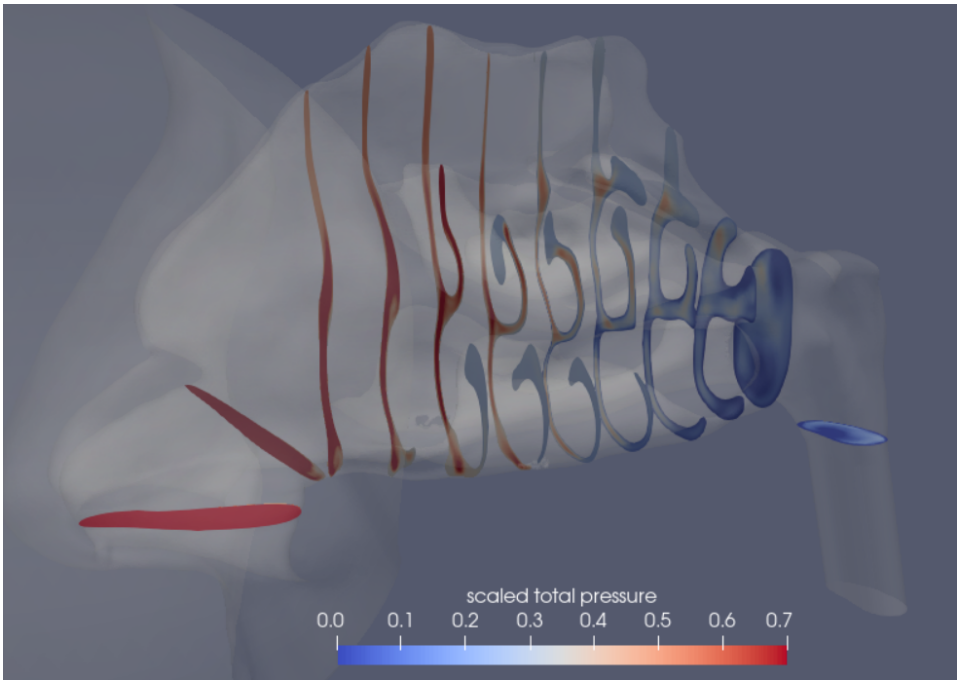


Figure D.1: Axial slices are plotted using the same methodology as in figure 4.6. The total pressure is scaled with the area-averaged total pressure at the pharynx slice for the healthy (FD2) subject. The total pressure within each slice is not entirely uniform, especially for the slices located at the anterior cavum slices.

**to accurately approximate the loss when the flow is uniform throughout cross-sections A and B**.

For the nasal airflow, will this stay true? We visualize the scaled total pressure in figure D.1 and figure D.2. the scaled total pressure is calculated as $1+\frac{P_{tot,i}}{\Delta P_{tot}}$, where $P_{tot,i}$ is total pressure at the slice $i$ and $\Delta P_{tot}$ is the total pressure drop over the entire nasal airway at the selected axial position. Adding $1$ into the scaling prevents the scaled pressure from being negative, which could be counter-intuitive. From figure D.1 and figure D.2, firstly, we notice that the scaled axial slices show a decreasing magnitude along the downstream direction for both subjects. Secondly, comparing the location of the recirculation zones in figure 6.1, we also notice that the total pressure has a lower magnitude at the location where a large recirculation zone exists, visible in the two circled regions of figure D.2.

We will further compare the total pressure resulting from flux-averaging (formulated in equation D.3) and area-averaging (formulated in equation D.5), as shown in figure D.3

We notice from figure D.3 (b) that the area-averaged total pressure will significantly decrease from the location of the internal nasal valve. Revisiting equation D.5, this is presumably caused by the fact that the total pressure is directly averaged with the area, so the total pressure of the recirculation zone is also averaged in the same weight as the total pressure of the mean stream region. In this way, the total pressure difference in adjacent slices becomes both the frictional loss and the total pressure reduction caused by the recirculation zone. Instead, if flux-averaging (in D.3) is used, the low-velocity region in the recirculation zone is added into the averaging with a

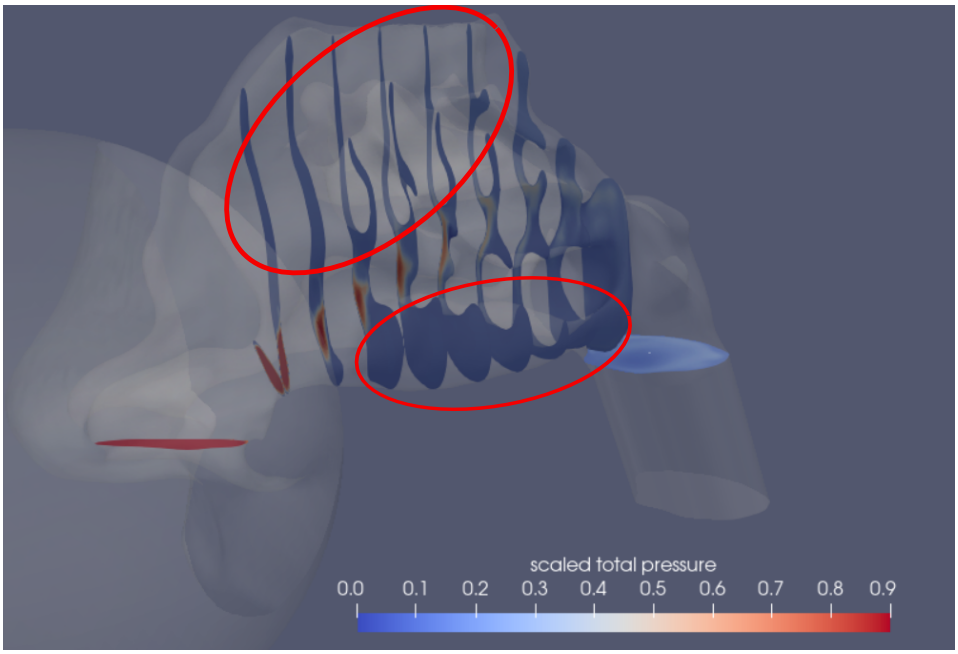


Figure D.2: Axial slices are plotted using the same methodology as in figure 4.6. The two circled-out regions correspond to the recirculation zones observed in figure 6.2 (c). The total pressure is scaled using area-averaging at the pharynx slice for the NAO (scan2) subject. The scan2 total pressure distribution is less uniform than for the FD2 subject. The total pressure distribution is determined mainly by the mean flow distribution, where a compressed inspiratory jet effect caused the flow to restrict in a certain area for the scan2 subject instead of a spreading-out pattern as in the healthy (FD2) subject.

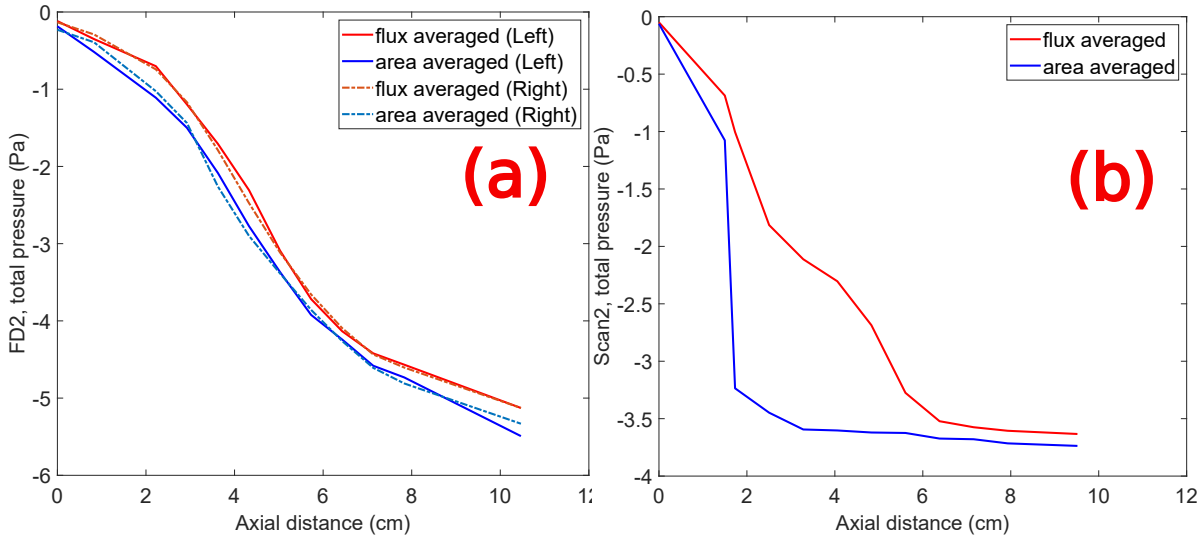


Figure D.3: The total pressure versus axial slice distance for the (a) healthy (FD2, both sides) and (b) NAO (scan2, obstructive side) subject is plotted. In figure D.3 (a), the difference between flux-averaged and area-averaged total pressure for both sides of the healthy (FD2) airway is around 6%. In comparison, such a difference for the obstructive side of the NAO (scan2) subject is more significant and location-dependent. For example, at the third slice where the recirculation is predominant, the area-averaged total pressure is around 2 times smaller than the flux-averaged total pressure. At the pharynx slice, the difference between the flux-averaging and the area-averaging for the NAO subject is around 3%.

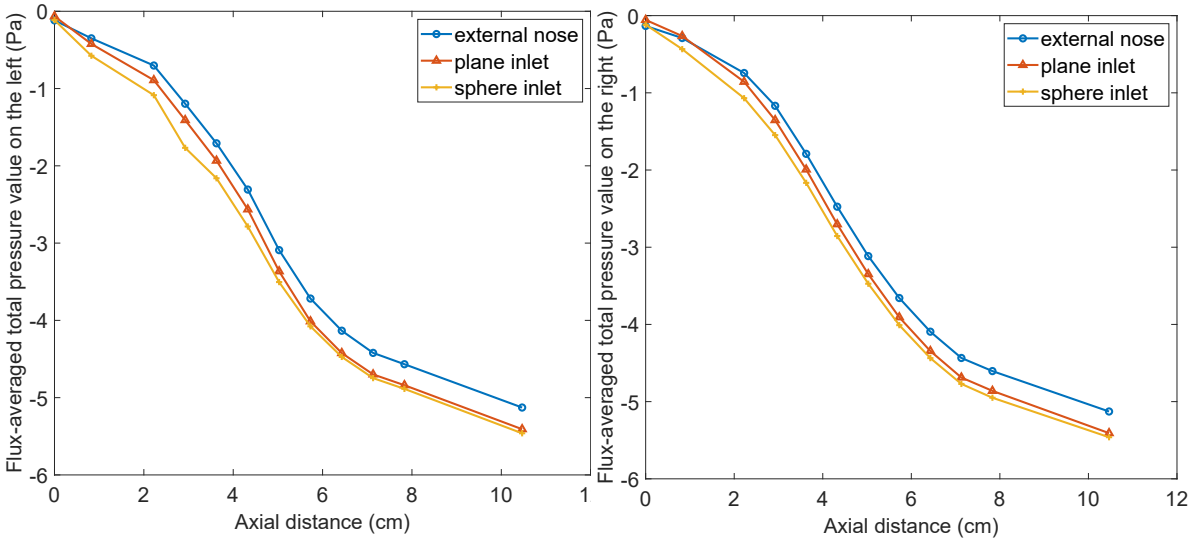


Figure D.4: The flux-averaged total pressure versus the axial distance of each slice is plotted. The flux-averaged total pressure curve of all three boundary configurations shifts upwards with respect to the area-averaged total pressure curve in figure 4.7. Although the flux-averaged total pressure value increased by around 4%, using a different averaging method to calculate total pressure did not alter our conclusions on boundary configuration selection.

smaller weight (the $(\underline{u} \cdot \underline{n})$). In this way, we will obtain a better approximation for the loss between two slices. Compared to the NAO (scan2) subject, in the case where recirculation is less predominant, such as in the healthy (FD2) subject (shown in figure D.3 (a)), the area-averaging can reasonably approximate the total pressure loss because the shape of the curve stays similar. However, the flow is still not uniform across each slice, and errors will still exist if one wishes to approximate loss by looking at the difference in total pressure for adjacent slices.

Overall, from the above analysis, we noticed that using flux-averaging may give the best approximation for the energy loss within the flow field and that area-averaging can give fair approximations for a close-to-uniform flow field. However, during post-processing, we noticed that flux-averaging requires additional steps in the calculation (to calculate the flux and take the average). These additional steps will result in a slightly longer post-processing time when more subjects are involved.

On the last note, we note that using the flux-averaged total pressure will not lead to major changes in our observations from figure 4.7 regarding the boundary configuration selection. The flux-averaged total pressure for the three boundary configurations is plotted in figure D.4.

# Bibliography


Anderson, N., Cassidy, P., Janssen, L., & Dengel, D. (2006). Peak inspiratory flows of adults exercising at light, moderate and heavy workloads. *Journal of the International Society for Respiratory Protection*, *23*, 53–63.

Andre, R., Vuyk, H., Ahmed, A., Graamans, K., & Nolst Trenite, G. (2009). Correlation between subjective and objective evaluation of the nasal airway. a systematic review of the highest level of evidence. *Clinical Otolaryngology*, *34*(6), 518–525.

Bruning, J. J., Goubergrits, L., Heppt, W., Zachow, S., & Hildebrandt, T. (2017). Numerical analysis of nasal breathing: A pilot study. *Facial Plast Surg*, *33*(4), 388–395.

Casey, K. P., Borojeni, A. A., Koenig, L. J., Rhee, J. S., & Garcia, G. J. (2017). Correlation between subjective nasal patency and intranasal airflow distribution. *Otolaryngol Head Neck Surg*, *156*(4), 741–750.

Cherobin, G. B., Voegels, R. L., Gebrim, E., & Garcia, G. J. M. (2018). Sensitivity of nasal airflow variables computed via computational fluid dynamics to the computed tomography segmentation threshold. *PLoS One*, *13*(11), e0207178.

Clark, D. D. W., Signore, D. A. G. D., Raithatha, D. R., & Senior, D. B. A. (2018). Nasal airway obstruction: Prevalence and anatomic contributors. *Ear, Nose & Throat Journal*, *97*(6), 173–176.

Covello, V., Pipolo, C., Saibene, A., Felisati, G., & Quadrio, M. (2018). Numerical simulation of thermal water delivery in the human nasal cavity. *Comput Biol Med*, *100*, 62–73.

Doorly, D. J., Taylor, D. J., Gambaruto, A. M., Schroter, R. C., & Tolley, N. (2008). Nasal architecture: Form and flow. *Philos Trans A Math Phys Eng Sci*, *366*(1879), 3225–46.

Durbin, P., & Reif, B. (2010). *Statistical theory and modeling for turbulent flows*. Wiley.

Elad, D., Liebenthal, R., Wenig, B. L., & Einav, S. (1993). Analysis of air flow patterns in the human nose. *Medical and Biological Engineering and Computing*, *31*(6), 585–592.

Fedorov, A., Beichel, R., Kalpathy-Cramer, J., Finet, J., Fillion-Robin, J. C., Pujol, S., Bauer, C., Jennings, D., Fennessy, F., Sonka, M., Buatti, J., Aylward, S., Miller, J. V., Pieper, S., & Kikinis, R. (2012). 3d slicer as an image computing platform for the quantitative imaging network. *Magn Reson Imaging*, *30*(9), 1323–41.

Franke, R., Rodi, W., & Schonung, B. (1990). Numerical calculation of laminar vortex-shedding flow past cylinders. *Journal of Wind Engineering and Industrial Aerodynamics*, *35*, 237–257.

Frank-Ito, D. O., Wofford, M., Schroeter, J. D., & Kimbell, J. S. (2016). Influence of mesh density on airflow and particle deposition in sinonasal airway modeling. *J Aerosol Med Pulm Drug Deliv*, *29*(1), 46–56.

Garcia, G. J. M., Rhee, J. S., Senior, B. A., & Kimbell, J. S. (2010). Septal deviation and nasal resistance: An investigation using virtual surgery and computational fluid dynamics. *American Journal of Rhinology & Allergy*, *24*(1), e46–e53.

Hadjiliadis, D., & Harron, P. F. (2021). Rapid shallow breathing: Medlineplus medical encyclopedia.

Hahn, I., Scherer, P. W., & Mozell, M. M. (1993). Velocity profiles measured for airflow through a large-scale model of the human nasal cavity. *Journal of Applied Physiology*, *75*(5), 2273–2287.

Hildebrandt, T., Bruning, J. J., Schmidt, N. L., Lamecker, H., Heppt, W., Zachow, S., & Goubergrits, L. (2019). The healthy nasal cavity-characteristics of morphology and related airflow based on a statistical shape model viewed from a surgeon's perspective. *Facial Plast Surg*, *35*(1), 9–13.

Jo, G., Chung, S. K., & Na, Y. (2015). Numerical study of the effect of the nasal cycle on unilateral nasal resistance. *Respir Physiol Neurobiol*, *219*, 58–68.

Jones, N. (2001). The nose and paranasal sinuses physiology and anatomy. *Advanced Drug Delivery Reviews*, *51*(1), 5–19.

Kahana-Zweig, R., Geva-Sagiv, M., Weissbrod, A., Secundo, L., Soroker, N., & Sobel, N. (2016). Measuring and characterizing the human nasal cycle. *PLoS One*, *11*(10), e0162918.

Keyhani, K., Scherer, P. W., & Mozell, M. M. (1995). Numerical Simulation of Airflow in the Human Nasal Cavity. *Journal of Biomechanical Engineering*, *117*(4), 429–441.

Kimbell, J. S., Frank, D. O., Laud, P., Garcia, G. J., & Rhee, J. S. (2013). Changes in nasal airflow and heat transfer correlate with symptom improvement after surgery for nasal obstruction. *J Biomech*, *46*(15), 2634–43.

Kumar, H., Jain, R., Douglas, R. G., & Tawhai, M. H. (2016). Airflow in the human nasal passage and sinuses of chronic rhinosinusitis subjects. *PLoS One*, *11*(6), e0156379.

Lafortuna, C., Minetti, A., & Mognoni, P. (1984). Inspiratory flow pattern in humans. *Journal of applied physiology: respiratory, environmental and exercise physiology*, *57*, 1111–9.

Li, C., Jiang, J., Dong, H., & Zhao, K. (2017). Computational modeling and validation of human nasal airflow under various breathing conditions. *J Biomech*, *64*, 59–68.

Lintermann, A. (2020). Computational Meshing for CFD Simulations. In *Clinical and biomedical engineering in the human nose - a computational fluid dynamics approach* (pp. 85–115). Springer Nature Singapore Pte Ltd. 2021.

McGee, S. (2012). Chapter 18 - respiratory rate and abnormal breathing patterns. In S. McGee (Ed.), *Evidence-based physical diagnosis (third edition)* (Third Edition, pp. 145–155). W.B. Saunders.

Mlynski, G. H. (2013). Physiology and pathophysiology of nasal breathing. In *Nasal physiology and pathophysiology of nasal disorders* (pp. 257–272). Springer Berlin Heidelberg.

Mohapatra, S. S. G., Sahu, N., Rath, S. N., Sahu, M. C., & Padhy, R. N. (2017). Significance of relationship between anatomical variants of middle turbinate and nasal septum in recurrent acute rhinosinusitis patients. *International Journal of Otorhinolaryngology and Head and Neck Surgery*, *3*(3).

Moniripiri, M., Amjadimanesh, H., Faramarzi, M., Sadrizadeh, S., & Abouali, O. (2021). Numerical simulation of unsteady airflow in a nasal cavity for various sizes of maxillary sinus opening in a virtual endoscopic surgery. *Respir Physiol Neurobiol*, *291*, 103690.

Nieuwstadt, F., Boersma, B., & Westerweel, J. (2016). *Turbulence: Introduction to theory and applications of turbulent flows*. Springer.

O'Neill, G., & Tolley, N. S. (2019). The complexities of nasal airflow: Theory and practice. *J Appl Physiol (1985)*, *127*(5), 1215–1223.

Patel, R. G., Garcia, G. J., Frank-Ito, D. O., Kimbell, J. S., & Rhee, J. S. (2015). Simulating the nasal cycle with computational fluid dynamics. *Otolaryngol Head Neck Surg*, *152*(2), 353–60.

Pendolino, A. L., Scarpa, B., & Ottaviano, G. (2019). Relationship between nasal cycle, nasal symptoms and nasal cytology. *Am J Rhinol Allergy*, *33*(6), 644–649.

Quadrio, M., Pipolo, C., Corti, S., Messina, F., Pesci, C., Saibene, A. M., Zampini, S., & Felisati, G. (2016). Effects of ct resolution and radiodensity threshold on the cfd evaluation of nasal airflow. *Med Biol Eng Comput*, *54*(2-3), 411–9.

Doorly, D., Taylor, D. J., Franke, P., & Schroter, R. C. (2008a). Experimental investigation of nasal airflow. *Proc Inst Mech Eng H*, *222*(4), 439–53.

Doorly, D. ., Taylor, D., & Schroter, R. (2008b). Mechanics of airflow in the human nasal airways. *Respir Physiol Neurobiol*, *163*(1), 100–110.

Rennie, C. E., Gouder, K. A., Taylor, D. J., Tolley, N. S., Schroter, R. C., & Doorly, D. J. (2011). Nasal inspiratory flow: At rest and sniffing. *Int Forum Allergy Rhinol*, *1*(2), 128–35.

Rhee, J. S., Poetker, D. M., Smith, T. L., Bustillo, A., Burzynski, M., & Davis, R. E. (2005). Nasal valve surgery improves disease-specific quality of life. *Laryngoscope*, *115*(3), 437–40.

Rhee, J. S., Book, D. T., Burzynski, M., & Smith, T. L. (2003). Quality of life assessment in nasal airway obstruction. *The Laryngoscope*, *113*(7), 1118–1122.

Rhee, J. S., Sullivan, C. D., Frank, D. O., Kimbell, J. S., & Garcia, G. J. M. (2014). A systematic review of patient-reported nasal obstruction scores. *JAMA Facial Plastic Surgery*, *16*(3), 219–225.

Ricci, E., Palonta, F., Preti, G., Vione, N., Nazionale, G., Albera, R., Staffieri, A., Cortesina, G., & Cavalot, A. L. (2001). Role of nasal valve in the surgically corrected nasal respiratory obstruction: Evaluation through rhinomanometry. *American Journal of Rhinology*, *15*(5), 307–310.

Samad, I., Stevens, H., & Maloney, A. (1992). The efficacy of nasal septal surgery. *The Journal of otolaryngology*, *21*(2), 88–91.

Schatz, C. J., & Ginat, D. T. (2014). Imaging features of rhinoplasty. *AJNR Am J Neuroradiol*, *35*(2), 216–22.

Schlichting, H., Krause, E., Oertel, H., & Gersten, K. (2003). *Boundary-layer theory*. Springer Berlin Heidelberg.

Schreck, S., Sullivan, K. J., Ho, C. M., & Chang, H. K. (1993). Correlations between flow resistance and geometry in a model of the human nose. *Journal of Applied Physiology*, *75*(4), 1767–1775.

Siu, J., & Douglas, R. (2021). Sinonasal anatomic variants, diseases and their management. In K. Inthavong, N. Singh, E. Wong, & J. Tu (Eds.), *Clinical and biomedical engineering in the human nose: A computational fluid dynamics approach* (pp. 31–42). Springer Singapore.

Stewart, M., Ferguson, B., & Fromer, L. (2010). Epidemiology and burden of nasal congestion. *Int J Gen Med*, *3*, 37–45.

Sullivan, C. D., Garcia, G. J., Frank-Ito, D. O., Kimbell, J. S., & Rhee, J. S. (2014). Perception of better nasal patency correlates with increased mucosal cooling after surgery for nasal obstruction. *Otolaryngol Head Neck Surg*, *150*(1), 139–47.

Sundh, C., & Sunnergren, O. (2015). Long-term symptom relief after septoplasty. *Eur Arch Otorhinolaryngol*, *272*(10), 2871–5.

Taylor, D. J., Doorly, D. J., & Schroter, R. C. (2010). Inflow boundary profile prescription for numerical simulation of nasal airflow. *J R Soc Interface*, *7*(44), 515–27.

Thulesius, H. (2012). *Rhinomanometry in clinical use. a tool in the septoplasty decision making process.* (Doctoral dissertation). Otorhinolaryngology (Lund). Department of Otorhinolaryngology, Lund University.

Tretiakow, D., Tesch, K., Meyer-Szary, J., Markiet, K., & Skorek, A. (2020). Three-dimensional modeling and automatic analysis of the human nasal cavity and paranasal sinuses using the computational fluid dynamics method. *Eur Arch Otorhinolaryngol*.

Van Strien, J., Shrestha, K., Gabriel, S., Lappas, P., Fletcher, D. F., Singh, N., & Inthavong, K. (2021). Pressure distribution and flow dynamics in a nasal airway using a scale resolving simulation. *Physics of Fluids*, *33*(1), 011907.

Versteeg, H., & Malalasekera, W. (2007). *An introduction to computational fluid dynamics: The finite volume method*. Pearson Education Limited.

Wang, Y., & Elghobashi, S. (2014). On locating the obstruction in the upper airway via numerical simulation. *Respir Physiol Neurobiol*, *193*, 1–10.

Weinhold, I., & Mlynski, G. (2004). Numerical simulation of airflow in the human nose. *Eur Arch Otorhinolaryngol*, *261*(8), 452–5.

Weller, H. G., Tabor, G., Jasak, H., & Fureby, C. (1998). A tensorial approach to computational continuum mechanics using object-oriented techniques. *Computers in Physics*, *12*(6), 620–631.

Wen, J., Inthavong, K., Tu, J., & Wang, S. (2008). Numerical simulations for detailed airflow dynamics in a human nasal cavity. *Respir Physiol Neurobiol*, *161*(2), 125–35.

White, F. (2011). *Fluid mechanics*. McGraw Hill.

Whyte, A., & Boeddinghaus, R. (2020). Imaging of adult nasal obstruction. *Clin Radiol*, *75*(9), 688–704.

Wong, E., Siu, J., Douglas, R., & Singh, N. (2021). Anatomy and physiology of the human nose. In K. Inthavong, N. Singh, E. Wong, & J. Tu (Eds.), *Clinical and biomedical engineering in the human nose: A computational fluid dynamics approach* (pp. 9–29). Springer Singapore.

Xiao, Q., Bates, A. J., Cetto, R., & Doorly, D. J. (2021). The effect of decongestion on nasal airway patency and airflow. *Sci Rep*, *11*(1), 14410.

Xiong, G.-X., Zhan, J.-M., Jiang, H.-Y., Li, J.-F., Rong, L.-W., & Xu, G. (2008). Computational fluid dynamics simulation of airflow in the normal nasal cavity and paranasal sinuses. *American Journal of Rhinology*, *22*(5), 477–482.

Yepes-Nunez, J. J., Bartra, J., Munoz-Cano, R., Sanchez-Lopez, J., Serrano, C., Mullol, J., Alobid, I., Sastre, J., Picado, C., & Valero, A. (2013). Assessment of nasal obstruction: Correlation between subjective and objective techniques. *Allergol Immunopathol (Madr)*, *41*(6), 397–401.

Zamankhan, P., Ahmadi, G., Wang, Z., Hopke, P. K., Cheng, Y.-S., Su, W. C., & Leonard, D. (2006). Airflow and deposition of nano-particles in a human nasal cavity. *Aerosol Science and Technology*, *40*(6), 463–476.

Zhang, Z., & Kleinstreuer, C. (2011). Laminar-to-turbulent fluid–nanoparticle dynamics simulations: Model comparisons and nanoparticle-deposition applications. *International Journal for Numerical Methods in Biomedical Engineering*, *27*(12), 1930–1950.

Zhao, K., Blacker, K., Luo, Y., Bryant, B., & Jiang, J. (2011). Perceiving nasal patency through mucosal cooling rather than air temperature or nasal resistance. *PLoS One*, *6*(10), e24618.

Zhao, K., Jiang, J., Blacker, K., Lyman, B., Dalton, P., Cowart, B. J., & Pribitkin, E. A. (2014). Regional peak mucosal cooling predicts the perception of nasal patency. *Laryngoscope*, *124*(3), 589–95.